

Effects of Ionic and Electronic Charge Carriers in Nanostructured TiO₂ on Lithium Storage

Von der Fakultät Chemie der Universität Stuttgart
zur Erlangung der Würde eines Doktors der
Naturwissenschaften (Dr. rer. nat.)
genehmigte Abhandlung

Vorgelegt von

Ji-Yong Shin

aus Seoul, Südkorea

Hauptberichter: Prof. Dr. Joachim Maier

Mitberichter: Prof. Dr. Joachim Bill

Prüfungsvorsitzender: Prof. Dr. Emil Roduner

Tag der mündlichen Prüfung: 26.03.2012

*With special thanks to my wife, parents, and brother
for their great support and love...*

나의 사랑하는 아내, 부모님, 그리고 동생에게 특별히 감사하며...

Erklärung

Die vorliegende Doktorarbeit wurde vom Autor selbst in der Abteilung von Prof. Maier am Max-Planck-Institut für Festkörperforschung, im Zeitraum von Oktober 2008 bis Januar 2012 angefertigt. Der Inhalt ist die eigene Arbeit des Autors, Ausnahmen sind gekennzeichnet, und wurde noch nicht zur Erlangung einer Qualifizierung oder eines Titels an einer akademischen Institution eingereicht.

Stuttgart, den 27 Februar 2012

Ji-Yong Shin

Declaration

The work described in this thesis was carried out by the author in the Department of Prof. Maier at the Max Planck Institute for Solid State Research from October 2008 to January 2012. The contents are the original work of the author except where indicated otherwise and have not been previously submitted for any other degree or qualification at any academic institution.

Stuttgart, 27 February 2012

Ji-Yong Shin

Acknowledgements

There are many I have to be grateful for. I must say that I could not have done it without their great support and love.

More than anyone, I would like to express my heartfelt words of gratitude to Prof. Dr. Joachim Maier who guided me over the years with patience. It was a great honor to work with him and gain an opportunity to learn some of his deep knowledge of physical and electrochemistry. With his sapient advice, inspiration and encouragement, I was able to enjoy all scientific activities here in Max Planck Institute, Stuttgart.

I would like to especially thank my daily supervisor Dr. Dominik Samuelis who extensively involved in my PhD work for his guidance. I also want to thank Dr. Reinhard Kremer (Chemical Service Group) for his advice and words of encouragement as an external supervisor throughout my PhD work.

I am grateful to Prof. Dr. Joachim Bill and Prof. Dr. Emil Roduner for being on my examination committee and reviewing this thesis.

Many thanks to all my colleagues at the Maier's department; Sofia Weiglein for her great administrative support, Kiran Adepalli and Dr. Jong Hoon Joo for fruitful daily discussion, Nils Ohmer for his assistance for the "Zusammenfassung", Anja Wedig and Dr. Katja Weichert for their kind helps with always smiley faces, and Changbao Zhu, Drs. Lijun Fu, Kun Tang, Chilin Li for their kind help for experimental problems.

Many thanks also to Gabi Götz, Annette Fuchs, Viola Duppel, Udo Klock, Uwe Traub, Peter Senk, Edwald Schmitt for all technical support.

I would like to also thank to Dr. Hans-Georg Libuda (coordinator of International Max Planck Research School for Advanced Materials) for his kind and constant help throughout my PhD periods.

Special thanks to all of my Korean colleagues and friends for their warm affection that encourage me a lot while I stayed in Stuttgart.

Most importantly, I would like to express my deepest gratitude to my family. First is my lovely wife Chorong Kim who always encouraged me to pursue what matters most with constant support and love. I must thank also my parents and brother who never gave up hope for me.

Zusammenfassung

Ein wachsender gesellschaftlicher Bedarf an effizienten Energiespeichern im Bereich der Elektromobilität und der Intelligenten Stromnetze rückt Lithiumbatterien aufgrund ihrer hohen Energie- und Leistungsdichte ins Rampenlicht des Interesses. Aufgrund der limitierenden elektrochemischen Eigenschaften der benutzten Elektrodenmaterialien ist es jedoch noch immer schwierig, die Anforderungen der Verbraucher hinsichtlich Lade- und Entladegeschwindigkeit, sowie Energiedichte zu erfüllen. Da für simplifizierte Bedingungen die Zeit, bis ein Partikel des Elektrodenmaterials geladen ist, dem Quotienten aus dem Quadrat der zurückzulegenden Diffusionsstrecke des Lithiums im Elektrodenmaterial (L) und dem Diffusionskoeffizienten (D) nach $\tau_{\text{eq}} \propto L^2/D$ proportional ist, ist offensichtlich, dass kurze (Ent-)Ladezeiten durch kurze Diffusionslängen und große Diffusionskoeffizienten erreicht werden können. In den vergangenen Jahren wurden daher große Anstrengungen unternommen, diese Parameter verändern und kontrollieren zu können. Da der Ladungstransport in Lithiumbatterien sowohl ionische, als auch elektronische Ladungsträger involviert, ist ein grundlegendes Verständnis der jeweiligen Rolle beider Arten von Ladungsträgern von großer Bedeutung, um eine gute Performance der Batterie zu erreichen. Das Hauptziel dieser Arbeit ist es daher, unter Benutzung von Titandioxid (TiO_2) als Modellsystem, die Effekte bezüglich der Länge der Diffusionsstrecke und Konzentration beider Ladungsträger (Li^+ und e^-) auf den Lithiumtransport und die Lithiumspeicherung zu verstehen. Darüber hinaus soll außerdem eine Strategie aus dem Blickwinkel der Defektchemie vorgeschlagen werden, um Elektrodenmaterialien mit guter Performance herstellen zu können.

Im ersten Teil der Arbeit wird hauptsächlich der Einfluss der zurückzulegenden Diffusionsstrecke ionischer Ladungsträger (d.h. Li^+) im Material auf die Lithiumspeicherung untersucht. Hierzu wurden hierarchisch aufgebaute,

nanoporöse TiO_2 Partikel mit einer großen Oberfläche via Hydrolyse-Methoden hergestellt und elektrochemisch charakterisiert. Durch diese Nano-Strukturierung wurde die Diffusionsstrecke der Li^+ -Ionen in den Partikeln signifikant verkürzt, was zu einer exzellenten Performance im Vergleich zu unporösen Materialien hinsichtlich der Lithiumspeicherung geführt hat, wobei eine erhöhte Speicherfähigkeit sowohl in der Volumenphase, als auch an der Grenzfläche erreicht wurde. Insbesondere die Natur der Grenzflächenspeicherung wird systematisch diskutiert und ihre große Bedeutung für Lithiumbatterien hervorgehoben.

Der zweite Teil dieser Arbeit konzentriert sich auf die Untersuchung des Einflusses der Konzentration elektronischer und ionischer Ladungsträger (d.h. e^- und Li^+) auf die Lithium-Speicherung. Um die Konzentration an elektronischen Ladungsträgern in nano-strukturiertem TiO_2 zu erhöhen, wurden die folgenden zwei Strategien verfolgt: (1) Bildung von nativen, eingefrorenen Defekten (sauerstoffarme $\text{TiO}_{2-\delta}$ nanoporöse Partikel), (2) homogene n-typ-Dotierung durch extrinsische Defekte (Nb^{5+} -substituierte mesoporöse TiO_2 -Nanopartikel). Die Ergebnisse werden auf der Basis verschiedener experimenteller Verfahren diskutiert, sowie durch eine theoretische defekt-chemische Betrachtung analysiert. Insbesondere erlauben sie, die experimentell beobachteten Optima in der Konditionierung zu erklären.

Diese verschiedenen Strategien stellen nicht nur die relevanten Stellgrößen zur Optimierung der Performance zur Verfügung, sondern erlauben auch ein tieferes Verständnis der ionischen und elektronischen Ladungsträger in Lithiumbatterien.

Abstract

As far as efficient energy storage device in electric vehicles or smart grids are concerned lithium batteries came to the fore due to their high energy and power densities. However, it is still challenging to develop reasonably high rate and energy density batteries because of the limitation in intrinsic electrochemical properties of electrode materials. For electrode materials in Li-batteries, excellent performance can be only achieved by short diffusion length (L) and high chemical diffusivity (\tilde{D}) of Li. In recent years, therefore many efforts to control the time dependence have been conducted in the field of Li-batteries. As operation of Li-batteries involves both ionic and electronic charge carriers, fundamental understanding of the role of each charge carrier is of great importance. Using titanium dioxide (TiO_2) as a model material, the main aim of this study therefore is to primarily understand effects of size and morphology and defect chemistry on the overall lithium transport and storage properties and furthermore to propose a strategy to design high performance electrode materials from the standpoint of defect chemistry.

In the first part, effects of size and morphology of titania (variation of transport length of mainly ionic charge carriers (*i.e.* Li^+)) on the Li storage are studied. Hierarchical nanoporous TiO_2 particles with a large interfacial proportion were successfully prepared by hydrolysis and its electrochemical performance investigated. Due to the significantly shortened transport length of Li^+ ion by nanostructuring, the materials showed excellent Li storage performance (showing both enhanced bulk and interfacial Li storage contributions) compared to nonporous materials. Especially, the nature of interfacial storage behavior is systematically discussed and its great importance for Li-batteries emphasized.

The second part of the thesis mainly focuses on effects of charge carriers concentration (variation of electronic charge carrier concentration) on the Li

storage properties. To increase electronic charge carrier concentrations in nanostructured TiO_2 , two different strategies are applied: (1) formation of frozen-in native defects (oxygen-deficient $\text{TiO}_{2-\delta}$ nanoparticles) and (2) homogeneous *n*-type doping by extrinsic defects (Nb^{5+} -substituted mesoporous TiO_2 nanoparticles). The results are discussed on the basis of multiple experimental techniques as well as a theoretical defect chemical analysis.

These different strategies not only allow to develop relevant adjusting screws for optimizing the performance, they also allow a deeper understanding of ionic and electronic charge carriers in the context of Li-batteries.

Contents

Acknowledgements	iv
Zusammenfassung	vi
Abstract	viii
Contents	x
1 General Introduction and Motivation	1
1.1 Fundamental Aspects of Lithium Batteries	4
1.2 Lithium Storage in Titanium (IV) Dioxide	7
1.3 Issues on Electrode Materials and Charge Carriers Effects	10
1.4 Motivation	11
References	13
2 Instrumental Techniques	17
2.1 Structural Characterization	17
2.1.1 X-ray Diffraction	17
2.1.2 Nitrogen Isotherm (Brunauer–Emmett–Teller Surface Area) ·	17
2.1.3 Electron Microscope (HRTEM, FESEM)	18
2.1.4 Karl-Fisher Titration	18
2.1.5 Thermogravimetric Analysis (TGA)	18
2.2 Conductivity Measurement	19
2.2.1 Measurement for Chapter 4	19
2.2.2 Measurement for Chapter 5	19
2.3 Electrochemical Characterization	20
2.3.1 Electrochemical Cell Assembly	20
2.3.2 Electrochemical Impedance Spectroscopy and Cyclic Voltammetry	20
2.3.3 Electrochemical Battery Test	21

3	Effects of Size and Morphology on Li Storage	22
3.1	Introduction	23
3.2	Materials and Preparation	24
3.3	Results and Discussion	24
3.3.1	Structural Characterization	24
3.3.2	Electrochemical Analysis: Li Storage Performance	29
3.3.2.1	Effects of Size and Porosity	29
3.3.2.2	Study on Interfacial Li Storage	33
3.4	Conclusion	37
	References	39
4	Effects of Defect Chemistry on Li Storage I. Case Study of Frozen-in Native Defects	41
4.1	Introduction	42
4.2	Concept: Frozen-in Native Defects	43
4.3	Experimental Results	45
4.3.1	Materials Preparation	45
4.3.2	Results and Discussion	46
4.3.2.1	Structural Characterization	47
4.3.2.2	Thermogravimetric Analysis	51
4.3.2.3	Conductivity Study	53
4.3.2.4	Electrochemical Analysis: Li Storage Performance	54
4.3.2.5	Electrochemical Analysis: Kinetic Analysis	57
4.3.2.6	Discussion: Defect Model	61
4.4	Theoretical Analysis– Brouwer Diagrams	69
4.4.1	Study on Defect Concentration	69
4.4.2	Study on Lithium Diffusivity	77
4.4.2.1	Negligible Initial Trapping Situation	78
4.4.2.2	Strong Initial Trapping Situation	79
4.4.2.3	Weak (Intermediate) Initial Trapping Situation	80
4.5	Conclusion	84
	References	86
5	Effects of Defect Chemistry on Li Storage II. Case Study of Extrinsic Defects	89
5.1	Introduction	90
5.2	Experimental Results	91
5.2.1	Materials Preparation	91
5.2.2	Results and Discussion	92
5.2.2.1	Structural Characterization	92
5.2.2.2	Defect Chemistry and Conductivity Study	97
5.2.2.3	Electrochemical Analysis: Kinetic Analysis	100
5.2.2.4	Electrochemical Analysis: Li Storage Performance	105

5.3 Theoretical Analysis– Brouwer Diagrams	111
5.3.1 Study on Defect Concentration	111
5.3.2 Study on Lithium Diffusivity	116
5.4 Conclusion	119
References	121
6 Conclusions and Outlook	123
References	127
Abbreviations and Symbols	128
Curriculum Vitae	132

1

General Introduction and Motivation

Modern society is characterized by constant needs for energy. In the past century, fossil fuels such as coal and petroleum have been considered as major sources to generate electric energy. However, concerns of environmental pollution *i.e.* global warming which results from the increased emission of carbon dioxide have brought a paradigm shift away from conventional energy sources towards so-called ‘renewable’ ones for example, wind, tidal and solar power. This paradigm shift into the sustainable energy sources has encouraged researchers to extensively investigate new energy production devices *e.g.* solar cells, wind turbines, tidal plants, and hydro-power plants. Along with the energy production from renewable power plants, it is also crucial to attain high energy storage efficiency to convert these seasonal and highly time-dependent sources into a stable and reliable energy supply. Therefore technologies to develop devices which can efficiently store the electric energy are currently another significant issue. It is obvious that the most familiar and efficient electrical energy storage devices so far are batteries. It did not take long for researchers to realize that among various types of batteries lithium-based rechargeable cells are the most promising candidates. This is due to their high energy and power densities (specific energy density; 100 – 180 Wh/kg), compared with other types of rechargeable batteries such as lead acid (specific energy density; 30 – 50 Wh/kg), nickel-cadmium (specific energy density; 45 – 80

Wh/kg) and nickel-metal hydride (specific energy density; 60 – 120 Wh/kg) batteries as illustrated in Figure 1.1 and Table 1.1.

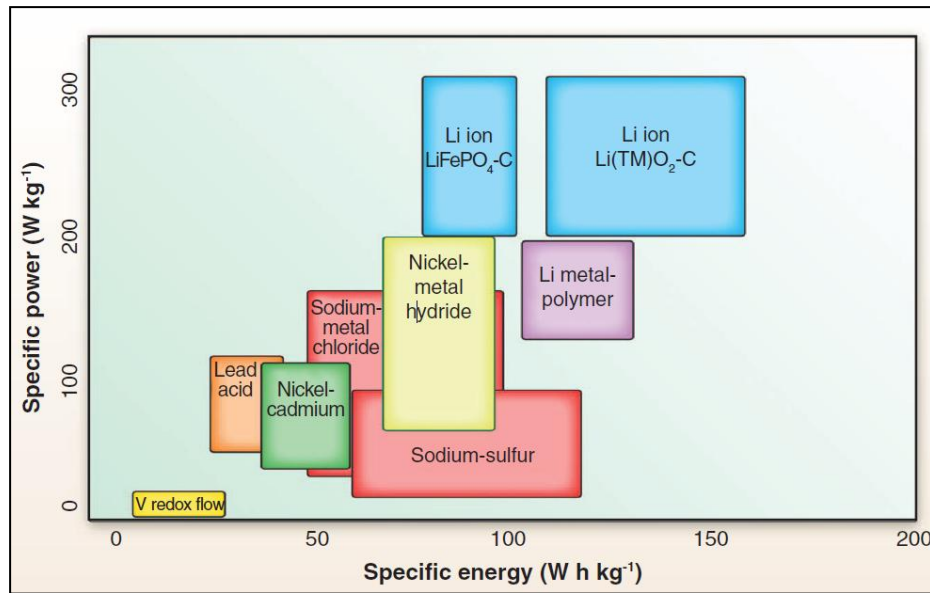


Figure 1.1: Comparison of gravimetric power and energy densities for different rechargeable batteries[1].

Table 1.1: Typical electrochemical properties of secondary batteries[2].

System	Nominal cell voltage [V]	Specific energy [Wh·kg ⁻¹]	Cycle life [up to 80 % initial capacity]	Charge time [h]	Self-discharge per month [%]
Lead-acid	2	30-50	200-350	8-16	5
Ni-Cd	1.25	45-80	1500	1	20
Ni-MH	1.25	60-120	300-500	2-4	30
Li-ion	3.6	110-180	500-1000	2-4	10
Li polymer	3.6	100-130	300-500	2-4	10

During the 1970s the concept of a lithium battery was proposed for the first time by Exxon’s Whittingham (now at Binghamton University). This lithium battery used titanium sulfide (LiTiS_2) as a cathode and lithium as an anode[3]. In 1979, Goodenough demonstrated a rechargeable cell using lithium cobalt oxide (LiCoO_2) as the positive electrode and lithium metal as the negative electrode (with high cell voltage in the 4 V). This innovation enabled lithium batteries feasible[4-5]. Later in 1982, a successful experiment demonstrating the electrochemical intercalation/extraction of lithium in graphite (using metallic lithium, polymer electrolyte, graphite cell) was reported by Armand and Yazami[6-7]. In spite of its

great improvement, the above-mentioned lithium batteries in which the electrode is made from metallic lithium still had safety problems owing to the high reactivity of the metallic lithium with the electrolyte as well as the formation of dendrites. Those dendrites easily penetrated the separator and led to an internal short circuit of the cell. Therefore, Bell Labs introduced a lithium-ion battery in which both the cathode and anode were made of a material containing lithium ions[8]. In 1985, Yoshino reported a prototype cell using carbonaceous material into which lithium ions could be inserted as the anode, and lithium cobalt oxide (LiCoO_2) as the cathode[9]. By using an anode material without metallic lithium, safety problems of cells were drastically improved and finally the first commercial release of lithium-ion batteries was made by Sony in 1991. Sony's lithium batteries used lithium cobalt oxide and graphite as electrodes, and this application of lithium-ion batteries was a revolution in consumer electronics *e.g.* cell phones, laptops *etc.* For last over twenty years, there has been a significant improvement of cell performance of Li-batteries *i.e.* energy density, cyclability, and safety *etc.* to meet the consumers' growth in demand for long-lasting, light-weight portable electronic devices.

With the rapid growth of smart grid and green car *e.g.* hybrid electronic vehicles (HEV) or full Electric Vehicles (EV) market, current issues of Li-battery applications have focused on developing advanced batteries with much higher energy and power densities[10-11]. On the basis of the report from New Energy and Industrial Technology Development Organization (NEDO) in Japan for example, targets for 2020 to develop high-performance batteries for the commercialization of EVs are $250 \text{ Wh}\cdot\text{kg}^{-1}$ and $1500 \text{ W}\cdot\text{kg}^{-1}$ in energy and power density, respectively[12]. However, there have been still critical limitations towards a success in developing such high-performance lithium batteries for EV application (with a reasonable driving distance and charging time). This results mainly from the unsatisfied intrinsic electrochemical properties of current electrode materials. Hence a fundamental understanding of intrinsic properties of electrode materials is of prime importance to overcome the current limitations.

1.1 Fundamental Aspects of Lithium Batteries

Through electrochemical redox reactions, batteries convert chemical energy into electrical energy. If an electrochemical cell is in the equilibrium state in which all local actions *e.g.* transport in the electrode stands still, the voltage of cells is essentially determined by the difference in the chemical potential of lithium (μ_{Li}) between two electrodes (positive and negative) according to

$$(\mu_{Li}(positive) - \mu_{Li}(negative)) = -nEF = \Delta_r G$$

where n refers to the number of the charge transferred during the reaction (per mole), E is the thermodynamic equilibrium voltage *i.e.* electromotive force (emf), and F is Faraday constant ($96485.3 \text{ C} \cdot \text{mol}^{-1}$). This difference in the chemical potential of Li is the Gibbs free energy of the reaction. As the chemical potential of lithium consists of the contribution of the lithium ions and electrons ($\mu_{Li} = \tilde{\mu}_{Li^+} + \tilde{\mu}_e^-$) and the electrochemical potential of Li^+ ($\tilde{\mu}_{Li^+}$) is constant over the whole cell ($(\partial/\partial x)\tilde{\mu}_{Li^+} = 0$), it is the electrochemical potential of the electron ($\tilde{\mu}_e^-$) (flowing through the outer circuit) the difference of which expresses the driving force of the cell (Figure 1.2)[13]. While during discharge of cells an electron is removed from the lithium containing negative electrode (anode) material (oxidation), the Li^+ ion recombines with an electron (reduction) coming from the external circuit on the positive electrode (cathode). During the charge process, the reverse procedure occurs by an externally applied electric field (see Figure 1.2).

Figure 1.3 shows essential mechanistic steps in a typical lithium half cell. Basically three decisive steps– i) ion transport (in electrolyte), ii) ion transfer (at electrolyte/electrode interface) and iii) chemical diffusion of neutral lithium (in electrode)– are necessary to operate a battery[14]. The first reaction *i.e.* Li^+ transport in electrolyte (Figure 1.3a) is a steady-state process that is driven by gradients in the electrochemical potential of the lithium ion ($\tilde{\mu}_{Li^+}$) in non-equilibrium condition. Transport coefficient for this reaction is determined by Li^+

conductivity. The lithium ion then has to traverse the phase boundary at the interface between electrolyte and electrode with a driving force being the difference in $\tilde{\mu}_{Li^+}$ on both sides. Assuming this process as close to equilibrium, the transport coefficient is determined by the exchange rate of the process[14]. The last mechanistic step in lithium batteries is the transport in the solid. If ion and electron transport are significantly different, we refer to a chemical diffusion of ions (Li^+) and electrons (e^-) in the electrode. The driving force of chemical diffusion is the gradient of the chemical potential of neutral Li ($(\partial/\partial x)\mu_{Li} = \partial/\partial x(\tilde{\mu}_{Li^+} + \tilde{\mu}_{e^-})$) in electrode materials and the transport coefficient is the ambipolar conductivity $\sigma^\delta (= (\sigma_{e^-}^{-1} + \sigma_{Li^+}^{-1})^{-1})$ which is governed by both Li^+ and e^- . If the driving force is expressed in terms of lithium concentration gradients ($(\partial/\partial x)c_{Li}$), the chemical diffusion coefficient D_{Li} that consists not only of ambipolar conductivity but also of the chemical capacitance C^δ (*i.e.* $\partial c_{Li}/\partial \mu_{Li}$) becomes the transport coefficient[14].

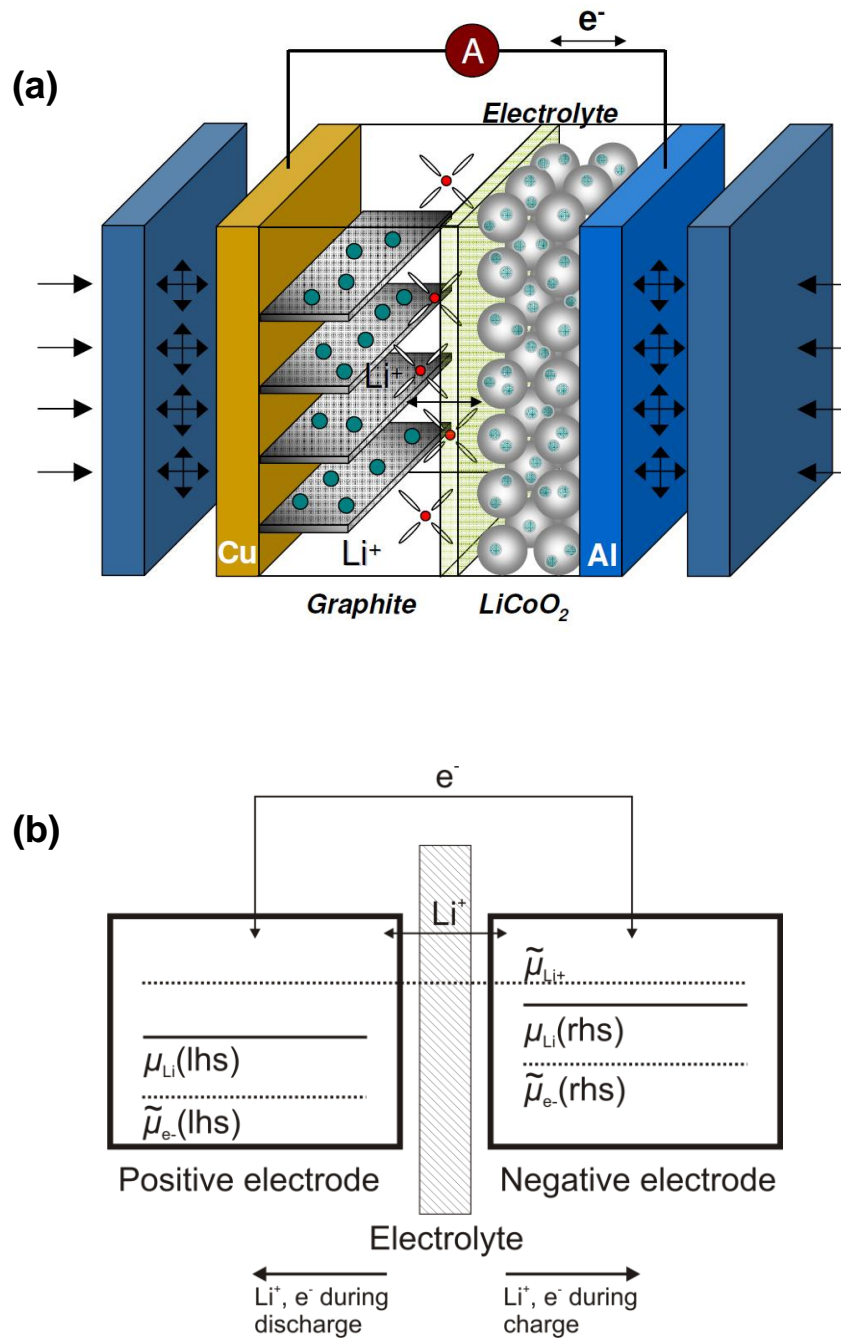


Figure 1.2: (a) Schematic illustration of typical lithium batteries (negative electrode: graphite, positive electrode: LiCoO₂) and (b) thermodynamic view of the operation of lithium batteries (chemical and electrochemical potentials of Li, Li⁺, and e⁻)[13].

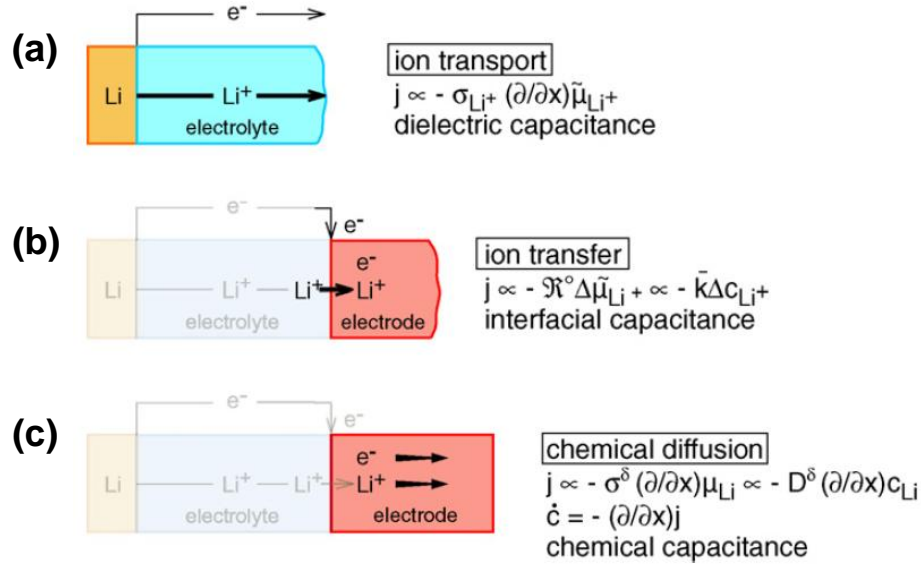


Figure 1.3: The decisive three mechanistic steps in lithium batteries (The Figure is taken from ref. 14, please note that the equations refer to small signal behavior).

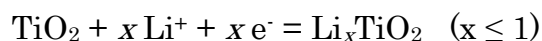
1.2 Lithium Storage in Titanium (IV) Dioxide

Titanium (IV) dioxide TiO_2 exists in three representative naturally-occurring crystalline forms, *viz.* rutile (tetragonal, $P4_2/mnm$), anatase (tetragonal, $I4_1/amd$) and brookite (orthorhombic, $Pbca$). In addition, several synthetic polymorphs are also known, of which primarily TiO_2 (B) has its importance in Li-batteries. Rutile is known as the most common form of TiO_2 in which titanium is octahedrally coordinated by oxygen, whereas in anatase and brookite the titanium-oxygen octahedron is distorted. In the last decades, TiO_2 has been considered as an attractive material for a multitude of applications, for instance heterogeneous photo-assisted catalysts[15-16], electrodes for dye-sensitized solar cells[17-18], and electrochromic displays[19-20] owing to not only its abundance and nontoxicity, but also due to especially suitable band-edge positions for some redox reactions[21-22]. Particularly for the photoelectrode or photocatalyst, modifying the band structure can significantly alter the overall performance of devices. The change in electronic structure can be manipulated by means of either an introduction of new donor levels into the band gap[23], or a formation of native defects such as frozen-in oxygen vacancies[24-25]. In the field of Li-batteries, the focus has been on TiO_2 as a

promising anode material with a number of key advantages. TiO_2 has a comparably low density and molar mass; it offers excellent volumetric and gravimetric storage capacities. Owing to their higher operating voltage compared to graphite, TiO_2 anodes are also more stable and safe during cycling. Also, this material show relatively high theoretical Li-insertion capacity[26-27]. Therefore, various polymorphs of titania such as rutile[28], anatase[29-30], and TiO_2 (B)[31-32] have recently been studied as electrode materials for Li-batteries with excellent electrochemical lithium storage properties.

To investigate Li insertion and transport mechanism in various polymorphs of bulk titania, extensive studies have been done by various research groups. These studies essentially suggest that Li^+ migrates most likely as an interstitial cation, while e^- transports by small polaron hopping along the metal sublattice[33-37]. Upon Li^+ insertion, charge-compensating electrons localize at Ti^{4+} cations in the lattice[38-39]. Moreover, it was found that energy barriers for transport of Li^+ and e^- strongly depend on the crystallographic structure and direction for transport. The values ranging from 0.39 to 0.65 eV for anatase (interoctahedron hopping)[40-43] and from 0.04 to 0.22 eV for rutile (c -direction)[44-48] were determined by computational calculation. On the other hand, experimentally measured energy barriers for Li^+ transport have been reported as higher than those determined by computational methods, showing 0.2 eV[42] and 0.04 eV[49] in anatase and rutile, respectively.

Among several polymorphs of titanium dioxides, the lithium insertion/extraction mechanism in the anatase phase has been most widely investigated due to its more outstanding lithium insertion ability. Figure 1.4a shows a schematic of the lithium battery using anatase TiO_2 as anode[50]. Lithium insertion and extraction in anatase occurs according to the following equation



The theoretical capacity of anatase TiO_2 is reported as 336 mAhg^{-1} ($x = 1$), while for the fully reversible reaction, the maximum x is known to be 0.5, corresponding to a capacity of 168 mAhg^{-1} . As previously mentioned, anatase titania has a tetragonal

structure indexed by the $I4_1/amd$ and thus titanium is surrounded by a distorted oxygen octahedron. During lithiation, an orthorhombic distortion of the lattice occurs (Figure 1.4b) at $x = 0.5$ in Li_xTiO_2 ($\text{Li}_{0.5}\text{TiO}_2$; lithium-titanate, space group $Imma$)[48,50]. As a result, this distortion causes TiO_6 octahedra in Li-titanate in which Li resides in the interstitial voids within the oxygen octahedra, being accompanied by a decrease of the unit cell along the c -axis and an increase along the b -axis[48].

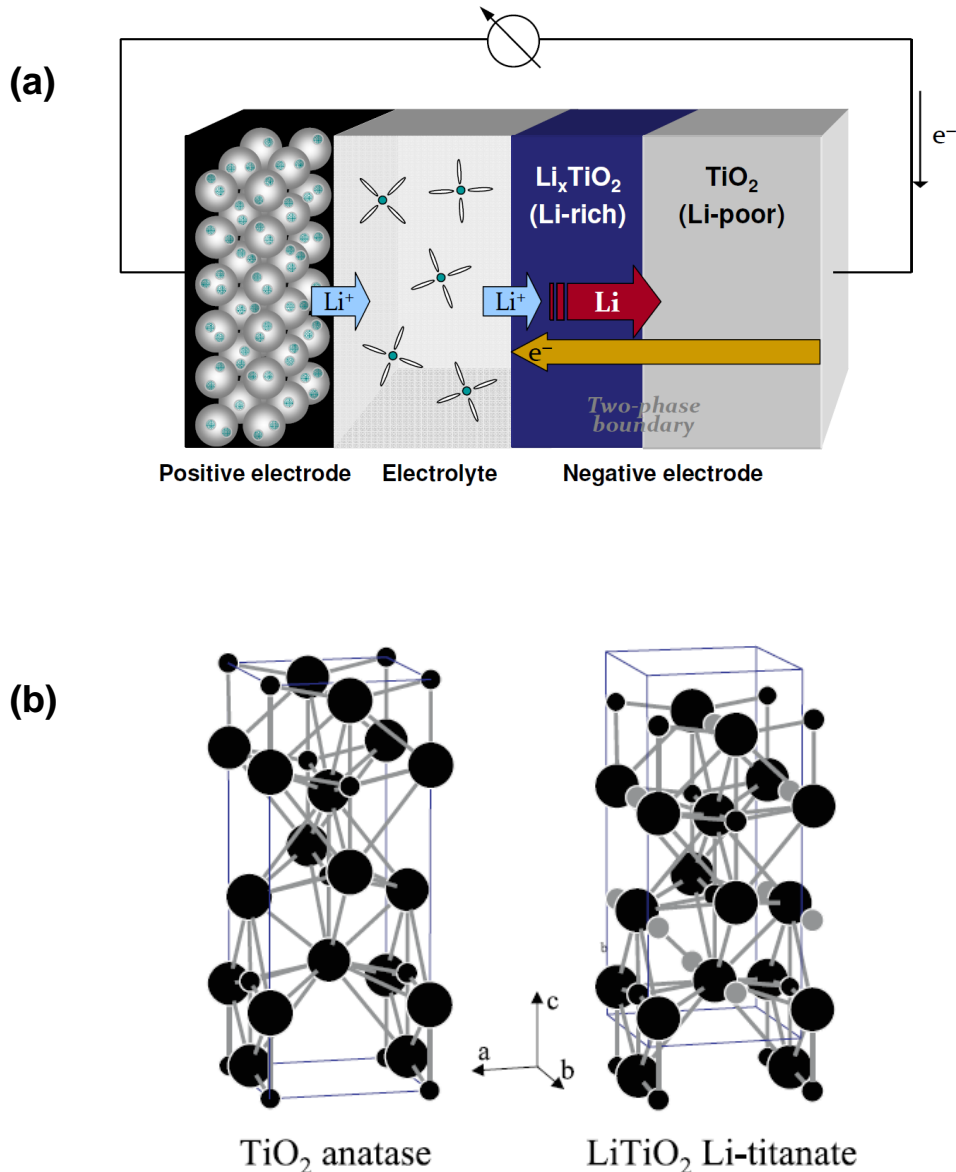


Figure 1.4: (a) Schematic view of a lithium ion-battery using anatase TiO_2 as anode. (b) The unit cell of anatase TiO_2 (space group $I4_1/amd$) and lithiated LiTiO_2 (Ti: small black spheres, O: large black spheres, Li: gray spheres). Figure 1.4b is taken from ref. 50.

1.3 Issues on Electrode Materials and Charge Carriers Effects

Whereas Li^+ transport (in electrolytes) and transfer (at the electrode/electrolyte interfaces) occurs on the nano- and micro-second time scale respectively, the rate-determining time dependence comes into play when considering the chemical diffusion of lithium in the electrode. As far as the storage of Li in electrodes is concerned, it is obvious that high electrode performance *i.e.* utilization of theoretical Li storage capacity, cyclic stability, and rate capability can be achieved by short diffusion length (L) and high chemical diffusivity (\tilde{D}) of Li, as the storage time (*i.e.* diffusion relaxation time) τ_{eq} varies according to $\propto L^2/\tilde{D}$. Hence, extensive studies on size effect (related to L) and/or transport coefficient of lithium (related to \tilde{D}) in terms of lithium storage have been conducted with various electrode materials.

A use of sufficiently small crystals not only reduces L for the mass and charge transport but also increases the surface-to-volume ratio, and therefore the charge rates (current density) of a battery using nano-sized electrode materials can be much higher. More interestingly, nano-sizing leads to new lithium storage phenomena due to a non-trivial interfacial contribution which is related to a re-distribution of charge carrier concentration at interfacial region in the given electrode materials[51-54]. On the other hand, using low dimensional materials *e.g.* one-dimensional nanowires[55] or rods[56] and two-dimensional nanoplatets[57,58] is also advantageous to lithium storage properties due to the significantly reduced diffusion length.

Transport coefficients depend on charge carrier concentration and kinetic parameters (such as mobilities or rate constants). Although there is a recent report that changes in the crystal structure induce a significant change in lithium diffusivity (6 orders of magnitude variation at the tetragonal/orthorhombic boundary with Li^+ migration barriers ranging from 0.5 to 1.4 eV)[59], as the kinetic parameters are still considered to be dominantly determined by the structure, it is the defect concentration whose variation is of prime influence[14]. This applies not only to ionic, but also to electronic charge carriers. Fast electronic transport is

particularly important as it is not only helpful for quick chemical transport but also could make electron collectors in batteries dispensable which would greatly simplify the morphology of cells. As the charge rate capability is predominantly governed by the rate at which lithium travel in the electrode compounds rather than in the electrolyte (as the diffusion coefficients of lithium in solids are much smaller than those in liquids), the improved transport coefficients in the electrode materials are significantly beneficial to excellent lithium storage performance.

1.4 Motivation

The present study is attempting to design a high performance anode material (especially for high rate capability lithium batteries), furthermore to advance fundamental understanding of how ionic and electronic charge carriers in the electroactive materials influence the overall lithium transport and storage properties. As the rate-determining step for electrode reaction is usually solid state diffusion of lithium, the time-constant of which $\tau_{\text{eq}} \propto L^2 / \tilde{D}$, where L is transport length and \tilde{D} is the chemical diffusion coefficient of Li. According to this relation, one can essentially mitigate the diffusion problems either by reducing transport length (increasing morphological complexity using geometric parameters) or by increasing chemical lithium diffusivity (increasing chemical complexity using materials parameters). In addition, the conductivities are important on their own, *viz.* whenever the particles are part of the ionic and electronic connections. For a deeper understanding of the effects of specific charge carriers on the mass transport and storage in the context of Li-batteries, the defect chemistry is analyzed. Main contents in the thesis include (1) the effect of transport length of ionic charge carriers by means of nano-structuring, and (2) the effect of charge carriers concentration by means of homogeneous doping, using the TiO_2 electrode as a model system. Both strategies are applied in the context of a careful consideration of charge carrier chemistry (defect chemistry) to apply fundamental aspects of materials properties to practical applications of electrochemistry in

terms of lithium transport and storage. Part of chapters written in this thesis is based on the published papers. The Chapter 3 is closely following ref. 60 and Chapter 4 is following ref. 61, 62. By combining theoretical analysis and multi-technique experimental methods, this study could ultimately propose the proper way to electrode materials strategies in the field of lithium batteries where ambipolar $\text{Li} = \text{Li}^+ + \text{e}^-$ transport is of significance.

References

- [1] B. Dunn, H. Kamath, J.-M. Tarascon, *Science* **2011**, *334*, 928.
- [2] High Energy Density Lithium Batteries, Ed. K.E. Aifantis, S.A. Hackney, R.V. Kumar, JohnWiley & Sons, Weinheim, **2010**.
- [3] M.S. Whittingham, *Science* **1976**, *192*, 1126.
- [4] J.B. Goodenough *et al.*, EP17400B1, application date (priority) April 5, 1979.
- [5] K. Mizushima, J.B. Goodenough *et al.*, *Mater. Res. Bull.* **1980**, *15*, 783.
- [6] M. Armand, Fast Ion Transport in Solids, ed. W. Van Gool, New York, North-Holland Amsterdam, **1973**, 665.
- [7] R. Yazami, Ph. Touzain, *J. Power Sources* **1983**, *9*, 365.
- [8] S. Basu, US 4304825, "Rechargeable battery", issued 8 December 1981, assigned to Bell Telephone Laboratories.
- [9] A. Yoshino, US 4668595, "Secondary Battery", issued 10 May **1985**, assigned to Asahi Kasei.
- [10] P.G. Bruce, B. Scrosati, J.-M. Tarascon, *Angew. Chem., Int. Ed.* **2008**, *47*, 2930.
- [11] M. Armand, J.-M. Tarascon, *Nature*, **2008**, *451*, 652.
- [12] S. Wakabayashi, Recent activities and topics on battery technology in Japan, Joint EC / European Green Cars Initiative Workshop 2011 "Europe's Strengths, Competencies and Job Opportunities in Electric Vehicle Battery Manufacturing", Bruxelles, December **2011**.
- [13] D. Samuelis, J. Maier, Batteries: Concepts and Systems, Science & Technology, book chapter in Chemical Energy Storage, Ed. R. Schlögl, De Gruyter, Berlin, submitted.
- [14] J. Maier, *J. Power Sources* **2007**, *174*, 569.
- [15] E. Kikuchi, H. Sakamoto, *J. Electrochem. Soc.* **2000**, *147*, 4859.
- [16] K. Ui, T. Fujita, N. Koura, F. Yamaguchi, *J. Electrochem. Soc.* **2006**, *153*, C449.
- [17] B. Oregan, M. Grätzel, *Nature* **1991**, *353*, 737.
- [18] U. Bach, D. Lupo, P. Comte, J. E. Moser, F. Weissörtel, J. Salbeck, H. Spreitzer, M. Grätzel, *Nature* **1998**, *395*, 583.

- [19] W. Weng, T. Higuchi, M. Suzuki, T. Fukuoka, T. Shimomura, M. Ono, L. Radhakrishnan, H. Wang, N. Suzuki, H. Oveisi, Y. Yamauchi, *Angw. Chem. Int. Ed.* **2010**, *49*, 3956.
- [20] C. Bechinger, S. Ferrere, A. Zaban, J. Sprague, B.A. Gregg, *Nature* **1996**, *383*, 608.
- [21] H. Tang, H. Berger, P. E. Schmid, F. Lévy, G. Burri, *Solid State Commun.* **1993**, *87*, 847.
- [22] Y.-C. Nah, I. Paramasivam, P. Schmuki, *Chem. Phys. Chem.* **2010**, *11*, 2698.
- [23] W. Li, Y. Wang, H. Lin, S. Ismat Shah, C.P. Huang, D.J. Doren, S.A. Rykov, J.G. Chen, M.A. Barteau, *Appl. Phys. Lett.* **2003**, *83*, 4143.
- [24] B.J. Morgan, G.W. Watson, *J. Phys. Chem C*, **2010**, *114*, 2321.
- [25] W. Göpel, G. Rocker, R. Feierabend, *Phys. Rev. B* **1983**, *28*, 3427.
- [26] L. Kavan, M. Kalbá, M. Zúkalová, I. Exnar, V. Lorenzen, R. Nesper, M. Grätzel, *Chem. Mater.* **2004**, *17*, 1248.
- [27] Y. Zhou, L. Cao, F. Zhang, B. He, H. Liz, *J. Electrochem. Soc.* **2003**, *150*, A1246.
- [28] Y.-S. Hu, L. Kienle, Y.-G. Guo, J. Maier, *Adv. Mater.* **2006**, *18*, 1421.
- [29] Y.-G. Guo, Y.-S. Hu, W. Sigle, J. Maier, *Adv. Mater.* **2007**, *19*, 2087.
- [30] J.S. Chen, Y.L. Tan, C.M. Li, Y.L. Cheah, D. Luan, S. Madhavi, F.Y.C. Boey, L.A. Archer, X.W. Lou, *J. Am. Chem. Soc.* **2010**, *132*, 6124.
- [31] A.R. Armstrong, G. Armstrong, J. Canales, R. Carcía, P.G. Bruce, *Adv. Mater.* **2005**, *17*, 862.
- [32] G. Armstrong, A.R. Armstrong, P.G. Bruce, P. Reale, B. Scrosati, *Adv. Mater.* **2006**, *18*, 2597.
- [33] J. Nowotny, M. Radecka, M. Rekas, *J. Phys. Chem. Solids* **1997**, *58*, 927.
- [34] E. Yagi, R.R. Hasiguti, M. Aono, *Phys. Rev. B* **1996**, *54*, 7945.
- [35] M.V. Koudriachova, S.W. de Leeuw, N.M. Harrison, *Phys. Rev. B* **2004**, *69*, 054106.
- [36] N.A. Deskins, M. Dupuis, *Phys. Rev. B* **2007**, *75*, 195212.
- [37] S. Kerisit, N.A. Deskins, K.M. Rosso, M. Dupuis, *J. Phys. Chem. C* **2008**, *112*, 7678.

- [38] S. Sodergren, H. Siegbahn, H. Rensmo, H. Lindstrom, A. Hagfeldt, S.E. Lindquist, *J. Phys. Chem. B* **1997**, *101*, 3087.
- [39] A. Henningsson, H. Rensmo, A. Sandell, H. Siegbahn, S. Sodergren, H. Lindstrom, A. Hagfeldt, *J. Chem. Phys.* **2003**, *118*, 5607.
- [40] S. Lunell, A. Stashans, L. Ojamae, H. Lindstrom, A. Hagfeldt, *J. Am. Chem. Soc.* **1997**, *119*, 7374.
- [41] S. Kerisit, K.M. Rosso, Z.G. Yang, J. Liu, *J. Phys. Chem. C* **2009**, *113*, 20998.
- [42] M. Wagemaker, R. van de Krol, A.P.M. Kentgens, A.A. van Well, F.M. Mulder, *J. Am. Chem. Soc.* **2001**, *123*, 11454.
- [43] F. Tielens, M. Calatayud, A. Beltran, C. Minot, J. Andres, *J. Electroanal. Chem.* **2005**, *581*, 216.
- [44] P.I. Kingsbury, W.D. Ohlsen, O.W. Johnson, *Phys. Rev.* **1968**, *175*, 1099.
- [45] O.B. Ajayi, L.E. Nagel, I.D. Raistrick, R.A. Huggins, *J. Phys. Chem. Solids* **1976**, *37*, 167.
- [46] M.V. Koudriachova, N.M. Harrison, S.W. de Leeuw, *Phys. Rev. Lett.* **2001**, *86*, 1275.
- [47] M.V. Koudriachova, N.M. Harrison, S.W. de Leeuw, *Solid State Ionics* **2003**, *157*, 35.
- [48] F. Gligor, S.W. de Leeuw, *Solid State Ionics* **2006**, *177*, 2741.
- [49] O.W. Johnson, *Phys. Rev.* **1964**, *136*, A284.
- [50] M. Wagemaker, Ph.D. thesis: Structure and Dynamics of Lithium in Anatase TiO₂: Study of Interstitial Li-ion Intercalation in Anatase TiO₂ at the Atomic Level, **2003**, Delft University of Technology.
- [51] J. Jamnik, J. Maier, *Phys. Chem. Chem. Phys.* **2003**, *5*, 5215.
- [52] Y.F. Zhukovskii, P. Balaya, E.A. Kotomin, J. Maier, *Phys. Rev. Lett.* **2006**, *96*, 4.
- [53] E. Bekaert, P. Balaya, S. Murugavel, J. Maier, M. Menetrier, *Chem. Mater.* **2009**, *21*, 856.
- [54] P. Balaya, H. Li, L. Kienle, J. Maier, *Adv. Funct. Mater.* **2003**, *13*, 621.
- [55] C. Zhou, Y. Yu, L. Gu, K. Weichert, J. Maier, *Angew. Chem. Int. Ed.* **2011**, *50*, 6278.

- [56] D.K. Kim, P. Muralidharan, H.-W. Lee, R. Ruffo, Y. Yang, C.K. Chan, H. Peng, R.A. Huggins, Y. Cui, *Nano Lett.* **2008**, *8*, 3948.
- [57] B. Ellis, W.H. Kan, W.R.M. Makahnouk, L.F. Nazar, *J. Mater. Chem.* **2007**, *17*, 3248.
- [58] S.F. Yang, P.Y. Zavalij, M.S. Whittingham, *Electrochem. Commun.* **2001**, *3*, 505.
- [59] A. Van der Ven, Elucidating the kinetics of complex Li insertion reactions in Li batteries, abstract #EMA-S4-010-2012, Meeting: Electronic Materials and Applications, Orlando, January 2012.
- [60] J.-Y. Shin, D. Samuelis, J. Maier, *Adv. Funct. Mater.* **2011**, *21*, 3464.
- [61] J.-Y. Shin, J.H. Joo, D. Samuelis, J. Maier, *Chem. Mater.* **2012**, *24*, 543.
- [62] J.-Y. Shin, D. Samuelis, J. Maier, *Solid State Ionics*, in press, DOI: 10.1016/j.ssi.2011.12.003.

2

Instrumental Techniques

2.1 Structural Characterization

2.1.1 X-ray Diffraction

The crystal structure analyses were carried out by X-ray diffraction (XRD) measurements with a PHILIPS PW3710 using filtered CuK α radiation (40kV/30mA). The patterns were identified by the program "X`Pert HighScore" containing databases JCPDS ICDD (Joint Committee on Powder Diffraction Standards - International Center for Diffraction Data). The crystallite size was calculated by fitting the entire powder pattern with the WPPD (whole powder pattern decomposition) method (Bruker TOPAS), enabling the separation of grain size and stress/strain effects.

2.1.2 Nitrogen Isotherm (Brunauer – Emmett – Teller Surface Area)

The nitrogen adsorption and desorption isotherms were performed with an Autosorb-1 system (Quanta-99 Chrome) at 77.4 K to determine the Brunauer–Emmett–Teller (BET) surface area. For a calculation of specific surface area, the following equation was used

$$\frac{1}{W\{(P_0/P)-1\}} = \frac{1}{W_m C'} + \frac{C'-1}{W_m C'} (P/P_0)$$

where W : the weight of gas adsorbed at a relative pressure P_0 , W_m : the weight of adsorbate (constituting a monolayer of surface coverage) and C : the energy of adsorption in the first adsorbed layers. On the other hand, the pore size distribution was determined by Barrett-Joyner-Halenda (BJH) methods, from the adsorption branch of the isotherm.

2.1.3 Electron Microscope (HRTEM, FESEM)

To investigate the morphologies of samples, instrument of scanning electron microscopes (SEM, StereoScan 420 SEM, Leica, Germany, operating at 15 keV, for Chapter 4) and field-emission SEM (FESEM, JEOL 6300F FESEM, JEOL, Japan, operating at 15 keV, for Chapters 3 and 5) were used for this thesis. High resolution transmission electron microscopy (HRTEM), and selected area electron diffraction (SAED) were performed with a Philips CM30 ST (300 kV, LaB6 cathode, $C_s=1.15$ mm).

2.1.4 Karl-Fisher Titration

In Chapter 3, trace amounts of water in nanoporous TiO_2 samples was determined by Karl-Fisher titration technique using a 831 KF Coulometer (Metrohm, Switzerland).

2.1.5 Thermogravimetric Analysis (TGA)

Thermogravimetric analysis, carried out with a NETZSCH TG 209, was used to determine oxygen nonstoichiometry and transport kinetics (chemical diffusion coefficient) in Chapter 4. In all TGA analysis, the different P_{O_2} was controlled by using either pure Ar or 5% H_2 / 95%Ar gas mixture. The "buoyancy" effect which can be induced during the gas switching process was corrected by subtracting the mass change measured with sapphire (having similar volume with that for measured TiO_2 powders) under the same experimental conditions from the mass change measured with the sample.

2.2 Conductivity Measurement

2.2.1 Measurement for Chapter 4

For conductivity measurements in Chapter 4, anatase powders were pressed by cold isostatic pressing (CIP) with ≈ 22 MPa for 5 min to make pellets (5 mm in thickness and 8 mm in diameter). The relative density of the pellet ($\approx 45\%$) was determined by the Archimedes method. Sufficiently thick films of Pt (≈ 200 nm) as electrodes were sputtered on both sides of the pellets. A sintering process was avoided to keep the anatase structure and to avoid grain growth. The electronic conductivities of TiO_2 were measured by the two-probe direct current (DC) method at temperatures between 473 and 723 K with heating and cooling rates of 3 $\text{K}\cdot\text{min}^{-1}$ in pure Ar atmosphere ($P_{\text{O}_2} \approx 10^{-5}$ bar). The experimental procedure for determining the change in electronic conductivity upon H_2 treatment is as follows: the sample is heated in pure Ar, to the treatment temperature of 723 K. During heating, conductivity is recorded as a function of T to analyze the activation enthalpy for the conduction (see Figure 4.6a, region i). After reaching treatment temperature, the gas atmosphere is switched to 5% H_2 / 95% Ar. The conductivity change upon treatment is recorded. (This is the data shown in Figure 4.6a region ii.) At the end, the gas atmosphere is changed to pure Ar, and the sample is cooled down to room temperature, again with recording conductivity as $\mathcal{K}(T)$ (see Figure 4.6a, region iii). The conductivity relaxation (see Figure 4.6b) was also measured in isothermal condition under 5% H_2 /95% Ar ($P_{\text{O}_2} \approx 10^{-25}$ bar) at 723 K. The measurement was performed using a current source and voltmeter (Keithley 2400 SourceMeter, U.S.A.).

2.2.2 Measurement for Chapter 5

For the study shown in Chapter 5, the conductivities were measured also with pellets pressed by the CIP technique with about 22 MPa of isostatic pressure holding for 5 min. Both sides of the pellets were deposited by Pt (≈ 200 nm thickness) under vacuum to improve the electric contact with external electrodes (Pt plates, round-shaped). The geometric shape of the pellets was 7 mm in diameter

and 1.25 mm in thickness. The relative density of all pellets ($\approx 45\%$) was determined also by the Archimedes method. The DC conductivity for undoped, and Nb-doped mesoporous TiO_2 powder was measured at a temperature of 523 K by two-probe method with a current source and voltmeter (Keithley 2400 SourceMeter[®], U.S.A.). The measurement was performed in Ar atmosphere (purity 99.999 %).

2.3 Electrochemical Characterization

2.3.1 Electrochemical Cell Assembly

The two-electrode Swagelok[®]-type lithium half cells were assembled in an Ar-filled glovebox to test electrochemical properties of the samples. To prepare working electrodes, a homogeneous mixture of active material, carbon black (conductive additive), and solution of poly (vinyl difluoride) (PVDF) in N-methyl-2-pyrrolidone (NMP) (binder), at a ratio of 80:10:10 in weight was used. The mixture was uniformly pasted on Cu-foil (0.025 mm in thickness, 99.9%, Goodfellow) followed by overnight drying at 353 K under vacuum. Electrode discs (diameter ≈ 10 mm) were punched from the Cu-foil. The typical electrode loadings were approximately 1 mg cm^{-2} of TiO_2 . Pure lithium metal (Aldrich) as counter electrode, glass fiber textile (GF/D, Whatman) as separator and the prepared working electrode were mounted in sequence. A liquid electrolyte of 1 M LiPF_6 in ethylene carbonate (EC)/dimethyl carbonate (DMC) (1:1, by volume) (Ube Industries Ltd.) was dropped to sufficiently wet the separator.

2.3.2 Electrochemical Impedance Spectroscopy and Cyclic Voltammetry

Electrochemical impedance spectroscopy (EIS) was performed in the frequency range between 100 kHz and 10 mHz with 10 mV AC amplitude. Slow-scan cyclic voltammetry (SSCV) was measured between cutoff voltages of 3.0 and 1.0 V. Scan rates for SSCV measurements were varied from 0.1 to 2 mV s^{-1} to determine the effective chemical diffusion coefficient of lithium. SSCV and EIS measurements were performed using PGZ 402 VoltaLab controlled by software VoltaMaster 4. All

cells were cycled before EIS and SSCV measurements to avoid interference from irreversible capacities at initial cycles.

2.3.3 Electrochemical Battery Test

Electrochemical lithium insertion/extraction reactions were performed by an Arbin MSTAT system at different discharge/charge rates. A rate of nC denotes an insertion/extraction of 1 Li in $1/nh$.

3

Effects of Size and Morphology on Lithium Storage

This section deals with morphological effects on overall Li storage properties. The concept of ‘nano-structuring’ has been applied by means of using a hierarchical nanoporous TiO₂ structure which was prepared by an *in-situ* hydrolysis method. Introducing hierarchically-interconnected pores in the given materials could efficiently reduce the transport length of Li and provide large interfacial area. It was found that these two advantages significantly enhance the Li-storage ability of titania materials. Especially the latter one gives a particularly big impact on charge rates of the cells due to kinetically favored Li storage at the interfacial region. An overall view on the Li-insertion mechanisms in the prepared hierarchical nanoporous titania is proposed and an importance of interfacial storage is emphasized.

3.1 Introduction

The size of electroactive materials for Li-batteries is known to affect the thermodynamics of lithium insertion and can therefore significantly alter overall Li-insertion properties. Various studies on size effects have been performed so far[1-5]. A special focus has been on nano-sized materials as they provide not only larger electrode/electrolyte contact areas thereby allowing not only high accessibility of Li^+ , but also a shortened diffusion path (L) for both electronic and ionic charge carriers[6-9]. In addition to small-size, introducing (hierarchical) porosity into the given materials is beneficial to Li storage performance[10-13] because nano-sized tiny pores also dramatically shorten the lithium diffusion length in the solid phase, as long as the electrolyte can penetrate the pores. This enables fast mass transport towards the interior of the solid. As the solid state diffusion of Li is the rate-determining reaction in electrode materials, the shortened diffusion length induced by using a small size and porous structure is key to improve time-constants. This concept of nano-sizing has largely been studied also with TiO_2 -containing batteries owing to its significantly improved power and energy densities[3-5,14]. Another interesting feature caused by down-sizing is the observation of a new Li storage mechanism. In nano-structured materials so-called interfacial (surface) Li storage is no longer negligible compared to the conventional bulk intercalation of Li into the TiO_2 lattice. Beyond the bulk storage limit, additional Li can be accommodated at interfaces in particular for the composite electrode system. Jamnik and Maier proposed the so-called ‘Job-sharing’ mechanism in which a synergistic storage mode of a Li^+ -accepting and an electron-accepting phase can provide additional storage capacity for Li by charge separation[14]. Using RuO_2 as a model, an additional reversible lithium storage capacity was observed in which Li^+ is accommodated at interstitial sites in Li_2O whereas e^- can occupy the metal surface of Ru, after RuO_2 has been decomposed[9,15].

The motivation of this section is therefore to investigate effects of increased morphological complexity (size and morphology effect) on Li storage ability using a titania electrode. The prepared nanoporous anatase TiO_2 ($np\text{-TiO}_2$) by a modified *in*

situ hydrolysis route[16] is used for this study. By systematically analyzing galvanostatic charge/discharge curves, it was found that the increase of morphological complexity gives rise to not only a significantly enhanced bulk Li storage, but also a drastically enhanced additional storage of Li at the interfacial region[17].

3.2 Materials and Preparation

Preparation of titanium glycolate precursor: First, titanium glycolate was prepared as a precursor. 2 mL of tetrabutyl orthotitanate ($C_{16}H_{36}O_4Ti$, $\geq 97.0\%$, Fluka) were added to 50 mL ethylene glycol followed by vigorous stirring for 8 hours in ambient temperature. In order to ensure homogeneity, the solution was mixed with a solution containing 170 mL acetone and 2.7 mL of distilled water and vigorously stirred for an hour. The suspension was centrifuged (8720 g for 20 min) to harvest white, precipitated powder and this was washed with distilled water and ethanol. After having been dried overnight at 323 K under vacuum, the final product (titanium glycolate precursor) yields 580 mg.

Preparation of nanoporous-TiO₂: The above prepared titanium glycolate precursor (0.2 g) was added into 40 mL of double distilled water for hydrolysis. At 373 K, the mixture was refluxed for an hour. The precipitated white powder was rinsed with distilled water for several times, and centrifuged at 8720 g and dried at 323 K under vacuum. The amount of the final fine *np*-TiO₂ powder was 152 mg. A calcination was carried out at 673 K under air for 5 hours.

3.3 Results and Discussion

3.3.1 Structural Characterization

The structural analysis of the synthesized titanium glycolate precursor (TGP), of as-prepared *np*-TiO₂, and of calcined *np*-TiO₂ were carried out by XRD, nitrogen isotherm, HRTEM, and FESEM. The physicochemical properties of the materials

are summarized in Table 3.1. The as-prepared and calcined np -TiO₂ showed a very high specific surface area as high as 524.5 m²g⁻¹ and 221.9 m²g⁻¹, respectively, with average pore diameters of 4 – 6 nm. Compared to other reported values for calcined anatase-type TiO₂ these measured S_{BET} values are sufficiently high[11,18,19]. This high specific surface area is most likely due to the controlled hydrolysis of the titanium glycolate precursor. Based on the literature[16], it was demonstrated that during hydrolysis, chemical instability of titanium glycolate precursor in aqueous medium enables the outer sphere surface of the material to react with surrounded water molecules, thereby forming thin oxide layers. Furthermore, the formation of cracks due to the density differences between titanium glycolate and thin titanium oxide shells makes inner parts of the sample accessible for further hydrolysis with aqueous media. As a consequence, three-dimensionally interconnected hierarchical nanoporous anatase structures with high specific surface areas can be successfully prepared.

The nitrogen adsorption/desorption isotherm measurement reveal that the calcined np -TiO₂ sample show nanoporous character with typical Type IV behavior with a clear hysteresis loop (Figure 3.1a-b)[20-22], whereas Type I behavior was shown for the as-prepared sample, which is typical for the microporous solids with relatively small external surfaces despite of a small hysteresis loop. The pore size distributions (Figure 3.1a-b insets) illustrate that the np -TiO₂ sample exhibits a relatively narrow pore size distribution (avg. pore diameter *ca.* 6 nm) compared to that for as-prepared np -TiO₂ sample.

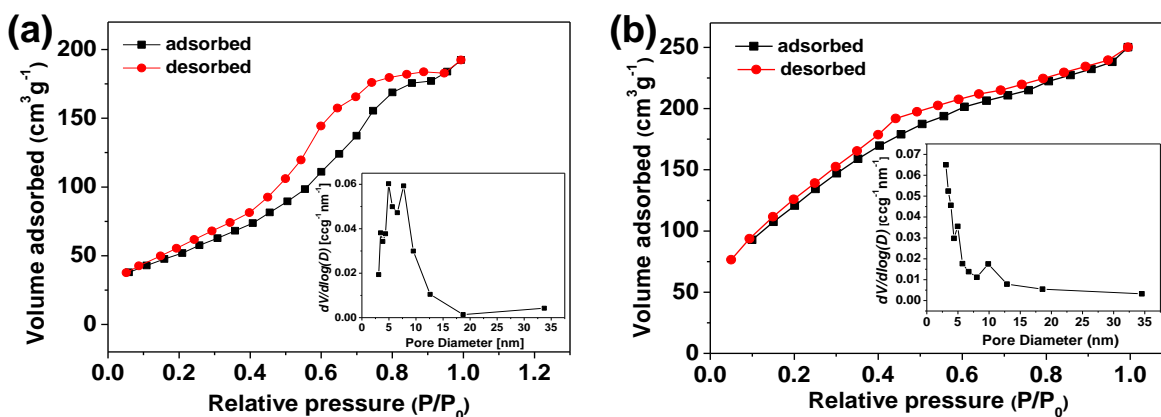


Figure 3.1: Nitrogen adsorption and desorption isotherms of (a) calcined and (b) as-prepared np -TiO₂ with pore diameter distributions of each sample (insets).

Table 3.1: Physicochemical properties of titanium glycolate precursor (TGP), as-prepared and calcined np -TiO₂ samples.

	S_{BET} [m ² g ⁻¹]	Total pore volume [cm ³ g ⁻¹]	Avg. pore diameter [nm]	Crystallite phase	Crystallite size[b] [nm]
TGP [a]	12.1	0.012	4.0	Amorphous	-
np -TiO ₂ (as-prepared)	524.5	0.387	3.2	Anatase	5.1
np -TiO ₂ (calcined)	221.9	0.298	6.0	Anatase	9.5
$comm$ -TiO ₂ (5 – 10 nm)	127.0	0.366	11.5	Anatase	18.8
$comm$ -TiO ₂ (~ 200 nm)	12.7	0.058	18.2	Anatase	265.7

[a] Titanium glycolate precursor

[b] Crystallite size from XRD (WPPD method, Bruker TOPAS)

X-ray diffraction patterns of the titanium glycolate precursor, the as-prepared and calcined np -TiO₂ are shown in Figure 3.2. While the titanium glycolate precursor shows typical amorphous characteristics (with the absence of any particular peaks in the measured angle range), the as-prepared np -TiO₂ sample already exhibits clear peak positions and widths of XRD patterns for the anatase phase (JCPDS, No. 21-1272). The average crystallite size calculated by the WPPD method was *ca.* 5.1 nm (see Table 3.1). There was no phase transformation to the rutile phase even after five hours calcination as XRD patterns still depict the anatase phase. Please note that the two small extra peaks at around 23 and 31 degrees in the diffractogram are assigned to the diffraction with an edge of the sample holder (Al₂O₃, single crystal) and trace amounts of a brookite phase (<211> reflection at $2\Theta=30.83^\circ$) formed during the synthesis, respectively. After the calcination, a significant increase of crystallite size of the sample was not shown (approx. 9.5 nm) with enhanced crystallinity (revealed by the decrease of the full width at half maximum (FWHM) of the peaks). This is due to a thermally stable nature of the obtained nanocrystalline anatase phase[23,24] in which, for particle size on the order of 10 nm or lower, the anatase phase is thermodynamically stable because of the low energy surfaces.

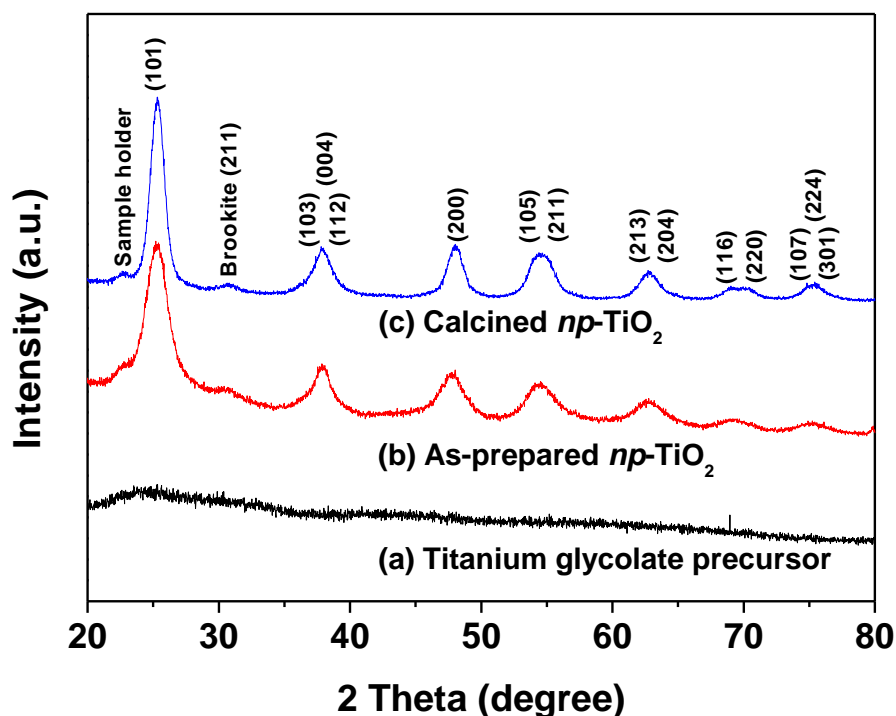


Figure 3.2: XRD patterns of (a) titanium glycolate precursor, (b) as-prepared np -TiO₂, and (c) np -TiO₂ calcined at 673 K for 5 h.

Assuming the prepared crystallites are spherical, the crystallite size can be calculated with the determined specific surface area using the following equation

$$d = 6/\rho S_{\text{BET}} \quad (3.3-1)$$

with d : particle size, ρ : density of TiO₂. This method gives smaller values of the crystallite size (2.9 nm and 6.8 nm for the as-prepared and calcined sample, respectively) but lies in a consistent range with values calculated from XRD.

Figures 3.3c-d show representative FESEM images of calcined and as-prepared np -TiO₂ samples with the respective particle size distribution (insets). At a first glance, it is clearly shown that a single particle is composed of several agglomerated grains with numerous pores inside. An overall particle size for the as-prepared TiO₂ sample was determined as 96.3 nm with a very wide size distribution (40 – 120 nm). Particles grown upon five hours of heat treatment exhibited a particle diameter of *ca.* 75.8 nm but with much narrower diameter distribution (70 – 125 nm). As

3 Effects of Size and Morphology on Lithium Storage

clearly shown in Figure 3.3a-b, HRTEM images confirm the three-dimensional network character of the samples, showing well-interconnected agglomerates of small single crystals (approx. 5 nm) with many nano-sized pores. After the calcination, the mean crystallite size was increased up to approx. 10 nm which is indicative of a grain growth under heat treatment. For all samples, the crystallite size determined using various techniques *e.g.* XRD, S_{BET} , and HRTEM) lies in a similar range. For both samples, SAED patterns (Figure 3.3a-b inset) show the representative polycrystalline anatase nanostructures with multiple concentric circles that can be attributed to different lattice planes of the anatase (*e.g.* (101), (004), (200), and (211)). This confirms that no structural changes of the anatase phase occurred during the calcination.

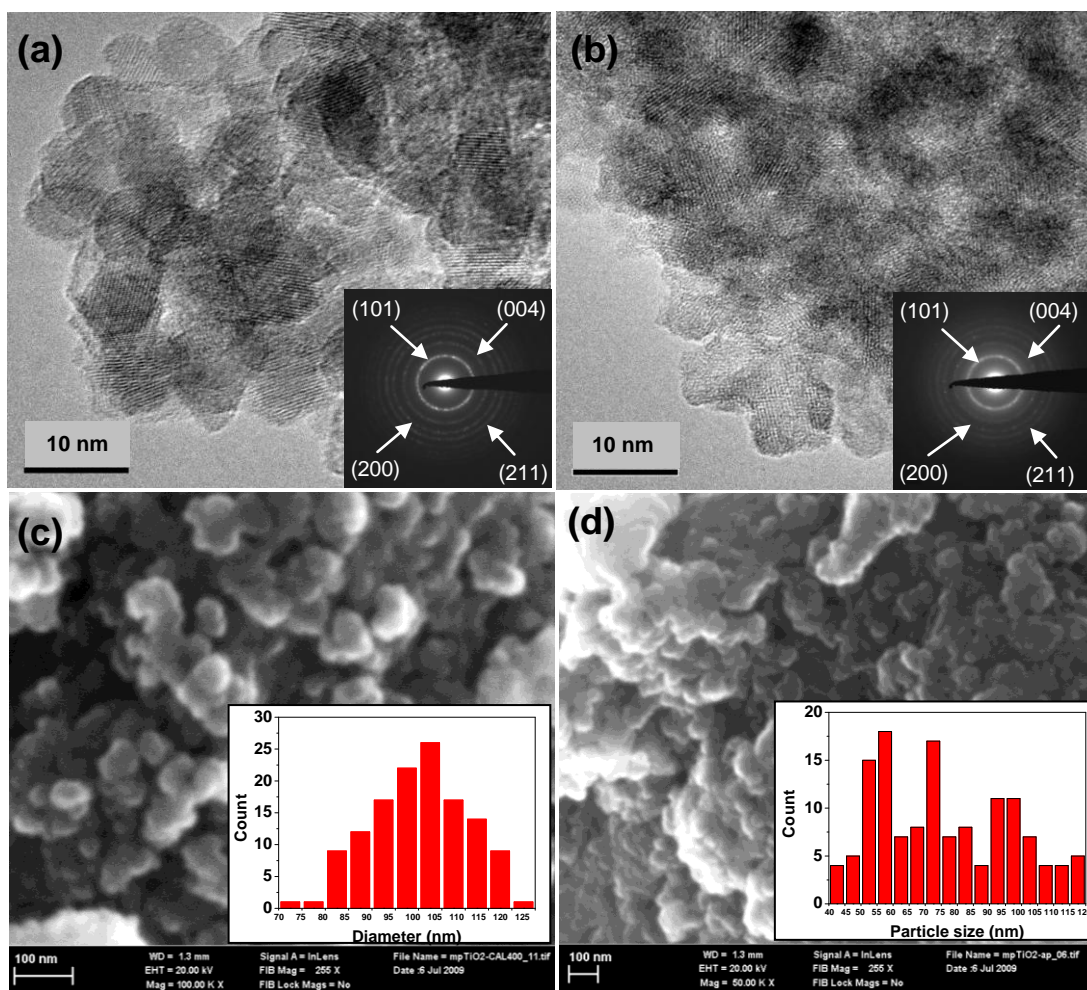


Figure 3.3: HRTEM image of (a) calcined $np\text{-TiO}_2$ with SAED pattern in the inset and (b) as-prepared $np\text{-TiO}_2$ with SAED pattern in the inset. FESEM image of (c) calcined $np\text{-TiO}_2$ and (d) as-prepared $np\text{-TiO}_2$ sample with the particle size distributions (inset).

3.3.2 Electrochemical Analysis: Li Storage Performance

3.3.2.1 Effects of Size and Porosity

Lithium insertion/extraction measurements in the present study were carried out in the potential window of 1-3 V. Figure 3.4a shows the voltage profiles of calcined *np*-TiO₂ for the first 20 cycles at a rate of C/5. The initial capacities upon Li-insertion and extraction were measured as 388.3 and 271.5 mAhg⁻¹ respectively, indicating 30% initial capacity loss. From Karl-Fisher titration measurements, the calculated amount of trace water in the nanoporous TiO₂ sample was determined as *ca.* 8.0 mol%. Such a high amount of trace water inside the *np*-TiO₂ is possible because of adsorption at the high surface area of the nanoporous structure. This might be one possible cause for electrolyte decomposition resulting in capacity loss at initial cycles. However, the coulombic efficiency of *np*-TiO₂ significantly increased almost up to 100 %, showing a perfectly reversible capacity of 242 mAhg⁻¹ at 20th cycle (corresponding to Li_{0.72}TiO₂). In addition, an excellent rate performance (discharge rates between C/5 and 60C) was obtained for the calcined *np*-TiO₂ sample (Figure 3.4b). For a comparison, rate performance of as-prepared *np*-TiO₂ and commercial-TiO₂ (*comm*-TiO₂) with grain sizes of 5 – 10 nm are also shown in Figure 3.4. Their charge capacities at various C rates are summarized in Table 3.2. The charge capacity of *comm*-TiO₂ cycled at C/5 was as small as 118 mAh·g⁻¹, while it was 94 mAhg⁻¹ for the as-prepared *np*-TiO₂ sample. These capacity values only reach less than 70% of the capacity for the calcined nanoporous sample. For rate capability, only the calcined *np*-TiO₂ electrode achieved excellent rate performance compared with the *comm*-TiO₂ and as-prepared *np*-TiO₂ sample being subject to rapid capacity decay at high C rates. Even at very high C rates, the capacities delivered by the calcined *np*-TiO₂ were 77 (30C) and 46 mAhg⁻¹ (60C). As summarized in Table 3.2, capacity retentions after 100 cycles for both nanoporous titania sample (*ca.* 95 %) were better than those of the *comm*-TiO₂ (5 – 10 nm) (*ca.* 90 %). It is noteworthy that not only the rate capability but also the cyclability of *np*-TiO₂ (calcined) electrode are superior compared with the previous work on similar mesoporous structures prepared by a different method[11]. Even without using effective electronically conducting second phases (except small amounts of

3 Effects of Size and Morphology on Lithium Storage

conductive carbon added during electrode preparation, 8:1 $\text{TiO}_2\text{:C}$ in mass), the capacities at low C rates and rate capability of the calcined $np\text{-TiO}_2$ lie in a comparable range with the reported mesoporous $\text{TiO}_2\text{:RuO}_2$ mixed conducting networks[25] in which higher mass fractions of carbon (6:2 in mass) was added in addition to having the conductive RuO_2 network.

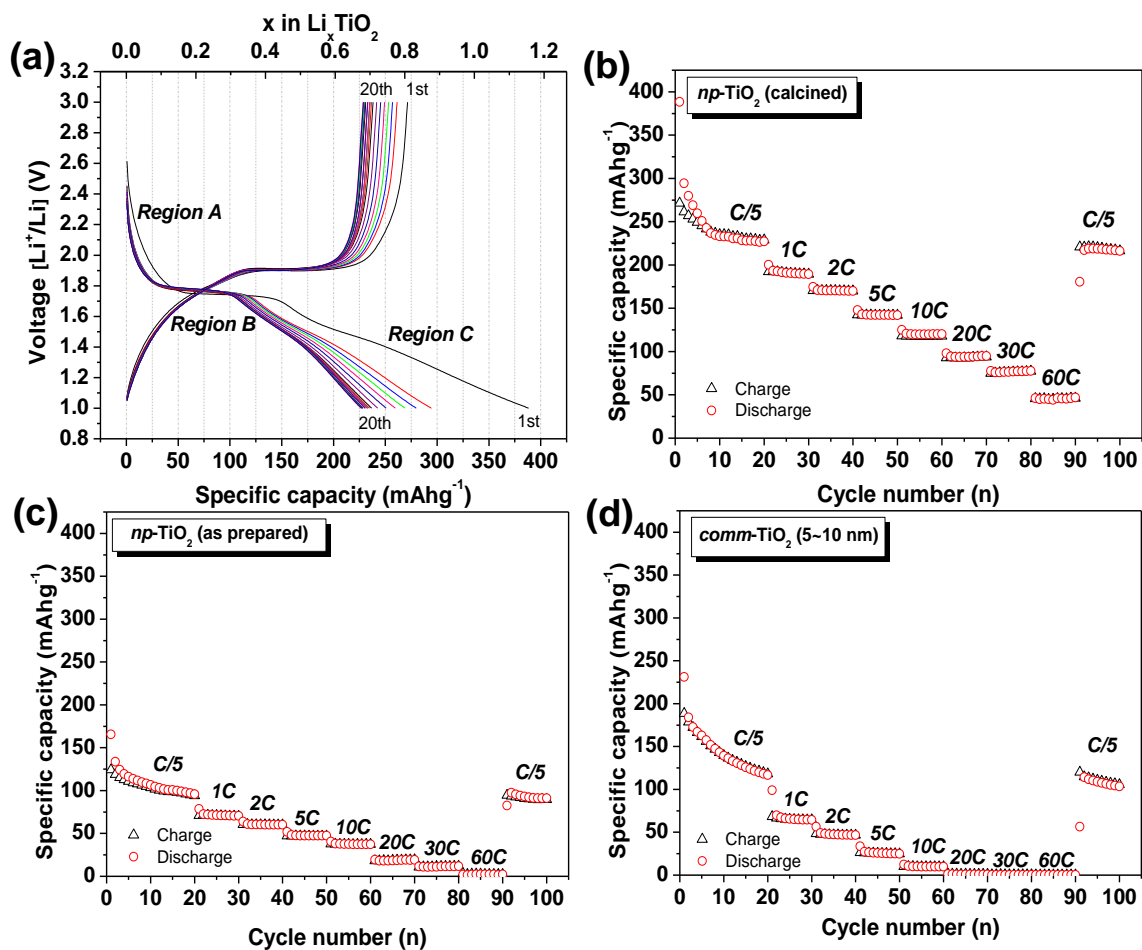


Figure 3.4: (a) Galvanostatic discharge (lithium-insertion)/charge (lithium-extraction) curves vs. Li/Li^+ of calcined $np\text{-TiO}_2$ cycled at a rate of C/5. Rate performance of (b) calcined $np\text{-TiO}_2$, (c) as-prepared $np\text{-TiO}_2$ and (d) $comm\text{-TiO}_2$ (particle size of 5 – 10 nm).

Table 3.2: Summary of the charge capacity [$\text{mAh}\cdot\text{g}^{-1}$] values of commercial TiO_2 , as-prepared and calcined nanoporous TiO_2 sample.

Rate	Pristine- TiO_2 (5-10 nm) [mAhg^{-1}]	Nanoporous- TiO_2 (as-prepared) [mAhg^{-1}]	Nanoporous- TiO_2 (calcined at 673 K) [mAhg^{-1}]	Mesoporous TiO_2 [12] [mAhg^{-1}]	Mesoporous $\text{TiO}_2\cdot\text{RuO}_2$ [25] [mAhg^{-1}]
C/5	118	94	229	210	214
1C	65	70	190	175	190
2C	47	60	170	153	173
5C	25	47	142	117	147
10C	10	37	118	87	123
20C	1	20	94	30	104
30C	0	12	77	10	91
60C	0	2	46	-	-
Capacity retention (after 100 cycles)	90 %	95 %	95 %	-	98 %

Now let me discuss more details of the electrochemical analysis. In Figure 3.5, initial galvanostatic discharge curves (at C/5) of *np*- TiO_2 (calcined) and two different sizes of commercial anatase particles (*ca.* 5 – 10 and 200 nm) are compared.

The discharge curve of the anatase titnia electrode can be divided into three different voltage regions: i) region A– a monotonic voltage drop to ~ 1.75 V (~ 0.20 mol lithium insertion), ii) region B– voltage plateau at ~ 1.75 V, and iii) region C– another monotonic voltage drop beyond the voltage plateau up to the cut-off voltage. The galvanostatic discharge curve shown in Figure 3.4a displays these typical three regions. Region A is attributed to a homogeneous Li insertion into the bulk up to solid solution limit of Li in TiO_2 (less than $\text{Li}_{0.1}\text{TiO}_2$), while region B is indicative of the typical bi-phase plateau ~ 1.75 V where the Li-rich anatase phase and Li-poor orthorhombic Li-titanate phase ($\sim \text{Li}_{0.3}\text{TiO}_2$) co-exists. Before forming of that phase ($\geq \text{Li}_{0.5}\text{TiO}_2$) is completed, I already observe a pseudo-plateau which in the literature is connected with the appearance of Li_1TiO_2 . Beyond these plateaus, further reversible storage of Li seems to occur especially at particle interfaces in region C. One can recognize by comparing galvanostatic curves of two *comm*- TiO_2 nanoparticles that reducing the particle size indeed is effective in improving both bulk intercalation and interfacial storage capacities, (leading to an increase of region B and C respectively). Two features for the 200 nm *comm*- TiO_2 –

i) overvoltages at low C rate (C/5) (which are visible in the region B) and ii) the low Li content at the end of region B further support a reduced electrochemically available volume and higher diffusion resistance for these bigger particles. On the other hand, the plateau voltage for the 5-10 nm *comm*-TiO₂ and the *np*-TiO₂ electrode looks very similar with the end of the plateau being close to the expected bulk limit with Li_{0.5}TiO₂ stoichiometry ($\sim 168 \text{ mAhg}^{-1}$). From this observation, I find that simple downsizing gives rise to a drastic reduction of transport length and rendering more volume available for electrochemical reactions.

Another notable difference for the TiO₂ electrode consisting of smaller primary particle sizes than some 10 nm (*i.e.* *comm*-TiO₂ (5 – 10 nm) and *np*-TiO₂ (9.5 nm) is the presence of a pseudo-plateau at $\sim 1.6 \text{ V}$. Because the Li content at the starting point of this pseudo-plateau is very close to Li_{0.5}TiO₂, the pseudo-plateau is very likely relevant for ongoing intercalation into the orthorhombic phase which involves another phase transition. This transition is probably limited by the size of particles, because phase transformation kinetics in 200 nm particles will most likely be prohibitively slow.

If one compares the voltage profiles of the 5 – 10 nm *comm*-TiO₂ and *np*-TiO₂ electrode, now the first striking difference in the profile is related to region C. In the case of *np*-TiO₂, one recognizes that the storage capacity delivered by region C ($\sim 250 \text{ mAh g}^{-1}$) is almost three times larger than that of the non-porous, commercial material ($\sim 95 \text{ mAh g}^{-1}$). As the particle size of these two samples is almost identical (see Table 3.1) the pore-induced confinement effects might be of prime importance for the interfacial storage reaction occurring after leaving the voltage plateau (region C).

Compared to non-porous type materials with similar grain size, the calcined *np*-TiO₂ sample posses not only a small size but also particularly high surface by means of the enormous number of nanosized-pores. Therefore, beyond the fraction of octahedral sites available for lithium intercalation reaction in the bulk, this hierarchically porous structure most likely provides many available additional sites for lithium accommodation particularly at interfaces. One possible way of interfacial Li storage is *via* the Job-sharing mechanism proposed by Jamnik and

Maier[14] in which Li^+ would be stored in accessible interstitial sites of the oxide's side of the interface, whereas electrons would be stored in a second phase, such as carbon additives or solid electrolyte interface (SEI) layers. The accommodated amount of Li at the surface was calculated for the $np\text{-TiO}_2$ electrode* to be $3.1 \times 10^{-5} \text{ mol m}^{-2}$ which is more than a two times higher value than our previous result for mesoporous anatase[11] and nanometer-sized rutile[3] TiO_2 particles.

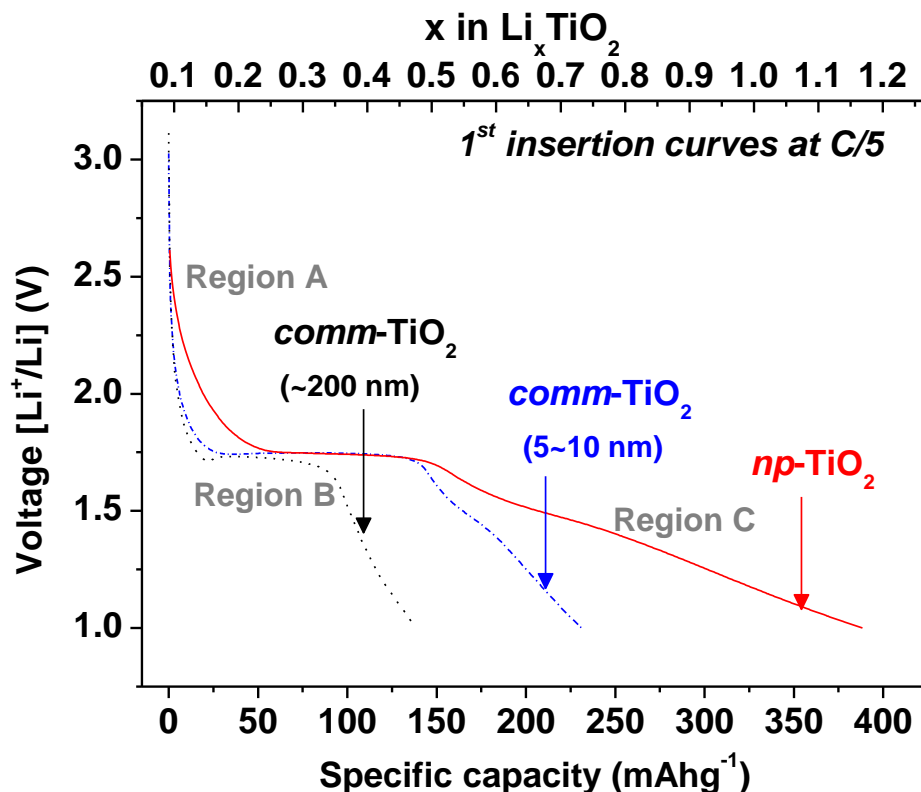


Figure 3.5: Galvanostatic curves of two types of $comm\text{-TiO}_2$ particles with different grain size (~ 200 and $5 - 10$ nm) and calcined $np\text{-TiO}_2$ discharged at $C/5$.

3.3.2.2 Study on Interfacial Li Storage

In the previous section, the observation of interfacial Li storage in the prepared $np\text{-TiO}_2$ sample was described. Now let me extend this to investigating this feature in detail. As a first method, direct cycling of this material at high C rates e.g. $1C$ and $5C$ was performed in order to characterize the kinetic response of $np\text{-TiO}_2$ electrode.

* This is not the real Li content on the surface, but the content of Li residing in the interfacial layer. Since we do not know an exact content, we related the Li content to the surface area.

Here I assume that the reaction kinetics of an interfacial storage mechanism is faster than bulk intercalation which accompanies phase changes. Therefore under high current densities the interface-based storage mechanisms might be more emphasized, whereas the bulk TiO_2 is prevented from being discharged above the $\text{Li}_{0.5}\text{TiO}_2$ threshold, where a part of further bulk intercalation reactions could become irreversible. With this assumption, it is expected that the material is subject to less degradation and capacity fading. Figure 3.6 shows charge/discharge capacities for calcined $np\text{-TiO}_2$ with increased number of cycles at fixed rates 1C (Figure 3.6a) and 5C (Figure 3.6b).

The direct cycling provided fully reversible capacities of 302 mAh g^{-1} (at 1C) and 229 mAh g^{-1} (at 5C) after 100 cycles. These capacity values are much higher than those determined by the stepwise cycling (Figure 3.6c). In addition, one can easily recognize that compared to the cycling at low rate (0.2C), much less degradation is observed when the materials are cycled at high rates. This phenomenon supports well the hypothesis that interfacial storage is strongly preferred at relatively high C rates *i.e.* 1C or 5C rather than 0.2C.

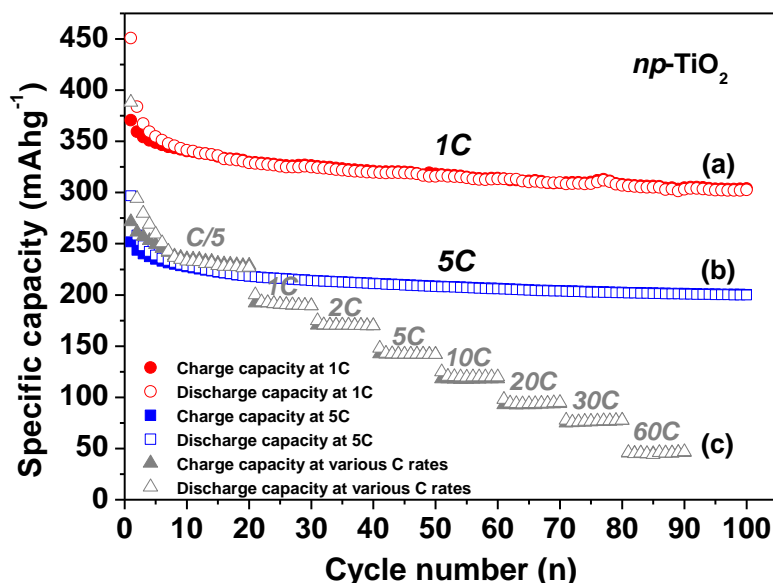


Figure 3.6: Charge/discharge capacities versus number of cycles for the calcined $np\text{-TiO}_2$ (dis)charged directly at a rate (a) 1C (charge/discharge to theoretical capacity within 1 h), and (b) 5C (charge/discharge to theoretical capacity within 12 min). (c) Charge/discharge capacities when the material (dis)charged with rates ascending stepwise from C/5 to 60C.

Figure 3.7 compares galvanostatic voltage profiles of the *np*-TiO₂ electrode at various discharge rates upon the first and 20th insertion cycle. Upon the first insertion process (Figure 3.7a), the proportions ($\sim 55 \pm 5$ %) of the voltage tail (region C) appear almost identical for all three rates. In detail, at C/5 a more distinct pseudo-plateau (~ 1.6 V) was observed due to the occurrence of further Li intercalation under slow insertion rate. However, under high insertion rates *i.e* 1C and 5C this pseudo-plateau was found to vanish. This is indicative of the dominance of the interfacial storage reaction at high C rates. Interestingly, the region C in the voltage profile at 5C resembles a straight line, most likely due to a purely capacitive storage characteristic. The capacity delivered during the initial Li-insertion process at 1C is significantly higher ($451 \text{ mAh}\cdot\text{g}^{-1}$) than that delivered at C/5 ($388 \text{ mAh}\cdot\text{g}^{-1}$). Particularly the disappearance of the pseudo-plateau (existed at ~ 1.6 V) under high current density condition is consistent with my hypothesis that cycling at high rates can provide more emphasis on interfacial storage reactions.

On the other hand, a large capacity loss (50 %) was observed after 20 cycles (Figure 3.7b) at C/5, whereas only 15 and 27 % capacity loss occurs at 1C and 5C, respectively. If one compares the shape of voltage curves at the 20th cycle (Figure 3.7b) to the first discharge cycle, it is shown that at high rates (1C and 5C), the pseudo-plateau has fully vanished, but no other severe changes in voltage shape occur. The interfacial Li storage contribution is still predominant after 20 cycles at high rates as in both cases the voltage profiles still maintain the large proportion of region C. However, after 20 cycles a considerable decrease of region C capacity was found in the voltage profile at C/5. This ultimately results in the large decay of overall capacity as the cycle number increases. As the shape of the region C for *np*-TiO₂ at 20th cycle (C/5) seems to be similar to that of the first C/5 discharge cycle profile of 5-10 nm *comm*-TiO₂, changes in the nanoporous structure might have occurred. The structural changes in the bulk after intercalating more than 0.5 Li per TiO₂ probably lead to a partial loss of the nanoporous structure of the *np*-TiO₂ after several cycles, and thus the fraction of interfacial storage capacity might decrease. Then the capacity delivered by region B drastically decreases after 20

3 Effects of Size and Morphology on Lithium Storage

cycles at $C/5$. This is in accordance with the previously mentioned sluggish nature and partially irreversible character of the reaction kinetics for Li inserted above the $\text{Li}_{0.5}\text{TiO}_2$ threshold, leading to an effective decrease of available bulk intercalation sites[5].

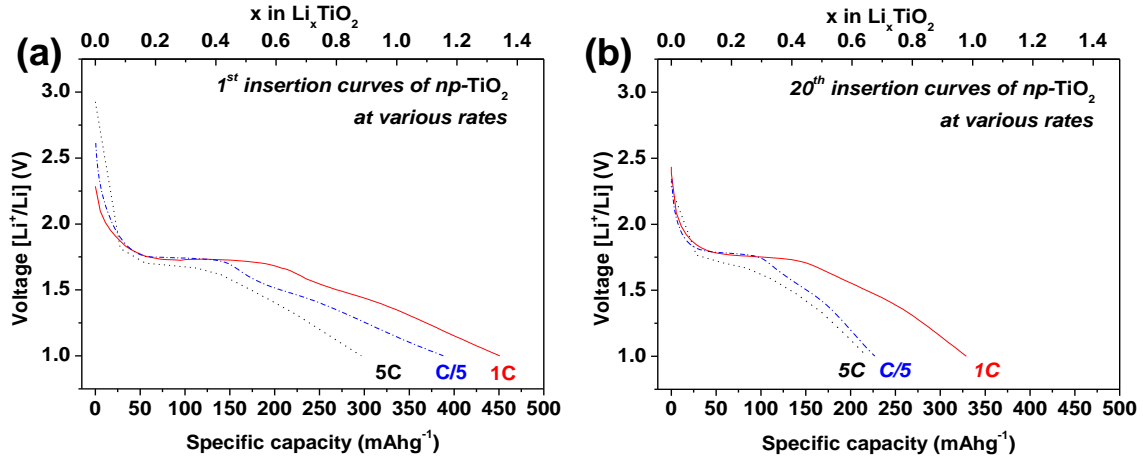


Figure 3.7: Voltage profiles of $np\text{-TiO}_2$ electrode at various C rates ($C/5 - 5C$) during (a) first and (b) 20th discharge process.

The electrochemical analyses of the Li insertion mechanisms into $np\text{-TiO}_2$ with sufficiently high surface area described above are summarized in Figure 3.8. At a first glance, one recognizes that two insertion mechanisms– i) bulk transition to the orthorhombic phase, with further Li intercalation above $x > 0.5$, and ii) interfacial storage are the storage processes after leaving the voltage plateau at ~ 1.75 V (region B). Here I demonstrate that these two storage mechanisms act in a consecutive way, because Li^+ first might penetrate the interfacial region before being able to enter the bulk. Compared to the sluggish bulk transition, Li^+ is predominantly stored in the interfacial regions especially at high C rates because bulk transport cannot keep up with the applied galvanostatic current[26]. Therefore, a continuous cycling of the materials keeps Li^+ ions at the interfaces, resulting in very little bulk degradation. This non-equilibrium condition must relax during an extended rest-period, and bulk degradation will occur.

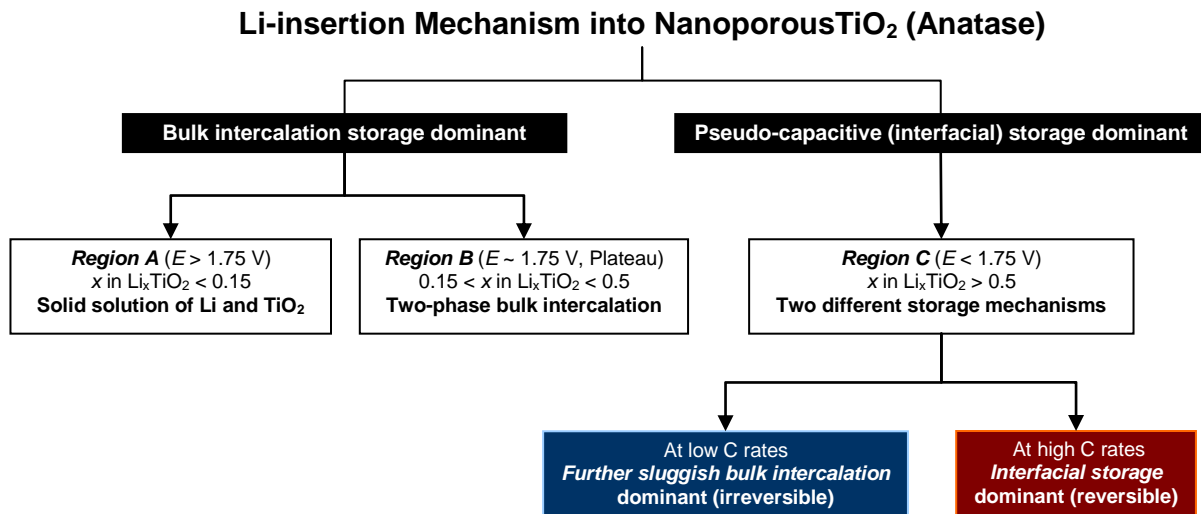


Figure 3.8: Proposed overall Li-insertion mechanism into nanoporous TiO₂ (anatase) structure with high surface area.

3.4 Conclusion

In short, this chapter has proven the importance of size and morphology of anode material to the overall lithium storage properties. The concept of nano-structuring by means of the hierarchical nanoporous TiO₂ (anatase) particles with high surface area was applied. The materials were prepared by a simple hydrolysis method without any further templates (that can hamper the Li storage performance); their electrochemical Li-storage properties were studied. The prepared material showed a significantly high specific surface area of *ca.* 222 m²g⁻¹ with a crystallite size of *ca.* 9 nm. Due to the drastically reduced transport length, the nanoporous TiO₂ could deliver not only high charge/discharge capacity but also much improved rate capability compared to non-porous electrode systems. The lithium storage property of the nanoporous TiO₂ was sustained with almost negligible capacity decays even at high lithium insertion/extraction rates, such as 30C and 60C. Two different storage mechanisms— interface-based and regular bulk intercalation mechanisms were recognized and compared under various Li-insertion/extraction condition *i.e.* C rates and cycle numbers. It was found that a use of not only small sized particles but also highly porous structures is advantageous for achieving high interfacial

storage. Moreover, the energy density of the nanoporous material increases compared to bulk TiO_2 not only because of increased capacities, but also due to the earlier onset of region C interfacial storage, giving rise to lower average anode potential.

I further confirmed the nature of interfacial storage behavior of Li in the hierarchical nanoporous TiO_2 (anatase) by charging/discharging the material in two different ways- direct insertion/extraction of Li at high rates and stepwise insertion/extraction of Li from low to high rates. The direct insertion/extraction of Li at high rates (without cycling at low rates) gives a significant capacity increase, compared to that cycled at various rates changing from low to high rates. On the basis of the performed electrochemical analysis, this can be ascribed to the fact that Li^+ is predominantly stored in the interfacial regions rather than in the bulk of titania, since storage kinetics of the interfacial storage is probably much faster than for the two-phase intercalation reaction (based on solid-state diffusion of Li in bulk materials). The high surface area and the presence of uniformly nanosized pores therefore play a very important role for the interfacial Li storage reaction.

As a consequence, this study illustrates that nano-structuring is beneficial not only to effectively reduce transport lengths but also to enhance (pseudo-capacitive) interfacial Li storage. This strategy improves the overall storage performance and further offers the potential to design ultrafast charge/discharge electrode materials.

References

- [1] L. Kavan, J. Procházka, T. M. Spitler, M. Kalbá, M. Zúkalová, T. Drezen, M. Grätzel, *J. Electrochem. Soc.* **2003**, *150*, A1000.
- [2] G. Sudant, E. Baudrin, D. Larcher, J.-M. Tarascon, *J. Mater. Chem.* **2005**, *15*, 1263.
- [3] Y.-S. Hu, L. Kienle, Y.-G. Guo, J. Maier, *Adv. Mater.* **2006**, *18*, 1421.
- [4] M. Wagemaker, W.J.H. Borghols, E.R.H. van Eck, A.P.M. Kentgens, G.J. Kearley, F.M. Mulder, *Chem. Eur. J.* **2007**, *13*, 2023.
- [5] M. Wagemaker, W.J.H. Borghols, F.M. Mulder, *J. Am. Chem. Soc.* **2007**, *129*, 4323.
- [6] N. Sata, K. Eberman, K. Eberl, J. Maier, *Nature* **2000**, *408*, 946.
- [7] J. Maier, *Nature Mater.* **2005**, *4*, 805.
- [8] A.S. Arico, P. Bruce, B. Scrosati, J.-M. Tarascon, W. van Schalkwijk, *Nature Mater.* **2005**, *4*, 366.
- [9] P. Balaya, A.J. Bhattacharyya, J. Jamnik, Y.F. Zhukovskii, E.A. Kotomin, J. Maier, *J. Power Sources* **2006**, *159*, 171.
- [10] Y.-S. Hu, Y.-G. Guo, W. Sigle, S. Hore, P. Balaya, J. Maier, *Nature Mater* **2006**, *5*, 713.
- [11] Y.-G. Guo, Y.-S. Hu, J. Maier, *Chem. Commun.* **2006**, 2783.
- [12] Y.-S. Hu, P. Adelhelm, B. Smarsly, S. Hore, M. Antonietti, J. Maier, *Adv. Funct. Mater.* **2007**, *17*, 1873.
- [13] H.-K. Song, K. T. Lee, M. G. Kim, L. F. Nazar, J. Cho, *Adv. Funct. Mater.* **2010**, *20*, 3818.
- [14] J. Jamnik, J. Maier, *Phys. Chem. Chem. Phys.* **2003**, *5*, 5215.
- [15] J. Maier, *Faraday Discuss.* **2007**, *134*, 51.
- [16] L.-S. Zhong, J.-S. Hu, L.-J. Wan, W.-G. Song, *Chem. Commun.* **2008**, 1184.
- [17] J. Wang, J. Polleux, J. Lim, B. Dunn, *J. Phys. Chem. C* **2007**, *111*, 14925.
- [18] H.-G. Jung, S.W. Oh, J. Ce, N. Jayaprakash, Y.-K. Sun, *Electrochem. Commun.* **2009**, *11*, 756.
- [19] P. Kubiak, J. Geserick, N. Hüsing, M. Wohlfahrt-Mehrens, *J. Power Sources* **2008**, *175*, 510.

- [20] S. Brunauer, L.S. Deming, W.E. Deming, E. Teller, *J. Am. Chem. Soc.* **1940**, *62*, 1723.
- [21] J. Rouquerol, D. Avnir, C.W. Fairbridge, D.H. Everett, J.M. Haynes, N. Pernicone, J.D.F. Ramsay, K.S.W. Sing, K.K. Unger, *Pure Appl. Chem.* **1995**, *66*, 1739.
- [22] K.S.W. Sing, D.H. Everett, R.A.W. Haul, L. Moscou, R.A. Pierotti, J. Rouquérol, T. Siemieniowska, *Pure Appl. Chem.* **1985**, *57*, 603.
- [23] E.L. Crepaldi, G.J. de A.A. Soler-Illia, D. Grosso, F. Cagnol, F. Ribot, C. Sanchez, *J. Am. Chem. Soc.* **2003**, *125*, 9770.
- [24] H. Zhang, J.F. Banfield, *J. Mater. Chem.* **1998**, *8*, 2073.
- [25] Y.-G. Guo, Y.-S. Hu, W. Sigle, J. Maier, *Adv. Mater.* **2007**, *19*, 2087.
- [26] A. Van der Ven, Elucidating the kinetics of complex Li insertion reactions in Li batteries, abstract #EMA-S4-010-2012, Meeting: Electronic Materials and Applications, Orlando, January 2012.

4

Effects of Defect Chemistry on Lithium Storage I.

Case Study of Frozen-in Native Defects

This section deals with effects of defect chemistry on lithium storage behavior of nanostructured anatase TiO_2 . In the first part (Chapter 4.3), the concept of frozen-in native defects by realizing oxygen-deficient $\text{TiO}_{2-\delta}$ nanoparticles with excess electronic charge carriers, and its impact on lithium storage properties is discussed. In the latter half (Chapter 4.4), a systematic defect chemical analysis of lithium storage in oxygen-deficient $\text{TiO}_{2-\delta}$ is discussed and the impact of defect chemistry (charge carriers concentrations) on the overall electrochemical lithium storage performance is emphasized.

4.1 Introduction

Even though many new electrode materials which are both environmentally-benign and structurally stable have been reported, their electrochemical properties for lithium storage are still limited by poor chemical diffusion of lithium. This limitation results from i) the slow lithium ion diffusion and/or ii) the poor electronic conductivity. Especially, the latter one – the improvement of electron transport kinetics in electrode particles – has been widely studied[1-3]. Most efforts to improve electron transport kinetics has focused on conductive coating by amorphous carbon[4-5] or decorating with other types of conductive second phases, for example carbon nanotubes[6], graphene[7] and nano-sized metal (oxide) particles[8,9]. However, large amounts of secondary phases (up to ≈ 30 vol.% for randomly distributed second phase particles of equal size) are required sometimes to form a percolating network for providing efficient electron transport. Additionally, open and percolating porosity with again a high volume demand might be required for providing Li^+ transport through electrolyte penetrating the pores. Consequently, it becomes hard to prepare percolating networks of three different phases (lithium host materials, voids/pores, and secondary phases) in the composite electrode system that would be essential for a good electrode performance. As far as materials preparation is concerned, chemically or physically admixing the conductive additives in a homogeneous manner especially with nano-sized lithium host materials is nontrivial. Moreover, side reactions within the operation voltage window can be triggered by the presence of a second phase. Therefore, increasing electronic charge carrier concentration of active materials without using second phases can be a more attractive approach to improve the electronic transport. The concept of ‘homogeneous lattice doping’ (dissolution within solid-solution limit) has been considered a powerful means taken to tune transport properties. Various effects of doping have been reported in the literature[10-18].

While defect chemical studies of oxide materials including TiO_2 as a function of temperature or oxygen partial pressure (P_{O_2}) have been extensively studied in the

context of high temperature chemistry, systematic defect chemical studies particularly in terms of lithium storage in oxide based electrodes for lithium batteries are – in spite of the paramount importance – almost absent in the literature. One exception is the detailed study of the redox-pair $\text{LiFeO}_4\text{-FePO}_4$ for which the charge carrier chemistry has been explained as a function of lithium activity (a_{Li}), temperature (T) and doping concentration (C)[19-21]. According to these studies, establishing a defect model in LiFePO_4 is the ultimate goal of a thermodynamic treatment of the charge carrier chemistry. This is because such studies are of importance in clarifying not only the nature of the electronic and ionic defects but also the variations of their concentrations as a function of the control parameters (a_{Li} , T , and C). For example, Amin *et al.*[19] reported on lithium ion conductivity and diffusivity of Aluminum-doped LiFePO_4 single crystals in which the ionic conductivity has increased while the electronic conductivity has decreased compared to undoped LiFePO_4 (donor doping effect). In addition, the temperature dependence of ionic conductivity and of lithium diffusivity was interpreted by a detailed defect chemical analysis in terms of lithium vacancies, holes, and associates. This study revealed that ionic-electronic as well as ionic-ionic defect associations play a significant role in the LiFePO_4 electrode system. In this regard, the motivation of this Chapter is to advance a fundamental understanding of charge carriers concentrations effects on lithium storage properties to emphasize the importance of point defect chemistry of lithium storage in the anode material TiO_2 . Two different situations– frozen-in native defects and doping with extrinsic defects are studied in Chapter 4 and 5, respectively.

4.2 Concept: Frozen-in Native Defects

As far as the defect structure of TiO_2 is concerned, the oxygen content depends significantly on temperature and surrounding oxygen atmosphere. For example, Weibel *et al.* reported a systematic interpretation of the point defect chemistry of anatase TiO_2 as a function of temperature and oxygen partial pressure[22]. The

point defect chemistry of undoped TiO_2 at elevated temperatures was considered in terms of oxygen vacancies, titanium interstitials, and titanium vacancies. Predominant types of defects are mainly dependent on temperature and/or oxygen partial pressure. Using defect chemical reactions, related physical properties *i.e.* electrical conductivity can be established at high temperatures, where charge carrier concentrations are in complete equilibrium. Because many practical applications including lithium batteries are however usually operated at room temperature where the interaction of oxides with surrounding gas phase is no longer reversible, the physical properties of materials may be controlled at temperatures lower than those at which defects *e.g.* oxygen nonstoichiometry are formed. This means that if a quenching of the high temperature defect-situation succeeds, parts of the internal defect equilibrium reactions may be still reversible at room temperature (so-called partially frozen-in state). So far, only little is reported on the careful consideration of the defect chemistry at low temperatures, despite their significance[23-24]. One study by Maier[25] gives a particularly clear treatment of cases in which frozen-defect chemistry is of significance. This is very important from an application point of view.

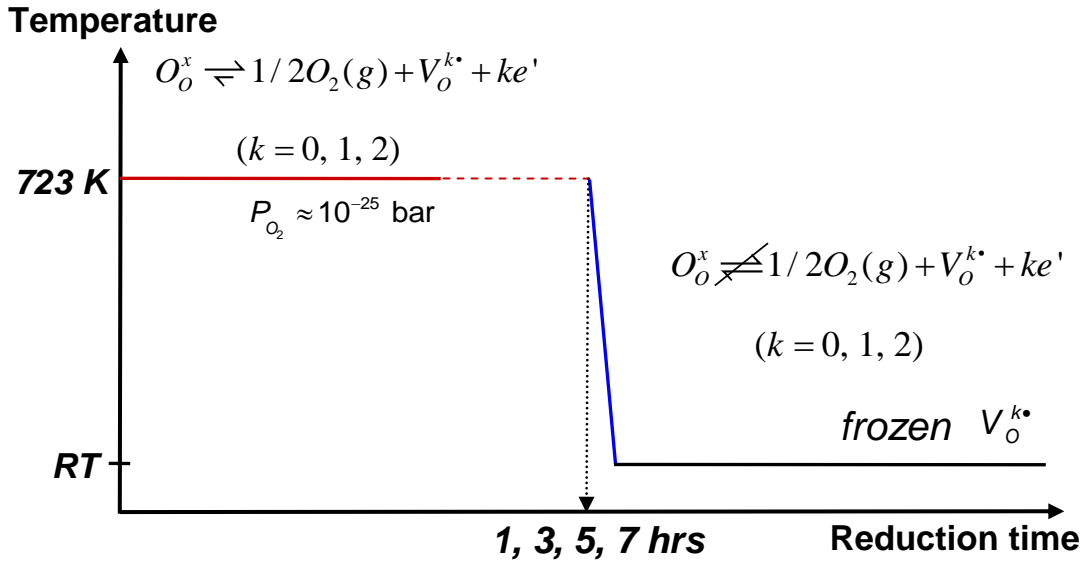
While doping with foreign elements (it is discussed in Chapter 5) is the usual approach taken to improve the electrochemical properties, only little is reported on the alternative strategy of introducing frozen native defects (*e.g.* frozen oxygen nonstoichiometry in oxides)[26]. This is surprising as this strategy is simple and provides benefits by avoiding side reactions. Furthermore, a systematic treatment of using native doping on electrochemical lithium storage properties has not been given at all. In this Chapter, effects of frozen-in native defects *i.e.* oxygen nonstoichiometry (established at high temperature and quenched to room temperature) on mass transport and storage in Li-batteries are systematically studied *via* not only multiple experimental techniques (Chapter 4.3) but also theoretical defect chemical analysis (Chapter 4.4).

4.3 Experimental Results

4.3.1 Materials Preparation

Materials: In this study, commercially available anatase TiO₂ nanopowders (MTI Co., U.S.A., $d \approx 50$ nm (specified)) are used. Particle size characterization gives real particle diameters approx. 20 nm.

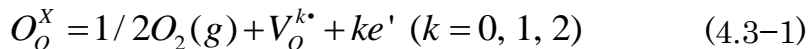
Hydrogen thermal treatment of TiO₂: As shown in Scheme 4.1, the commercially available titania nanoparticles (*ca.* 20 nm) first underwent a pre-treatment for 30 min at 573 K in a cylindrical electric furnace to remove impurities, *e.g.* organic residues from synthesis or handling and adsorbed water, under pure Ar (purity 99.999 %). The pre-treated sample was then heated up to 723 K under pure Ar at a gradient rate of 10 K min⁻¹. The Ar flow rate was fixed as 20 ml min⁻¹. For reducing the pre-treated sample, 5% H₂ / 95% Ar gas mixture was subsequently introduced with a flow rate of 72 ml min⁻¹ at 723 K and was heated for different time periods (1 – 7 h). The gas was deliberately switched again to pure Ar and temperature decreased to room temperature with the same gradient rate of 10 K min⁻¹. In order to avoid re-oxidation of materials, the prepared oxygen-deficient TiO_{2- δ} sample was allowed to be taken out from the Ar atmosphere when it was completely cooled down to room temperature. Not only H₂-treated oxygen-deficient TiO_{2- δ} samples, but also another set of samples was prepared by treating with the same thermal treatment condition, but without exposure to reducing gas. The nomenclature of the prepared samples is the following: i) *H₂- n h-TiO_{2- δ}* for titania nanoparticles thermally annealed under 5 % H₂/95 % Ar ($P_{O_2} \approx 10^{-25}$ bar) for n hours (n being 0, 1, 3, 5, or 7) (see Scheme 4.1). ii) *Ar-1h-TiO_{2- δ}* and *Ar-7h-TiO_{2- δ}* for thermally annealed anatase nanoparticles in inert condition (99.999 % Ar, $P_{O_2} \approx 10^{-5}$ bar) for 1 and 7 h, respectively.



Scheme 4.1: Schematic illustration of experimental procedure for the preparation of oxygen-deficient $\text{TiO}_{2-\delta}$ nanoparticles.

4.3.2 Results and Discussion

Please note that the initial oxygen deficiencies of the commercial, untreated anatase nanoparticles compared with the oxygen deficiency introduced by H_2 reduction are neglected. As briefly mentioned previously, titanium dioxide can tolerate quite high oxygen deficiencies ($\text{TiO}_{2-\delta}$) either by removal of oxygen from the anion sub-lattice (leaving oxygen vacancies), or by formation of titanium interstitials[27]. (If the oxygen deficiency δ is too high, so-called Magnéli phases can form[28]). On the basis of the phase diagram as a function of oxygen partial pressures and temperatures, oxygen vacancies (rather than titanium interstitials) are most likely the predominant types of defects that can be formed upon the performed H_2 -thermal treatment (reducing condition: $P_{\text{O}_2} \approx 10^{-25}$ bar at temperature 723 K)[22]. It is worthy of note in this thesis that one should consider not only fully ionized vacancies ($V_o^{\bullet\bullet}$), but also singly ionized (V_o^{\bullet}) or even neutral ones, (V_o^x) as the oxygen vacancies can easily be associated with electrons at room temperature. The reduction reaction can be expressed in Kroger-Vink notation as follows:



It is proven to be a good approximation to consider the overall oxygen deficiency determined by the performed thermal reduction to be frozen. As a result, the n -type electronic carrier concentration increases. Then the electro-neutrality in pure material follows as $[e'] = 2[V_O^{**}] + [V_O^*]$. As the main conclusions should be independent of the nature of the compensating ionic majority defect, hydrogen incorporation (OH_O^*) is not explicitly considered but would lead to similar consequences. Moreover, as protons typically have a higher mobility than oxygen vacancies, the fact that defects are clearly frozen is a strong support for oxygen vacancies to be the dominant ionic defects.

4.3.2.1 Structural Characterization

Figure 4.1 shows powder X-ray diffraction (XRD) patterns of pristine TiO_2 , Ar - $1h$ - $TiO_{2-\delta}$, H_2 - $1h$ - $TiO_{2-\delta}$, and H_2 - $7h$ - $TiO_{2-\delta}$ samples. The non-treated TiO_2 sample shows typical peaks for anatase with a space group of $I4_1/amd$ (JCPDS, No. 21-1272). As shown in the XRD pattern of Ar - $1h$ - $TiO_{2-\delta}$ and H_2 - $1h$ - $TiO_{2-\delta}$ sample, no phase transition to other phases *i.e.* rutile occurred upon one hour of thermal treatment. Even after the prolonged thermal annealing (7 h), the materials still maintained the anatase phase. At given annealing temperature (723 K), fluctuation of Ti and O atoms in anatase are not strong enough to generate rutile nuclei (on the surface or in the bulk) even for the prolonged annealing process. The XRD lattice parameters for pristine anatase TiO_2 and for all Ar - and H_2 -treated samples are shown in Table 4.1. A slight increase in the lattice parameters was shown upon reduction due to a lattice expansion upon reduction from Ti^{4+} to Ti^{3+} . The crystallite sizes and specific surface areas of Ar -annealed and H_2 -thermally treated samples are summarized in Figure 4.2 and Table 4.1. It is clearly shown that upon 1 h gas treatments, the crystallite size of pristine TiO_2 (17 ± 3 nm) sample was increased to 29 ± 5 nm. However, regardless of gas atmosphere further significant increase in the crystallite size was not observed even after prolonged treatments (1 – 7 h). The grain growth is limited by Ti and O mobility as well, and slow growth kinetics for isothermal grain growth at 723 K[29] can be the reason for the similarity in

crystallite size for the 1 h- and 7 h-treated samples. As shown in Figure 4.2a-b, the determined BET surface area values gave a consistent result with the variation of crystallite size as a function of treatment time, showing a slightly decreased S_{BET} after 1 h treatment, but no further changes upon extended annealing times. As shown in Figure 4.3, HRTEM images also correlate well with the crystallite size determined from XRD and S_{BET} .

Table 4.1: Space group, crystallite size from XRD analysis, unit cell parameters, and BET surface area for pristine anatase TiO_2 , and for all $\text{TiO}_{2-\delta}$ samples.

	Pristine TiO_2	Ar-1h- $\text{TiO}_{2-\delta}$	Ar-7h- $\text{TiO}_{2-\delta}$	H_2 -1h- $\text{TiO}_{2-\delta}$	H_2 -3h- $\text{TiO}_{2-\delta}$	H_2 -5h- $\text{TiO}_{2-\delta}$	H_2 -7h- $\text{TiO}_{2-\delta}$
Space group	$I4_1/amd$	$I4_1/amd$	$I4_1/amd$	$I4_1/amd$	$I4_1/amd$	$I4_1/amd$	$I4_1/amd$
Crystallite size [nm]	17 ± 3	29 ± 5	29 ± 5	29 ± 5	28 ± 6	28 ± 6	29 ± 5
Lattice parameters [Å]	a 3.787 c 9.509	a 3.790 c 9.520	a 3.790 c 9.521	a 3.790 c 9.523	a 3.792 c 9.523	a 3.792 c 9.524	a 3.791 c 9.524
S_{BET} [m^2/g]	174.1	160.6	160.8	153.7	155.4	151.7	150.8

As a consequence, as a function of the annealing time (at the fixed temperature 723 K) the change in physicochemical parameters of titania can be negligible. Nevertheless, only the small change of the overall particle interconnectivity induced by the thermal annealing have to be considered (see SEM images). Figure 4.4 indicates that particles are gradually agglomerated with increasing treatment time, regardless of the types of treatment gas. On the other hand, the color change from pure white to light yellowish after 1h of hydrogen thermal treatment supports the partial reduction of the material (Figure 4.4c, inset), as no color change was visible for Ar-7h- $\text{TiO}_{2-\delta}$ (Figure 2b, inset). The dark yellow color of the H_2 -7h- $\text{TiO}_{2-\delta}$ sample (Figure 4.4d, inset) also reveals a strong reduction of material.

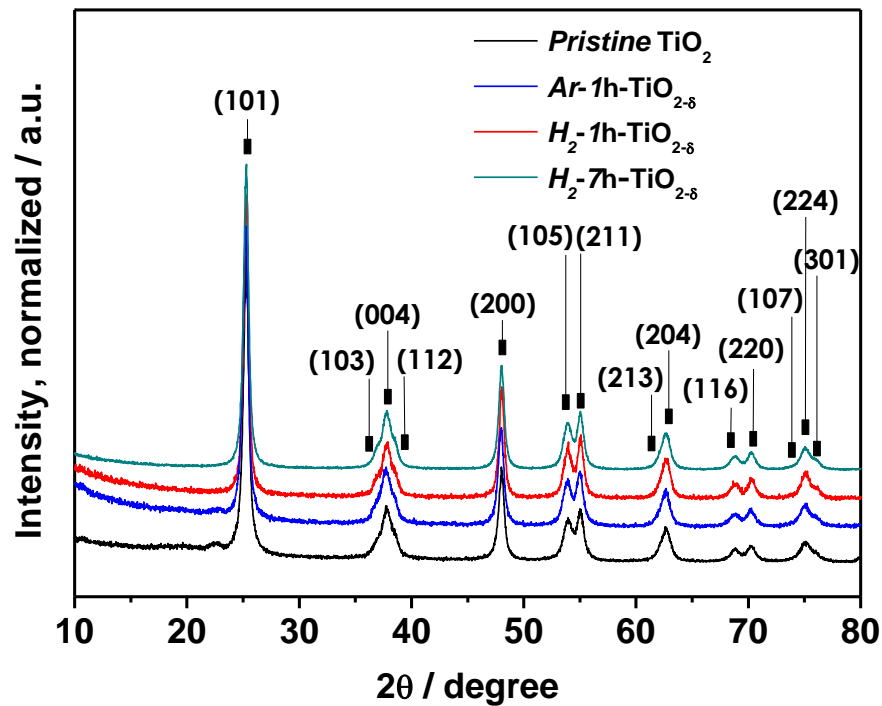


Figure 4.1: Powder X-ray diffraction pattern of pristine TiO_2 , $\text{Ar-1h-TiO}_{2-0.8}$, $\text{H}_2\text{-1h-TiO}_{2-0.8}$, and $\text{H}_2\text{-7h-TiO}_{2-0.8}$.

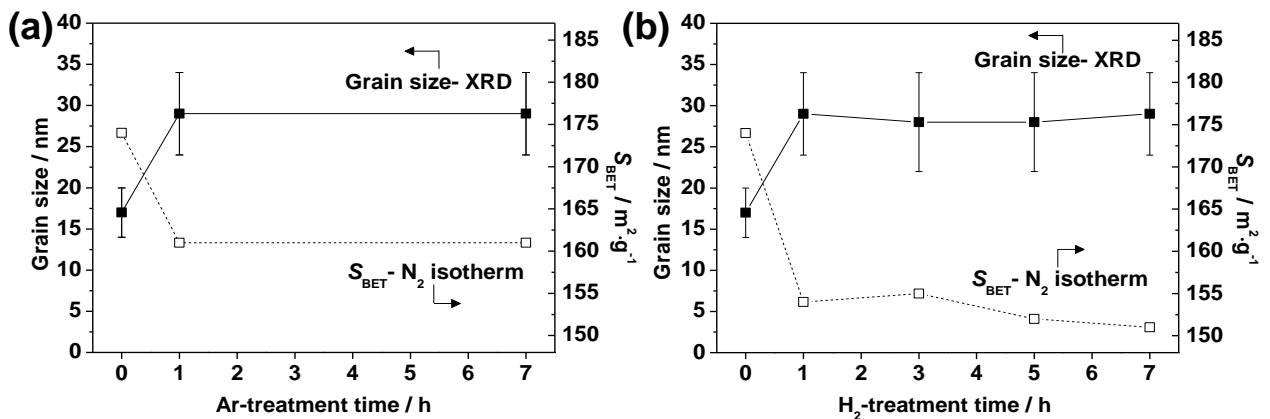


Figure 4.2: Variation of grain sizes (determined by XRD) and BET surface area (determined by N_2 isotherm) upon (a) Ar-annealing and (b) H_2 -thermal treatment as a function of treatment time.

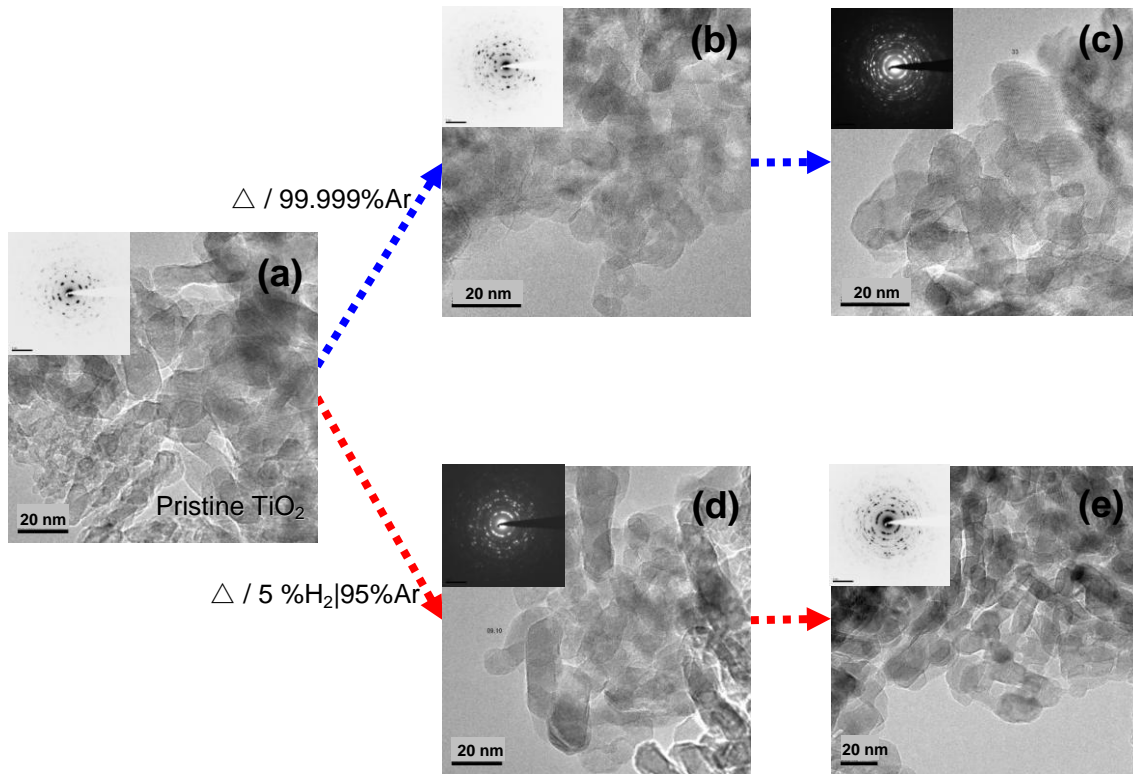


Figure 4.3: HRTEM images of (a) pristine TiO₂, (b) *Ar* 1h-TiO_{2-δ}, (c) *Ar* 7h-TiO_{2-δ}, (d) *H₂* 1h-TiO_{2-δ} and (e) *H₂* 7h-TiO_{2-δ} nanoparticles.

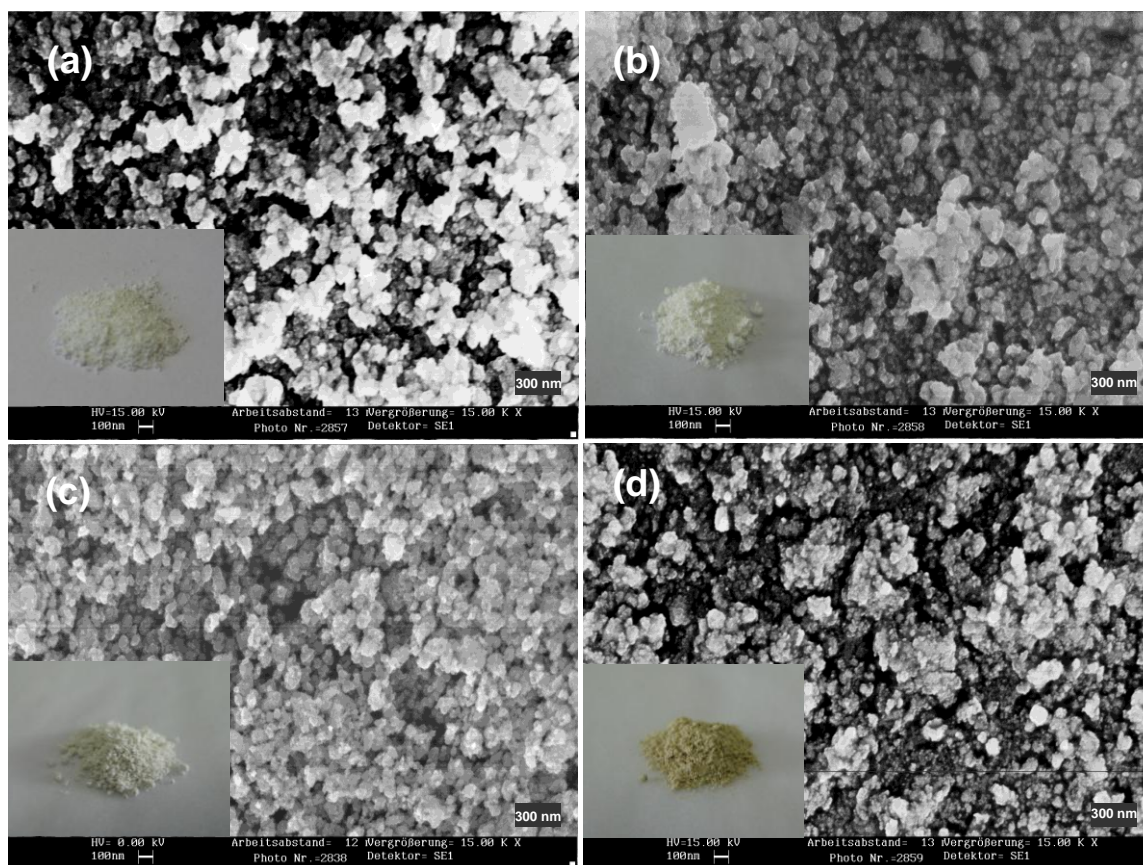


Figure 4.4: SEM images and appearance (inset) of (a) pristine TiO_2 , (b) $\text{Ar-1h-TiO}_{2-\delta}$, (c) $\text{H}_2\text{-1h-TiO}_{2-\delta}$ and (d) $\text{H}_2\text{-7h-TiO}_{2-\delta}$ nanoparticles.

4.3.2.2 Thermogravimetric Analysis

The changes of oxygen nonstoichiometry $\Delta\delta$ upon hydrogen reduction were determined by thermogravimetric analysis. The determined $\Delta\delta$ values are in the range of thousand ppm level showing around 5300 ppm for a $\text{H}_2\text{-7h-TiO}_{2-\delta}$ sample. In order to give a rough estimate for the equilibration time of anatase nanoparticles (particle size ~ 20 nm) for the reduction at 723 K, a series of preliminary TGA relaxation experiments were performed, yielding an oxygen chemical diffusion coefficient of approx. $\tilde{D}_o \approx 10^{-16} \text{ cm}^2\cdot\text{s}^{-1}$ (at 723 K) and a subsequent equilibration time of approx. 6 h. The calculated diffusion coefficient is shown in Table 4.2. In good agreement, DC conductivity relaxation (Figure 4.6b) shows a beginning saturation of the conductivity after ~ 350 min (close to 6 h), indicating that equilibration of the particles in reducing conditions is nearly

complete. The unrealistically small \tilde{D}_o value indicates the oxygen incorporation reaction to be surface-rate controlled for the 20 nm sized particles. Therefore, the 7 h-treated material ($H_{\mathcal{Z}} 7h\text{-TiO}_{2-\delta}$) very likely is fully reduced to the equilibrium conditions at 723 K and $P_{O_2} \approx 10^{-25}$ bar. The $H_{\mathcal{Z}} 7h\text{-TiO}_{2-\delta}$ is then only partially equilibrated but can nonetheless be assumed to be homogeneous owing to surface-rate controlled kinetics.

Table 4.2: Calculated oxygen stoichiometry values depending on hydrogen reduction time and oxygen chemical diffusivity.

Temperature [K]	$\tilde{D}_{O, fit}$ [$\text{cm}^2 \cdot \text{s}^{-1}$]	$\Delta\delta_{60\text{min}}$	$\Delta\delta_{180\text{min}}$	$\Delta\delta_{300\text{min}}$	$\Delta\delta_{420\text{min}}$
723	$1.7 \cdot 10^{-16}$	0.00235	0.00452	0.00499	0.00529

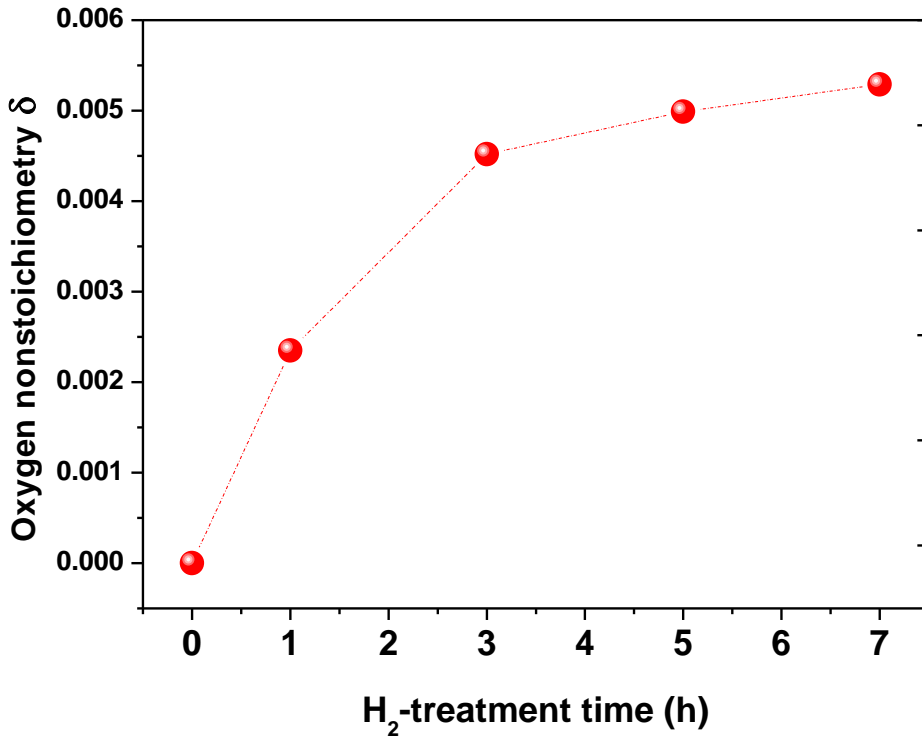


Figure 4.5: Oxygen stoichiometry upon hydrogen reduction as a function of treatment time (1 – 7 h)

4.3.2.3 Conductivity Study

Figure 4.6a shows the temperature dependence of the total conductivity of anatase TiO_2 before, during (1 h), and after the hydrogen thermal treatment at 723 K. The electronic conductivities in the temperature range of 473 – 723 K follows the Arrhenius form. The calculated activation enthalpies before and after H_2 -thermal reduction are almost identical as ≈ 1.5 eV. (Please see regime (i) and (iii) in Figure 4.16a.) The values are in good agreement with that reported by Weibel *et al.* for bulk anatase ($E_a \approx 1.3$ eV) in a similar temperature range[22]. Absence of significant change of activation enthalpies is indicative of the fact that the mechanism of conduction does not change upon thermal reduction and also that the nonstoichiometry remains frozen. After hydrogen thermal treatment for 1 h (H_2 -1h- TiO_{2-8}), the conductivity (at 723 K) increased by approx. one order of magnitude, showing $\approx 1.5 \cdot 10^{-3} \text{ S} \cdot \text{cm}^{-1}$, whereas more than two orders of magnitude higher conductivity was measured with H_2 -7h- TiO_{2-8} sample ($\approx 4.4 \cdot 10^{-2} \text{ S} \cdot \text{cm}^{-1}$).

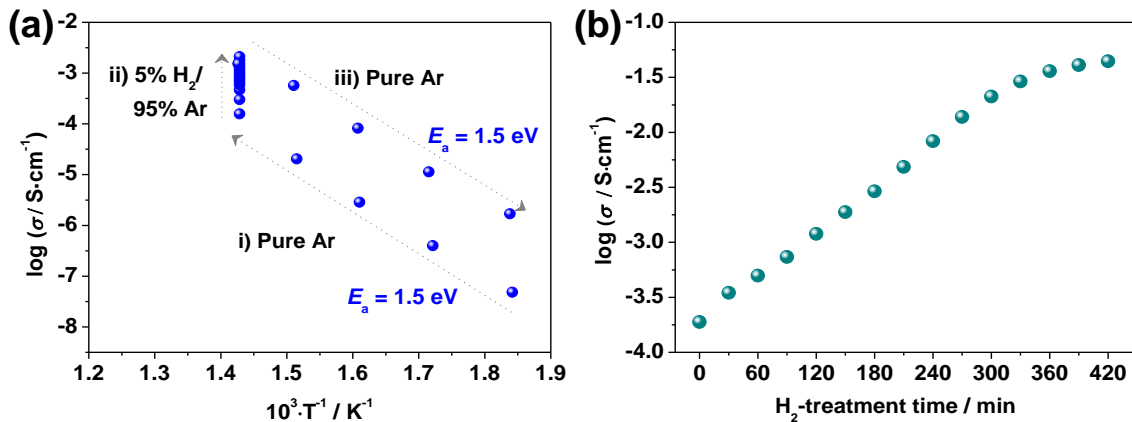


Figure 4.6. (a) *In-situ* monitoring of conductivity for TiO_2 before, during (1 h), and after H_2 -thermal treatment process. (b) Conductivity relaxation plot at 723 K under 5% H_2 / 95% Ar atmosphere.

4.3.2.4 Electrochemical Analysis: Li storage Performance

For analysis of electrochemical Li-storage properties, the prepared materials *i.e.* pristine TiO_2 , Ar-1h-TiO_{2-8} , and $\text{H}_2\text{-1h-TiO}_{2-8}$ were charged/discharged at 0.2C for 20 cycles and their galvanostatic discharge/charge curves are shown in Figure 4.7a. All the samples exhibit cathodic insertion of lithium at 1.75 V and anodic extraction of lithium at 1.95 V *vs.* Li/Li^+ that is a representative electrochemical characteristic of the titania electrode[30]. The Figure illustrates that both thermal-annealing and H_2 -thermal treatment are very effective to improve Li-storage performance, as $\text{H}_2\text{-1h-TiO}_{2-8}$ and Ar-1h-TiO_{2-8} show greatly enhanced discharge capacities of 180 mAh g^{-1} and 148 mAh g^{-1} , respectively, compared with pristine TiO_2 (64 mAh g^{-1}). It is clearly shown in Figure 4.7a that the total capacity enhancements by Ar-annealing and H_2 -reduction are mainly contributed by the increase of the two-phase plateau.

The charge/discharge capacities of the samples at various current densities (67.2 mA g^{-1} (0.2C) – 10.1 A g^{-1} (30C)) are shown in Figure 4.8. Despite the high initial capacities at 0.2C (234 mA g^{-1}), pristine TiO_2 exhibited a sharp capacity decay upon further twenty cycles. One hour of thermal treatment provided remarkably enhanced initial discharge capacities at the same C rate (0.2C), showing 350 mAh g^{-1} for Ar-1h-TiO_{2-8} electrode. However, excellent rate capabilities were obtained only for the $\text{H}_2\text{-1h-TiO}_{2-8}$ electrode, showing a discharge capacity of 60 mAh g^{-1} even very high C rate 10C. As the above observation reveals that the hydrogen-thermal treatment includes two different effects on the electrochemical lithium storage ability of the titania electrode, *viz.* i) thermal annealing, and ii) actual hydrogen treatment effect, it is necessary to differentiate between the two. Figure 4.7b clearly displays that at 0.2C 56 % of the capacity increase is contributed to the thermal annealing process, while 44 % is attributed to actual hydrogen reduction. The better lithium storage properties of thermally treated titania sample, *i.e.* Ar-1h-TiO_{2-8} compared with the pristine material can be explained by its more dense electrode morphology with better crystallinity particularly at particle surfaces. As shown in Figure 4.4a-d (SEM images), the particle morphology of titania electrodes tends to be more closely packed with an

increase of thermal annealing time (both under pure Ar and 5% H₂ / 95% Ar mixture). As a consequence, the denser particle interconnectivity induced can give rise to better electronic contacts between titania particles compared with those of non-annealed materials, which is definitely advantageous to obtain a better electrode performance[31]. Despite the enhanced electronic contacts for Ar-1h-TiO_{2-δ} sample, electronic conductivity seems to be still limited to the bulk value of anatase. Here the effect of H₂-reduction comes into play. Compared to the Ar-annealing, H₂-thermal treatment effectively increases the bulk value of electronic conductivity by means of frozen-in defects that facilitate the electron transport. This most likely gives rise to the significant increase in voltage plateau not only at low C rates but also under high current densities.

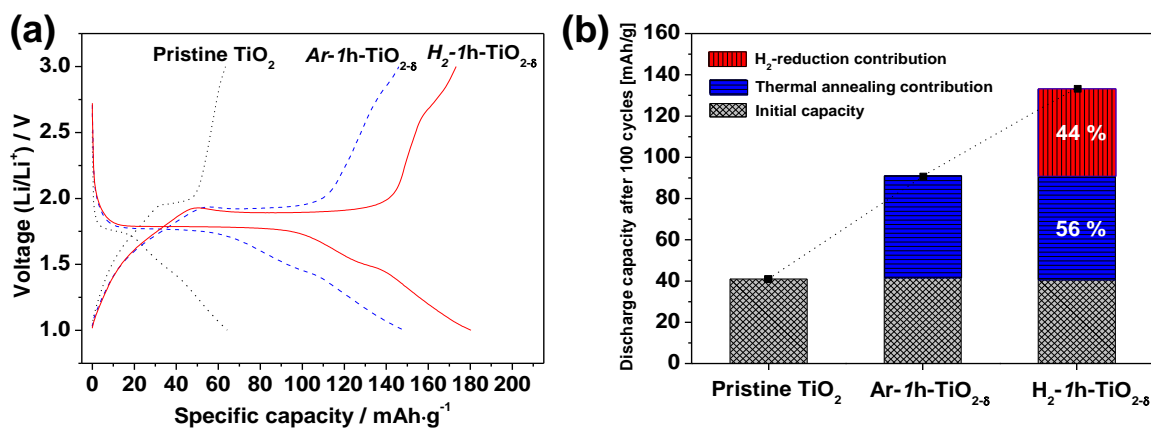


Figure 4.7: (a) Galvanostatic charge/discharge profiles (at 20th cycle) and (b) discharge capacities for pristine TiO₂ (dotted line), Ar-1h-TiO_{2-δ} (dashed line), and H₂-1h-TiO_{2-δ} (solid line) cycled at 0.2C.

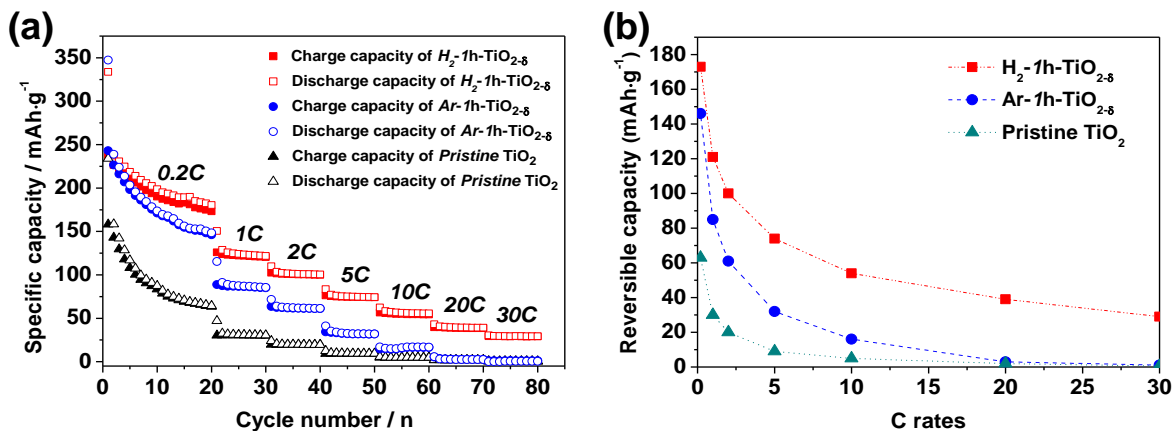


Figure 4.8: Comparison of the rate performance of pristine TiO₂, Ar-1h-TiO_{2-δ}, and H₂-1h-TiO_{2-δ}.

Now let me discuss effects of reduction time which is directly related to electronic charge carriers concentration on electrochemical Li storage performance of titania electrodes. For this, first Li-storage performances of H_2 - n h-TiO_{2- δ} nanoparticles are compared in Figures 4.9–10 and Table 4.3. The electrodes were charged/discharged for 100 cycles at constant current densities of 1C (0.336 A \cdot g⁻¹) and 10C (3.360 A \cdot g⁻¹), respectively. It is clearly seen that oxygen-deficient H_2 - n h-TiO_{2- δ} electrodes delivered higher capacities than those for the pristine (stoichiometric) TiO₂ electrode. On the other hand, it is interesting to note that despite the lower electronic conductivity (lower concentration of frozen-in defects), the reversible capacity of the H_2 -1h-TiO_{2- δ} at 1C (161 mAh \cdot g⁻¹) was considerably higher than that of H_2 -7h-TiO_{2- δ} (99 mAh \cdot g⁻¹). At 10C, the H_2 -1h-TiO_{2- δ} sample delivered nearly the same reversible capacity (159 mAh \cdot g⁻¹, 20th cycle) with that delivered at 1C without no significant capacity decay. In contrast, the H_2 -7h-TiO_{2- δ} electrode lost 19 % of its discharge capacity. This is summarized in Figure 4.10a. The Figure shows that with increasing C rates from 0.2C to 10C, only a slight decay of discharge capacity (12 %) occurs for H_2 -1h-TiO_{2- δ} . On the other hand, Figure 4.10b shows reversible capacities (at 1C/10C) as a function of the degree of reduction. It is noteworthy here that the capacity does not proportionally increase with reduction time, but show a maximum values at 1 h treatment condition. Details on this phenomenon are discussed in the next section (Chapter 4.3.2.6).

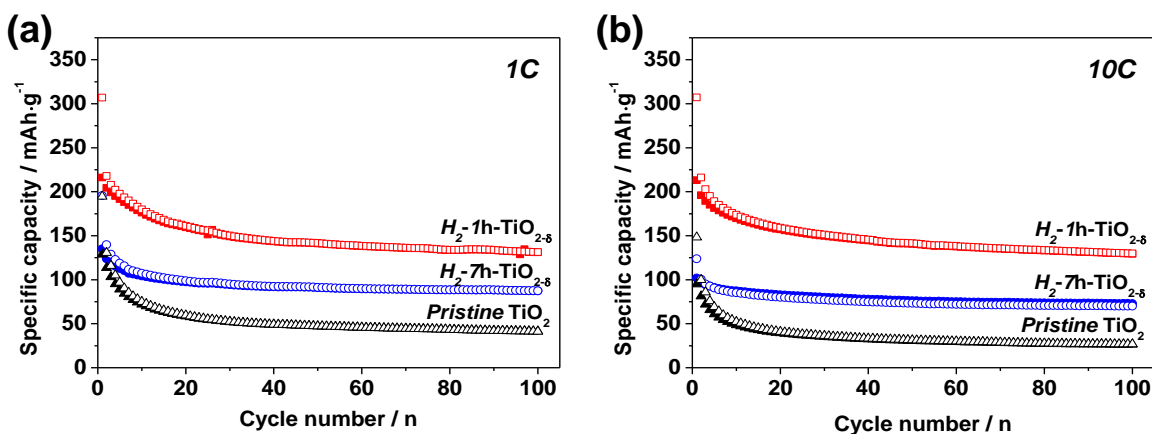


Figure 4.9: Variation of charge and discharge capacity versus cycle number for H_2 -1h-TiO_{2- δ} (discharge \square , charge \blacksquare), H_2 -7h-TiO_{2- δ} (discharge \circ , charge \bullet), and pristine TiO₂ (discharge \triangle , charge \blacktriangle) cycled at constant current rate of (a) 1C (336 mA \cdot g⁻¹) and (b) 10C (3.36 A \cdot g⁻¹).

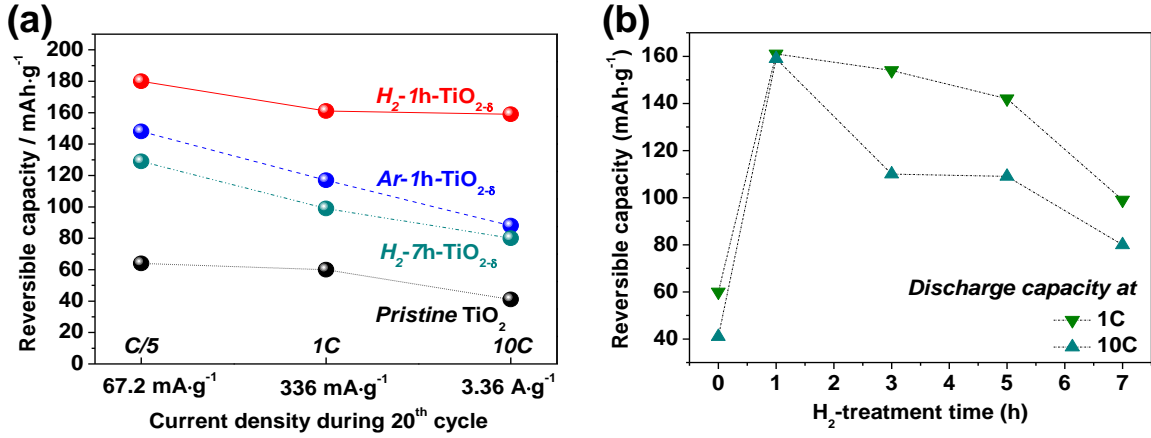


Figure 4.10: (a) Current density dependence of the reversible discharge capacity for differently-treated anatase TiO₂ nanoparticles. (b) Reversible capacities of hydrogen reduced titania electrodes during discharge at 1C and 10C as a function of hydrogen treatment time.

Table 4.3: First and reversible capacities during discharge at 1C and 10C.

	1C [mAh·g ⁻¹]		10C [mAh·g ⁻¹]	
	(1 st cycle)	(20 th cycle)	(1 st cycle)	(20 th cycle)
Pristine TiO ₂	195	41	148	27
Ar-1h-TiO _{2-δ}	267	91	192	65
Ar-7h-TiO _{2-δ}	245	80	146	57
H ₂ -1h-TiO _{2-δ}	307	131	307	130
H ₂ -3h-TiO _{2-δ}	222	140	163	100
H ₂ -5h-TiO _{2-δ}	222	132	114	99
H ₂ -7h-TiO _{2-δ}	196	88	124	70

4.3.2.5 Electrochemical Analysis: Kinetic Analysis

This section focuses on the kinetic analysis of thermally reduced samples ($H_x nh$ -TiO_{2-δ}). Let me discuss the behavior of the different hydrogen thermally treated titania nanoparticles using EIS and SSCV measurements[32-34]. Nyquist plots for the $H_x nh$ -TiO_{2-δ} show a single semicircle at high frequency range which corresponded to the charge transfer resistance of Li⁺ from the electrolyte into the electrode material, followed by a steep sloping line at lower frequencies (Warburg impedance) where the electrode kinetics is completely limited by chemical diffusion process of Li under semi-infinite conditions (see Figure 4.11a inset). The Warburg factor (S_W) can be determined especially by plotting in the complex plane $-Z''$ (imaginary) = $S_W \omega^{-1/2}$ or Z' (real) = $S_W \omega^{-1/2}$ against $\omega^{-1/2}$ where ω is angular

frequency (Figure 4.11a). In Figure 4.11b, the calculated S_W values are plotted as a function of treatment time. Herefrom the effective chemical diffusion coefficient of Li (D_{Li}^δ) can be calculated using the following equation[35]

$$\tilde{D}_{Li} = \frac{R^2 T^2}{2A^2 n^{*4} F^4 C^{*2} S_W^2} \quad (4.3-2)$$

with R ; molar gas constant, T ; absolute temperature, A ; electrode surface area in cm^2 , n^* ; number of electrons transferred, F ; Faraday constant, and C^* is the bulk concentration of the species in mol cm^{-3} . (The calculated D_{Li}^δ values are summarized for the various hydrogen thermal treatment times (0, 1, 3, 5, 7 h) in Table 4.4 and plotted in Figure 4.11b.) The effective D_{Li}^δ in a stoichiometric TiO_2 electrode was determined as $\approx 1.7 \cdot 10^{-17} \text{ cm}^2 \cdot \text{s}^{-1}$. Compared with this pristine titania sample, a significant increase in D_{Li}^δ was observed only by one hour of hydrogen thermal treatment ($\approx 1.3 \cdot 10^{-16} \text{ cm}^2 \cdot \text{s}^{-1}$). Upon extended treatments, D_{Li}^δ show a maximum for H_2 3h- $\text{TiO}_{2-\delta}$ sample, and the value for H_2 7h- $\text{TiO}_{2-\delta}$ decreased to $\approx 6.8 \cdot 10^{-17} \text{ cm}^2 \cdot \text{s}^{-1}$.

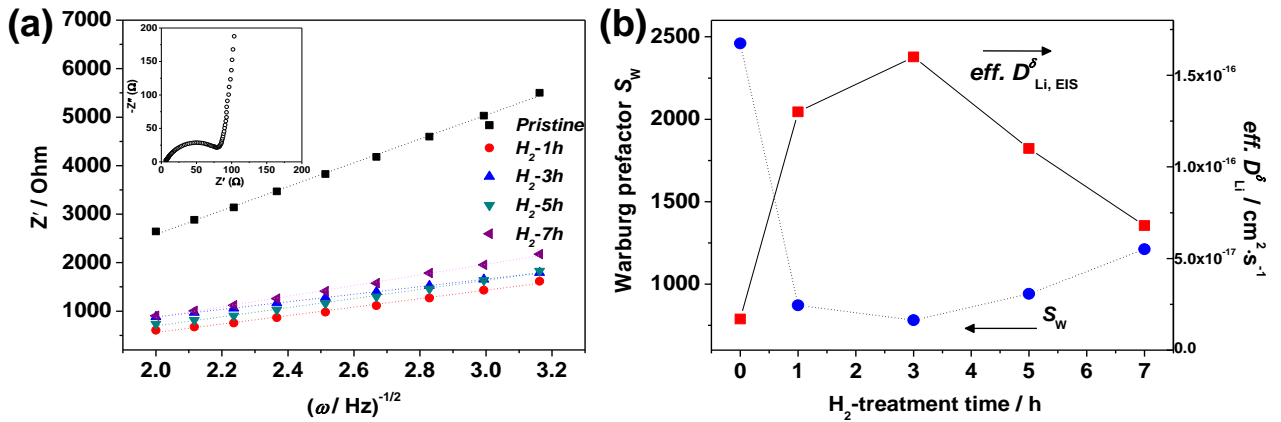


Figure 4.11: (a) Z' vs. $\omega^{-1/2}$ at low frequency region for H_2 -treated $\text{TiO}_{2-\delta}$ electrodes depending on the H_2 -treatment time (inset: Nyquist plot of H_2 -1h- TiO_2 sample). (b) Warburg prefactor (S_W) with effective chemical diffusion coefficient of Li in pristine TiO_2 and hydrogen treated $\text{TiO}_{2-\delta}$ nanoparticles as a function of hydrogen treatment time.

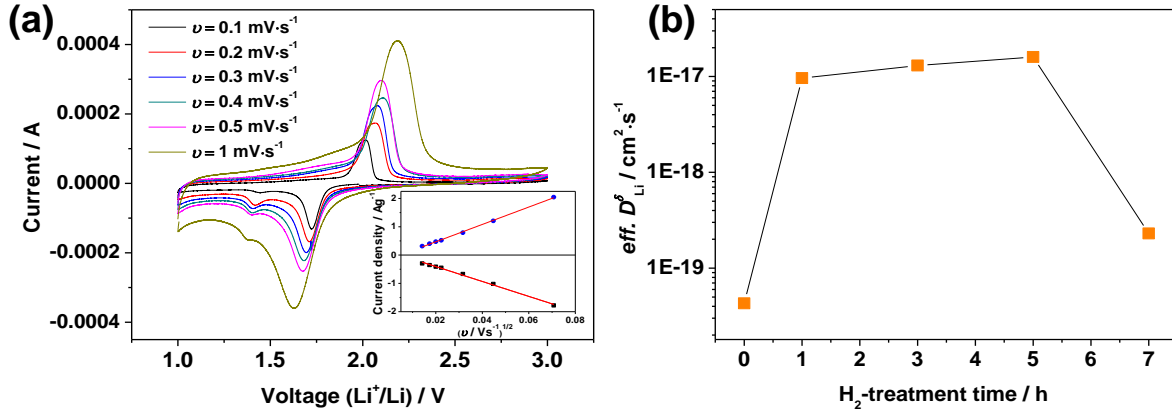
The diffusion coefficients were estimated also from the peak current in the SSCV measurements[35-37]. Figure 4.12a shows cyclic voltammograms of $H_{27}Ih\text{-TiO}_{2-\delta}$ electrode measured at different scan rates (0.1 – 1 $\text{mV}\cdot\text{s}^{-1}$). The material depicts a pair of redox peaks at the voltage ≈ 1.75 V (Li insertion) and ≈ 1.95 V (Li-extraction), confirming the Li-insertion/extraction reaction revealed by galvanostatic charge/discharge curves (Figure 4.7a). As the measured peak current i_p for a diffusion-controlled system is proportional to the square root of the scan rate (Figure 4.12a inset), the peak current i_p can be described by the Randles-Sevcik equation for the diffusion-controlled reversible system at room temperature[35]

$$i_p = (2.69 \cdot 10^5)n^{*3/2}AD^{1/2}C^*v^{1/2} \quad (4.3-3)$$

with n^* ; number of electrons transferred, A ; electrode surface area in cm^2 , D ; chemical diffusion coefficient of the species (here Li) in $\text{cm}^2\cdot\text{s}^{-1}$, v ; scan rate in $\text{V}\cdot\text{s}^{-1}$ and C^* is the bulk concentration of the species in the accumulation layer in $\text{mol}\cdot\text{cm}^{-3}$. The n is taken as unity and C^* is taken as 0.024 $\text{mol}\cdot\text{cm}^{-3}$ for $x = 0.5$ according to the following lithium intercalation reaction, $\text{TiO}_2 + x\text{Li}^+ + xe^- = \text{Li}_x\text{TiO}_2$ [38]. (Please note that a linear proportionality is expected for capacitive currents.) Obviously even though a two phase mechanism is referred to, diffusion describes the kinetics well. This presupposes that the motion of the interfaces is not rate-determining and the diffusion situation is operationally semi-infinite. The calculated effective diffusion coefficient for the pristine titania electrode ($\approx 4.3 \cdot 10^{-20}$ $\text{cm}^2\cdot\text{s}^{-1}$) lies in the similar range with the recently reported value determined by SSCV method[39]. By one hour thermal reduction, the effective D_{Li}^δ also notably increased to $\approx 9.6 \cdot 10^{-18}$ $\text{cm}^2\cdot\text{s}^{-1}$.

Table 4.4. Determined chemical diffusion coefficient of Li, D_{Li}^{δ} depending on the H_2 -thermal treatment time using EIS and SSCV.

	H_2 -exposure time [h]	D_{Li}^{δ} (EIS) [$cm^2 \cdot s^{-1}$]	D_{Li}^{δ} (SSCV) [$cm^2 \cdot s^{-1}$]
Pristine TiO_2	0	$1.7 \cdot 10^{-17}$	$4.3 \cdot 10^{-20}$
H_2 -1h- $TiO_{2-\delta}$	1	$1.3 \cdot 10^{-16}$	$9.6 \cdot 10^{-18}$
H_2 -3h- $TiO_{2-\delta}$	3	$1.6 \cdot 10^{-16}$	$1.3 \cdot 10^{-17}$
H_2 -5h- $TiO_{2-\delta}$	5	$1.1 \cdot 10^{-16}$	$1.6 \cdot 10^{-17}$
H_2 -7h- $TiO_{2-\delta}$	7	$6.8 \cdot 10^{-17}$	$2.3 \cdot 10^{-19}$

**Figure 4.12:** (a) Cyclic voltammograms of H_2 -1h- $TiO_{2-\delta}$ electrodes at different scan rates (0.1 ~ 1 $mV \cdot s^{-1}$) and corresponding voltametric current densities versus square root of scan rate (inset). (b) The effective chemical diffusion coefficient of Li calculated using SSCV depending on the hydrogen treatment time.

It must be stated that the variation of the diffusion coefficient with δ comes out similar in both methods. The fact that absolute values are found smaller in the SSCV than in the EIS is a common observation and is probably due to the very different amplitudes used[39-42]. In case of EIS these amplitudes are much smaller (10 mV) avoiding concentration variations that could locally drive the phase out of saturation range. At any rate, as far as various techniques are concerned, the variations of effective D_{Li}^{δ} as a function of treatment time determined by these methods are in reasonable agreement (showing a maximum).

4.3.2.6 Discussion: Defect model

In this section, the experimentally observed feature (the increase of storage capacity and lithium diffusivity from non-treated TiO_2 to $H_x/T_h\text{-TiO}_{2-\delta}$ and then a decrease upon extended reduction) is elucidated using defect chemistry. Assuming that all the individual TiO_2 particles are well connected (*i.e.* fast transport of electrons *via* the current collector and fast transport of the ions through the electrolyte to every particle), and excluding the case that the conductivities of electrons and ions in TiO_2 are very similar the decisive quantity is the effective diffusion of lithium in titania that governs the storage kinetics. For this I mainly consider the relevant charge carrier concentrations and conductivities.

The mobile Li^+ conductivity is determined by two factors: (a) mobility, and (b) concentration of Li^+ ions. Because the sufficiently small values of determined δ (thousand ppm level, Figure 4.5) most likely exclude dominance of potentially formed Magnéli-type phases[28], a great significance of hydrogen reduction is then the effect on the concentration of Li^+ charge carriers rather than on the mobility. As far as charge carriers are concerned, there are several theoretical studies in literature suggesting that Li^+ ion and electron transport in anatase are highly correlated or strongly coupled[43-45]. Very little experiments however have been carried out in probing Li^+ ion and electron transport in anatase, and Kerisit *et al.* rightly state that “this potential ambipolar diffusion aspect of Li insertion has largely been deemphasized in previous experimental work”[44]. Li^+ ion transport was probed using nuclear magnetic resonance (NMR) methods, yielding Li^+ ion self-diffusivities around $10^{-12} \text{ cm}^2\cdot\text{s}^{-1}$ at room temperature[46-47]. This self-diffusivity however is probed on an atomic length scale, and the method cannot elucidate whether there is long range transport or just Li jumps around a polaron site, with no net displacement.

In the present thesis, a more simple approach has been used for the model. Even though there is an indication for coupled transport of polarons and Li^+ ions in anatase, also the free polaron, *i.e.* the polaron not bound to a next-neighbor Li^+ ion, and similarly the free Li^+ ion should be able to migrate separately. In this case, a simple thermodynamic equilibrium approach can be used to determine the

concentration of the free, un-trapped Li^+ ion and small polaron. As already mentioned, Li interstitials (Li_i^\bullet) are associated with excess electrons e' ($\equiv \text{Ti}'_{\text{Ti}} - \text{Ti}_i^{\text{X}}$) to form neutral associates ($\text{Li}_i^\bullet + e' \rightleftharpoons \text{Li}_i^{\text{X}}$), and therefore it can lead to a drastic depletion of free Li^+ carriers. Due to mass action, the association degree is the larger the greater the degree of reduction. A defect model for $\text{Li}_x\text{TiO}_{2-\delta}$ which takes into account this associate formation and concentrates on *e.g.* doubly ionized oxygen vacancies is as follows. First I have to consider the following four major reactions and balances

(i) associate (assoc.) formation, with binding enthalpy E_{bind} :



$$K_{\text{assoc.}} = \frac{[\text{Li}_i^{\text{X}}]}{[\text{Li}_i^\bullet][e']}, \text{ with } K_{\text{assoc.}} = \exp\left(-\frac{E_{\text{bind}}}{kT}\right) \quad (4.3-5)$$

(ii) Lithium insertion balance

$$[\text{Li}_i^\bullet] + [\text{Li}_i^{\text{X}}] = x \quad (4.3-6)$$

(iii) Charge neutrality balance

$$[e'] = [\text{Li}_i^\bullet] + 2[V_o^{\bullet\bullet}] \quad (4.3-7)$$

(iv) Oxygen non-stoichiometry δ .

$$[V_o^{\bullet\bullet}] = \delta \quad (4.3-8)$$

Then concentrations of all species can be calculated as a function of the input parameters $K_{\text{assoc.}}(T)$'s, x and δ where $K_{\text{assoc.}}$ denotes mass action constant. As a consequence, solving Eq (4.3-5), (4.3-6), and (4.3-7) for the free Li concentration $[\text{Li}_i^\bullet]$ yields

$$[\text{Li}_i^\bullet] = \frac{-2K_{\text{assoc.}}\delta - 1 + \sqrt{4K_{\text{assoc.}}^2\delta^2 + 4K_{\text{assoc.}}(\delta + x) + 1}}{2K_{\text{assoc.}}} \quad (4.3-9)$$

As $[e'] = [\text{Li}_i^\bullet] + 2\delta$, the n -type carrier concentration $[e']$ is finally given as follows

$$[e'] = \frac{2K_{\text{assoc.}}\delta - 1 + \sqrt{4K_{\text{assoc.}}^2\delta^2 + 4K_{\text{assoc.}}(\delta + x) + 1}}{2K_{\text{assoc.}}} \quad (4.3-10)$$

Figure 4.13a shows the modeled result of the molar fraction of free electrons for various formation enthalpies of associates. At association enthalpies around 0.1 eV, the amount of free n -type carriers is expected to already decrease by almost one order of magnitude, if the Li content is increased. With association enthalpies of 0.5 eV (as already proposed by Olson *et al.*[48]), almost all electrons introduced by Li intercalation are effectively trapped in Li_i^X associates, while the n -type carrier concentration remains approximately at the level given by the reduction (*i.e.* 2δ) throughout the Li concentration range. The defect diagram in Figure 4.14a shows the anticipated situation. At low δ the electronic concentration is compensated by ionized defects, while for high δ the compensating role is taken over by oxygen vacancies. From this phenomenon, $[Li_i^\bullet]$ is expected to decrease. For more detailed descriptions of Brouwer diagrams, please see the next theoretical analysis section (Chapter 4.4).

The free Li concentration as a function of the nonstoichiometry δ can be also directly derived from the model (Figure 4.13b). At associate formation enthalpies that are large compared to the thermal energy (0.02 eV at room temperature), only a very small amount of Li^+ ions is not bound in an associate and can move freely. I have taken this free Li^+ ion concentration from the defect model to estimate the Li^+ conductivity ($\sigma_{Li_i^\bullet}$) in anatase at the fixed Li content of $x = 0.25$. On the other hand, the electronic conductivity σ_e was determined by extrapolating the 723 K value down to room temperature. Therefore, absolute conductivity values should be treated with care while tendencies should be accurately reflected. Combining those two component conductivities *i.e.* $\sigma_{Li_i^\bullet}$ and σ_e , I can get an insight into the ambipolar conductivity of Li (σ_{Li}^δ). (Please note that in order to fix the starting value for $\sigma_{Li_i^\bullet}$, the conductivity ratio $\sigma_{Li_i^\bullet} / \sigma_e$ which was determined by Sushko *et al.*[43] by multiscale modeling for stoichiometric TiO_2 was applied). In Figure 4.13b, one can easily recognize at a first glance that ambipolar conductivity of Li runs through a maximum at 1 ~ 2 h of H_2 -reduction condition that is a comparable behavior with the storage experiment.

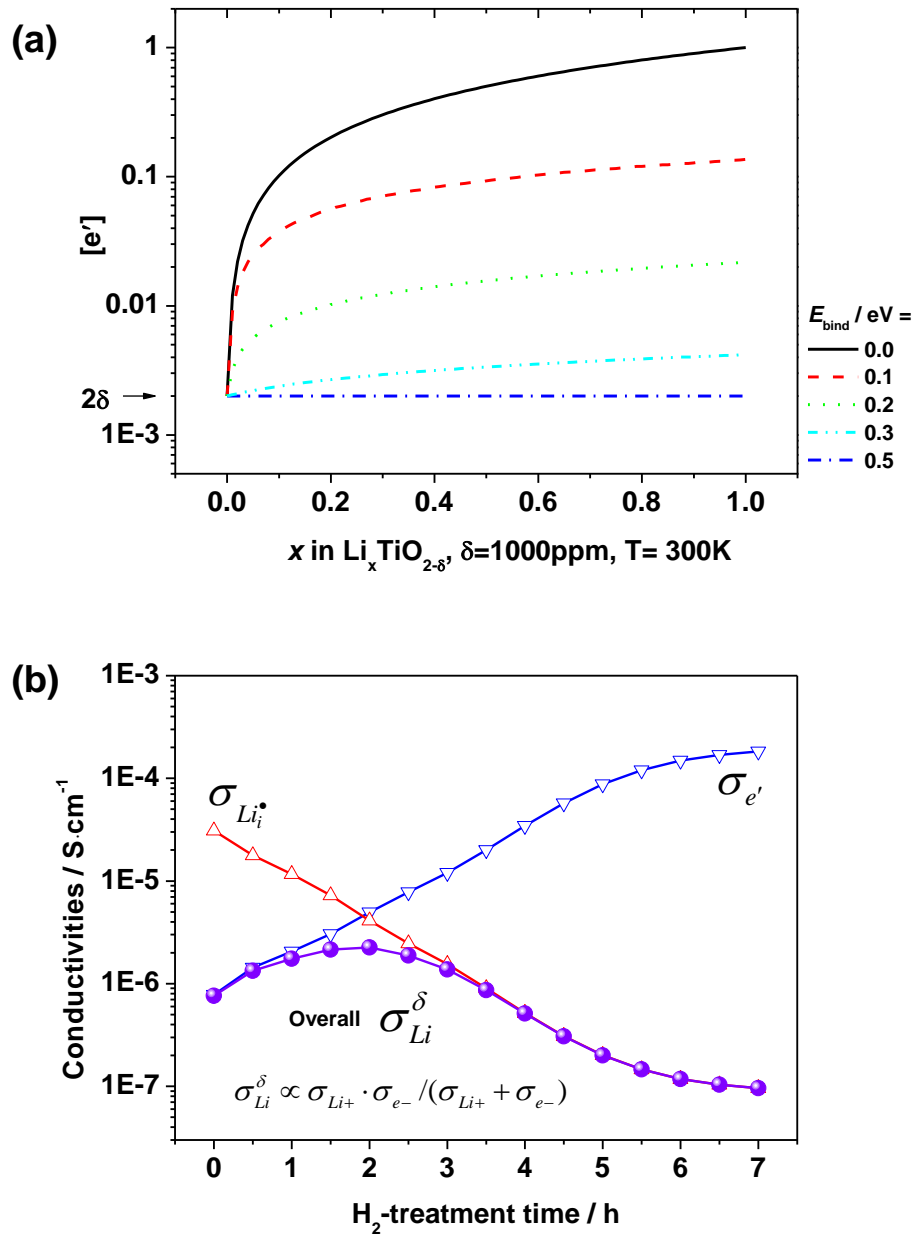


Figure 4.13: (a) Molar fractions of free n -type charge carriers e' , as a function of the formation enthalpy for associates, as given by the defect model. The arrow at $2 \cdot 10^{-3}$ denotes the amount of n -type carriers introduced by the hydrogen-thermal annealing process. (b) Calculated partial conductivity contributions towards, and overall ambipolar conductivity of Li as derived from the defect model for $\text{Li}_x\text{TiO}_{2-\delta}$ at fixed Li content $x = 0.25$.

Based on the defect diagram shown in Figure 4.14a, I can also anticipate the variation of lithium diffusivity. The chemical diffusion coefficient of Li consists of an inverse chemical resistance ($\propto \sigma_{Li}^\delta \propto \sigma_{e'} \cdot \sigma_{Li^*} / \sigma$) and an inverse chemical capacitance ($\propto \partial \mu_{Li} / \partial c_{Li}$). If the Li content is essentially realized through Li_i^X , the second term, for ideal conditions, is given by $(\partial \ln[Li_i^X]) / (\partial [Li_i^X]) \cdot RT = (RT) / ([Li_i^X])$ and hence constant at given Li content. (Please note that differential trapping factors have to be explicitly invoked for more general cases (see Chapter 4.4)[19,49]. Because the development of D_{Li}^δ is given by the development of σ_{Li}^δ , then D_{Li}^δ also must run through a maximum as a function of degree of reduction (oxygen nonstoichiometry δ) (Figure 4.14b). But this is possible only if the association initial condition is very strong and mobility of the lithium ions (u_{Li^*}) is greater than that of the electrons ($u_{e'}$), as suggested by Sushko *et al.*[43]. If the mobility of electrons is larger than that of lithium ions ($u_{e'} \gg u_{Li^*}$), the maximum should be attributed to the interplay of percolation and local storage kinetics, because in this case a monotonic decrease of D_{Li}^δ as a function of δ is expected. (Details are discussed in the next section.)

Here the electron's double role in the storage of a multi particle arrangement needs to be addressed. The first role is that it – together with Li^+ motion – enables Li transport within a particle. Second, it is important for bringing the electrons to the active particle which is in contrast with the electrolyte. For example, as shown in Figure 4.15, while the TiO_2 -particle #1 is readily accessible to storage (quick transport of Li^+ through the electrolyte, and of e^- through the current collector), this is not the case for particle #2 if the electronic conductivity of particle #1 is poor. In every experiment performed here, these factors will appear together with the local D_{Li}^δ and hence be incorporated in the effectively measured value. Hence the counterplay of increased $\sigma_{e'}$ and decreased σ_{Li^*} can qualitatively explain the results even for $u_{Li^*} \ll u_{e'}$. A more detailed description of the defect chemistry is given in the next theoretical analysis section.

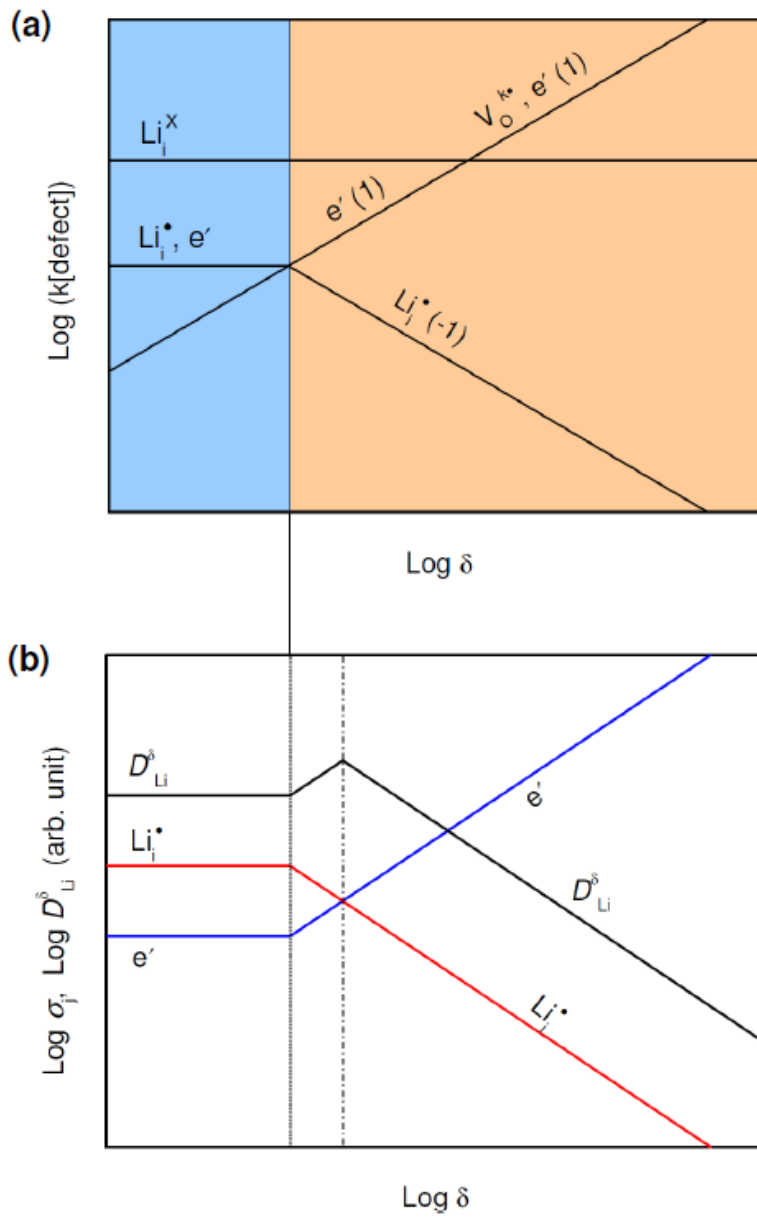


Figure 4.14: Dependence of (a) defect concentrations, (b) conductivities, and chemical diffusion coefficient of Li in $\text{Li}_x\text{TiO}_{2-\delta}$, on oxygen nonstoichiometry δ . (Please note that the assumption for (b) is that Li_i^\bullet mobility exceeds e' mobility.)

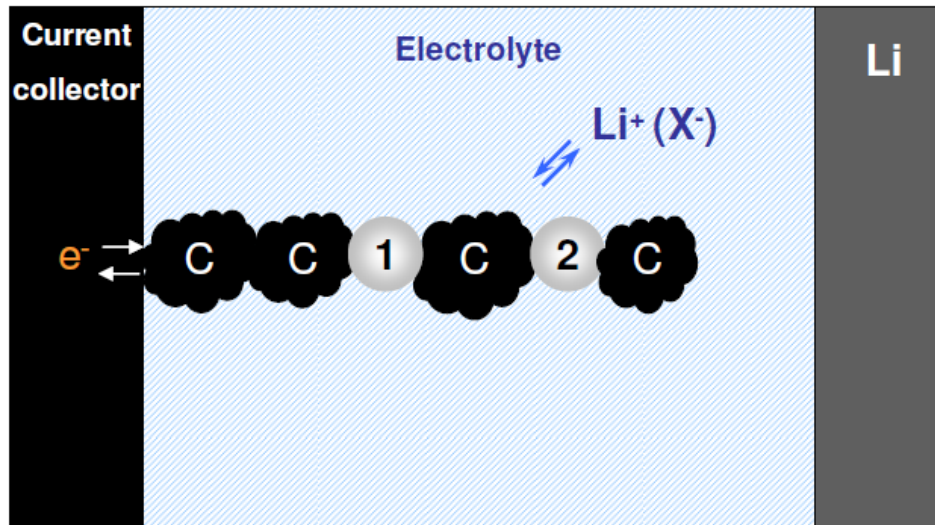


Figure 4.15: Schematic representation of the effect of electronic charge carrier concentration in electrochemically active materials on overall Li storage performance.

As a summary, Figure 4.16 shows the overall correlation among $\sigma_{e'}$, σ_{Li}^{δ} , D_{Li}^{δ} , and Li-storage performance as a function of hydrogen reduction time which is related to the electronic conductivity.

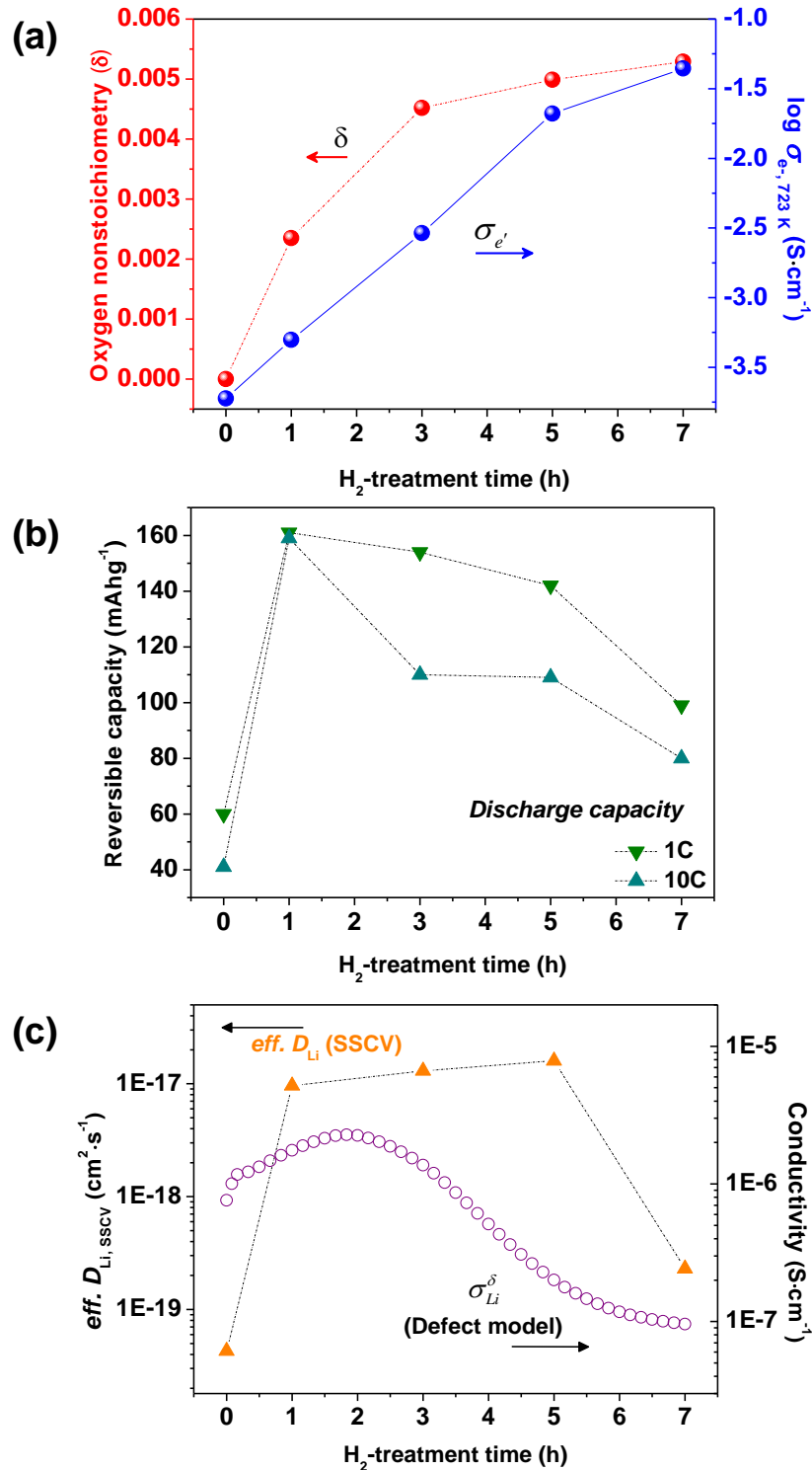


Figure 4.16: Summary of determined electrical and electrochemical parameters as a function of hydrogen reduction time.

4.4 Theoretical Analysis– Brouwer Diagrams

Here in this section the experimental observation described in the previous section is extended to investigation of the more detailed defect chemistry. For this purpose, mass action laws and balance equations are discussed for oxygen nonstoichiometric lithium titanate ($\text{Li}_x\text{TiO}_{2-\delta}$). Defect concentrations and lithium diffusivity in lithiated oxygen-deficient lithium titanate ($\text{Li}_x\text{TiO}_{2-\delta}$), where the oxygen nonstoichiometry is frozen-in, are analytically derived. This treatment is simplified compared to the previous study on LiFePO_4 [19] because titanium defects are neglected for the parameter window considered. On the other hand, oxygen vacancies are included in the analysis. It represents a particularly relevant example for two reasons. First of all, the complete composition window $\text{Li}_x\text{TiO}_{2-\delta}$ can be experimentally exploited by varying oxygen and lithium activities. Second, as the temperatures at which reversibility for the different sublattices can be attained in reasonable times are very different, one meets here a excellent example of partially frozen-in defect chemistry and of the significance of *in-situ* and *ex-situ* parameters[25]. While at room temperature the lithium content can be reversibly varied (the lithium activity a_{Li} is an *in-situ* parameter), the variation of the oxygen content demands an intermediate annealing at high temperature (P_{O_2} as *ex-situ* parameter).

4.4.1 Study on Defect Concentration

While at high temperatures, the reversibility with the oxygen partial pressure gives rise to a power law ($P_{\text{O}_2}^{N_j}$) as far as the concentration of the charge carrier (point defect) j is concerned, at room temperature, the oxygen content is frozen which gives rise to a native doping effect. Here then the influence occurs through the electroneutrality condition and the effective dopant concentration C to which the oxygen defects contribute. Because TiO_2 is n -type conducting in the window of consideration and cannot tolerate oxygen interstitials, the electroneutrality therefore is expressed as $[e'] = C + [\text{Li}'_i]$. This relation anticipates that lithium

occupies interstitial sites[50-51] according to $Li + V_i \rightleftharpoons Li_i^\bullet + e'$ (this is also crystallographically meaningful). Because the electrostatic and elastic interactions between point defects can lead to clustering (or so-called association), at room temperature ion-electron association between Li^+ ions and electrons but also between oxygen vacancies and electrons have to be considered according to $Li_i^\bullet + e' \rightleftharpoons Li_i^X$ and $V_o^{\bullet\bullet} + 2e' \rightleftharpoons V_o^\bullet + e' \rightleftharpoons V_o^X$. As illustrated in the previous section, in particular the first reaction seems to take place to a very great degree (*i.e.* with a large enthalpy of association[48]). In general, for Boltzmann and Brouwer-condition, one expects for any carrier j (K_r denoting the mass action constant of the reaction r) as a function of C , a_{Li} (lithium activity being a measure of cell voltage *vs.* Li) and T (temperature)

$$[j] \propto C^{M_j} a_{Li}^{N_j} \prod_r K_r^{\gamma_{rj}}(T) \quad (4.4-1)$$

giving rise to Brouwer and Van't Hoff diagrams[52-53]. Under the same conditions, power laws of the form are expected for

$$[j] \propto \delta^{M'_j} x^{N'_j} \prod_r K_r^{\gamma'_{rj}}(T) \quad (4.4-2)$$

with varied exponents in the case of the parameter set δ , x and T (compared with the parameter set C , a_{Li} and T) where δ is the oxygen deficiency ($\delta = [V_o^{\bullet\bullet}] + [V_o^\bullet] + [V_o^X]$) in $TiO_{2-\delta}$ and at x the lithium content ($x = [Li_i^\bullet] + [Li_i^X]$). Here the exponents (M'_j , N'_j , and γ') can be easily found using the following mass action laws and balance equations.

$$\delta = [V_o^{\bullet\bullet}] + [V_o^\bullet] + [V_o^X] \quad (\text{oxygen stoichiometry}) \quad (4.4-3)$$

$$x = [Li_i^\bullet] + [Li_i^X] \quad (\text{Li stoichiometry}) \quad (4.4-4)$$

$$2[V_o^{\bullet\bullet}] + [V_o^\bullet] + [Li_i^\bullet] = [e'] \quad (\text{electroneutrality}) \quad (4.4-5)$$

$$[V_o^{\bullet\bullet}][e'] = K_1[V_o^\bullet] \quad (\text{trapping of } e' \text{ by } V_o^{\bullet\bullet}) \quad (4.4-6)$$

$$[V_o^\bullet][e'] = K_2[V_o^X] \quad (\text{trapping of } e' \text{ by } V_o^\bullet) \quad (4.4-7)$$

$$a_{Li} = K_3[Li_i^X] \quad (\text{neutral incorporation of Li}) \quad (4.4-8)$$

$$[Li_i^\bullet][e'] = K_4[Li_i^X] \quad (\text{trapping of } e' \text{ by } Li_i^\bullet) \quad (4.4-9)$$

As long as in a given defect chemical regime only one oxygen defect or lithium defect dominates the respective mass balance, in the logarithmic form the mass action laws are linear. In addition to this, Brouwer conditions require the logarithmic electroneutrality equation to be linear[52]. This is guaranteed if two oppositely charged point defects dominate. The considerations can be extended in a straightforward way to the presence of titanium defects.

Figures 4.17–4.21 show Brouwer diagrams $\log [\text{defect}]$ vs. $\log x$ or $\log a_{Li}$ (at constant δ) or vs. $\log \delta$ (at constant x , or a_{Li}) derived from the above mass action laws and balance equations. Please note that for simplicity, the contribution $\log 2$ arising from the double charge of $V_o^{\bullet\bullet}$ is suppressed in all Figures (see Eq (4.4-5)). This does not affect the slopes, only the transition regimes are to be slightly modified.

At a first glance the diagrams look quite different according to the choice of the “initial” situation (left hand side values of the abscissa) specified by the trap-state at low a_{Li} . As far as the plot $\log [\text{defect}]$ vs $\log x$ or $\log a_{Li}$ is considered, first the evolution of the defect diagram depends on whether $V_o^{\bullet\bullet}$, V_o^\bullet (or V_o^X) predominates at zero x (or a_{Li}). This is clear when one compares Figure 4.17a with 4.17b. When comparing $[V_o^{\bullet\bullet}]$ with $[V_o^\bullet]$, it is appropriate to consider Eq (4.4-7) showing that $[V_o^{\bullet\bullet}]/[V_o^\bullet] = K_1/[e']$. If $[e']$ tends to zero, $[V_o^{\bullet\bullet}]$ is expected to dominate initially.

When lithium defects are considered, it must be noticed that an exergonic trapping reaction, *e.g.* $Li_i^\bullet + e' \rightleftharpoons Li_i^X$ (the same holds for oxygen vacancies) does not imply that at room temperature always the trapped state is dominant. For small concentrations, the configurational entropy influence can be very strong. According to Eq (4.4-9) showing $[Li_i^\bullet]/[Li_i^X] = K_4/[e']$, $[Li_i^\bullet]$ would, if $[e']$ tends to zero, dominate over $[Li_i^X]$ for even very small K_4 values. The comparison of Figure 4.17a with 4.17c *e.g.* shows that an additional regime (green regime) occurs depending on the ratio of $[Li_i^\bullet]/[Li_i^X]$ one starts with at the left hand side. The important information however does not depend very much on such details. Increase of lithium content (x) gives rise to an increase of Li^+ and e^- carriers, *i.e.* Li_i^\bullet and e' even though not as

step as for Li_i^x which eventually will dominate x . On increased x also the tendency is obvious to realize δ eventually by V_o^x . Still considering lithium defects, the transition from x to a_{Li} as variable is only important if x is initially given by Li_i^\bullet (Figure 4.18a) as otherwise simply $x = [Li_i^x] \propto a_{Li}$ (see Figure 4.18b and Eq (4.4-8)).

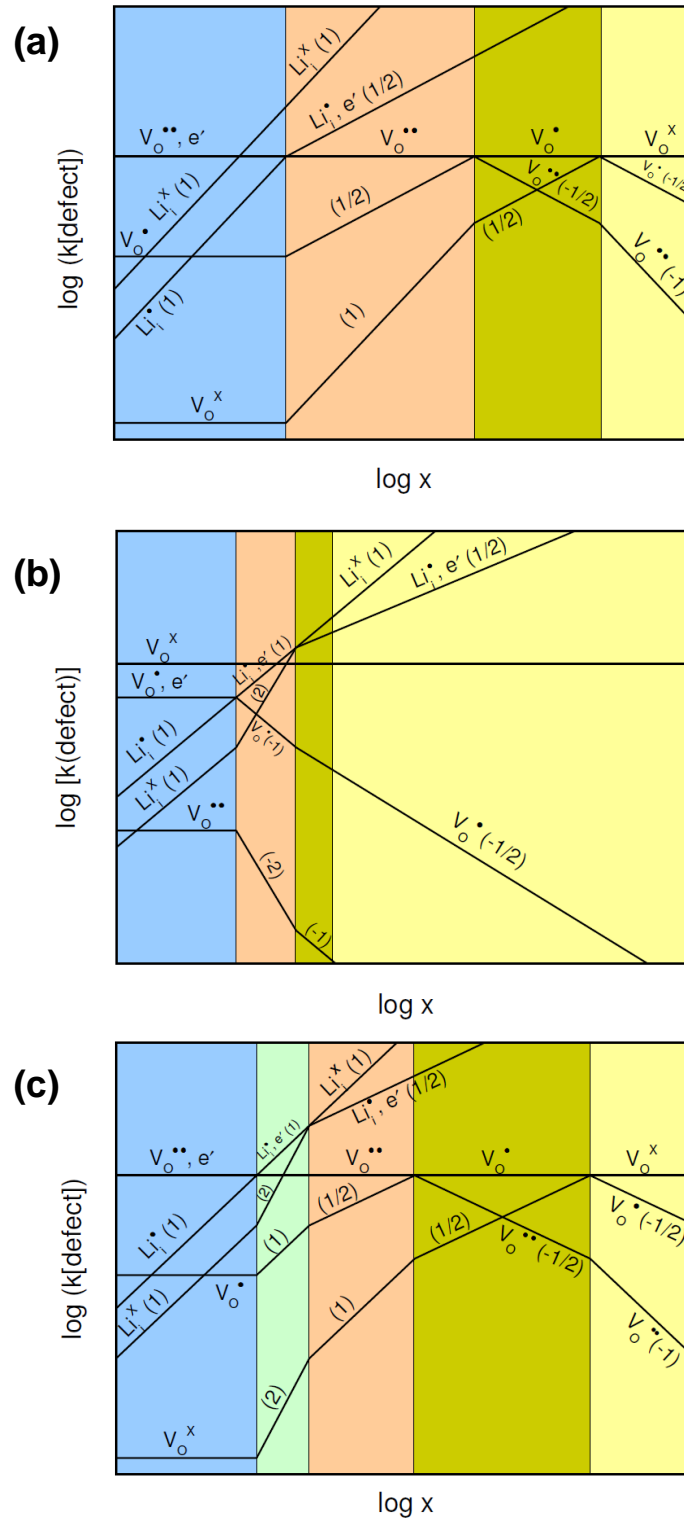


Figure 4.17: Comparison of defect concentration diagram as a function of x in $\text{Li}_x\text{TiO}_{2.8}$ (with constant δ): i) depending on initially predominant oxygen defects (a: $V_o^{..}$ and b: V_o^x being predominant) and ii) depending on the initial Li^+/e^- association condition (a: strong and c: weak association). Please note that for simplicity, the contribution $\log 2$ arising from the double charge of $V_o^{..}$ is suppressed.

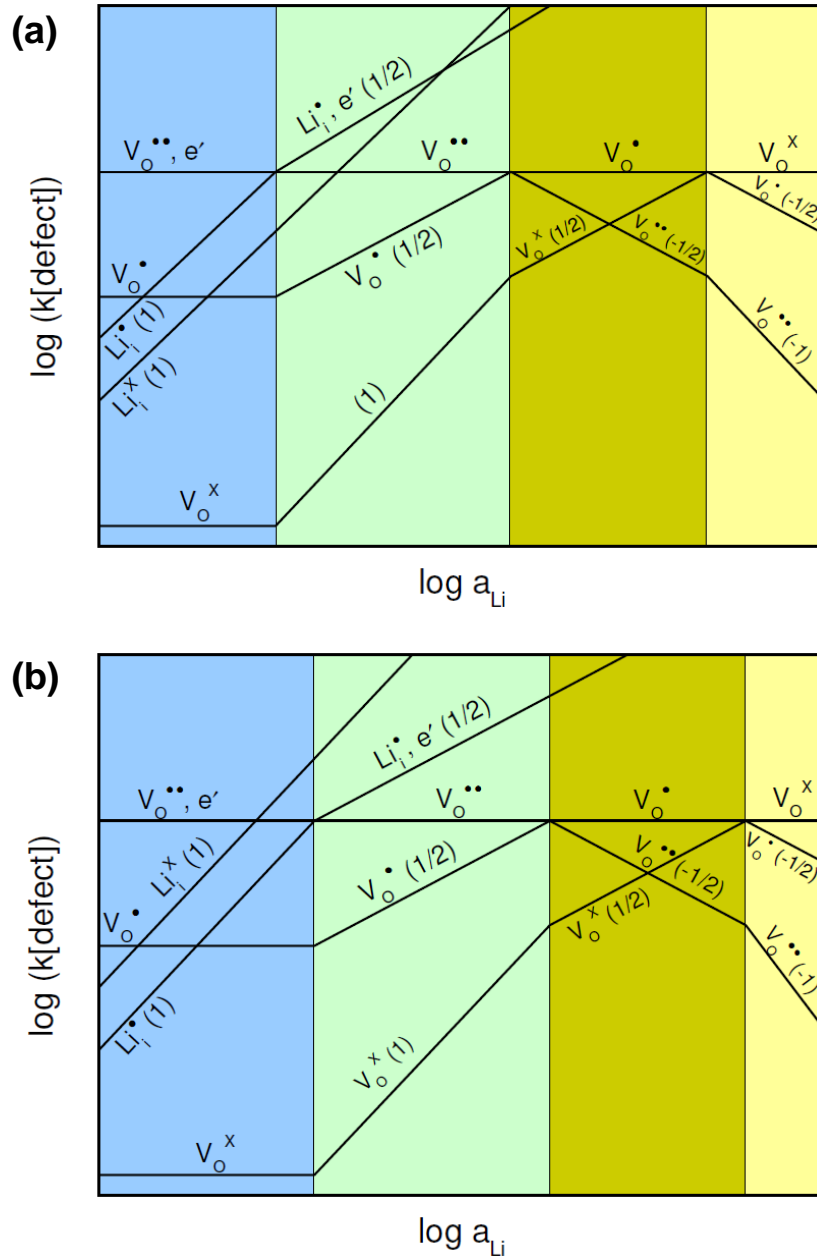


Figure 4.18: Variation in defect concentration in TiO_{2-δ} (with constant δ) as a function of Li-activity a_{Li} for the initial situation of (a) weak and (b) strong Li⁺/e⁻ association. Please note that for simplicity, the contribution log 2 arising from the double charge of V_o^{••} is suppressed.

The variation of the oxygen deficiency at given lithium content is even more instructive (Figures 4.19–4.21). Indeed, one starts of course with conditioning at high temperature and ends with lithium loading at room temperature. Then, if there is ion-electron association, on increased δ the electron concentration increases, but owing to increased trapping (ion-electron defect association) the free lithium carrier concentration decreases. Moreover, the trend of decrease in free lithium carrier concentration is dependent on the initial Li^+/e^- association condition (the ratio $[\text{Li}_i^\bullet]/[\text{Li}_i^x]$). This is highly important for Li-storage owing to the large impact on lithium diffusivity.

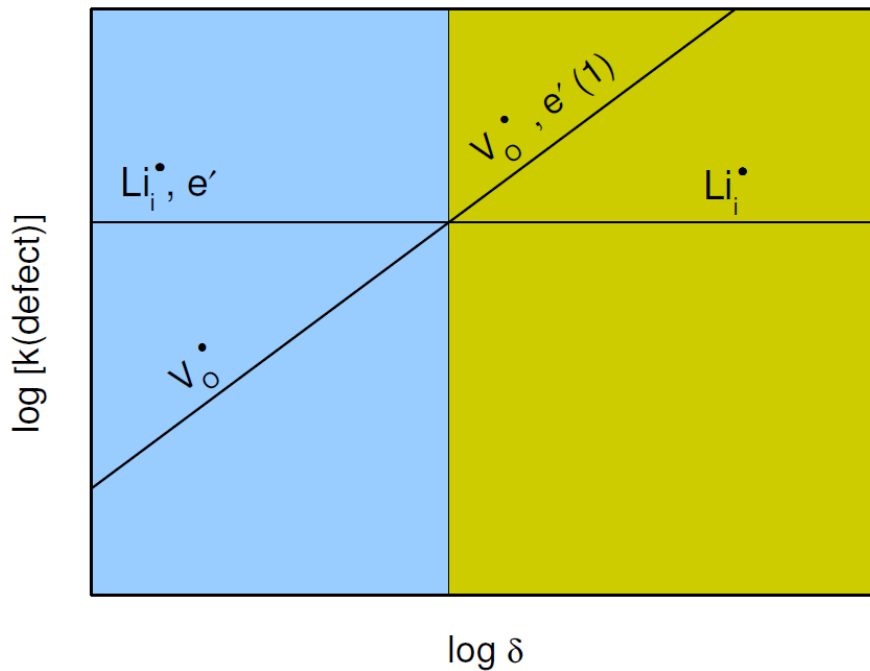


Figure 4.19: Defect concentration as a function of oxygen stoichiometry δ (with constant Li-content) for the initial situation of negligible Li^+/e^- association.

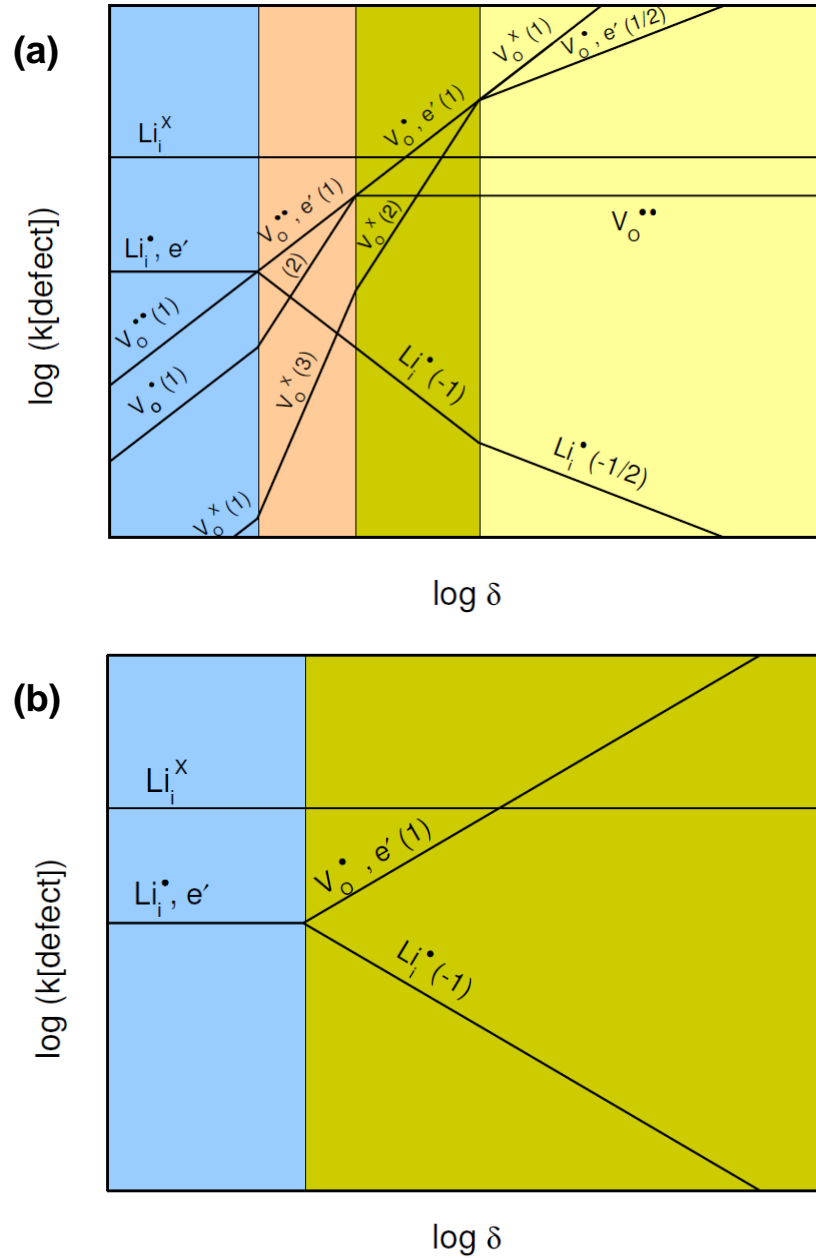


Figure 4.20: (a) Defect concentration as a function of oxygen stoichiometry δ (with constant Li-content) for the initial situation of strong Li^+/e^- association. Please note that for simplicity, the contribution $\log 2$ arising from the double charge of $\text{V}_o^{\bullet\bullet}$ is suppressed. (b) Special case of strong Li^+/e^- association and dominance of V_o^{\bullet} as far as δ is concerned; this simplified case is directly addressed in the calculation of D_{Li}^{δ} .

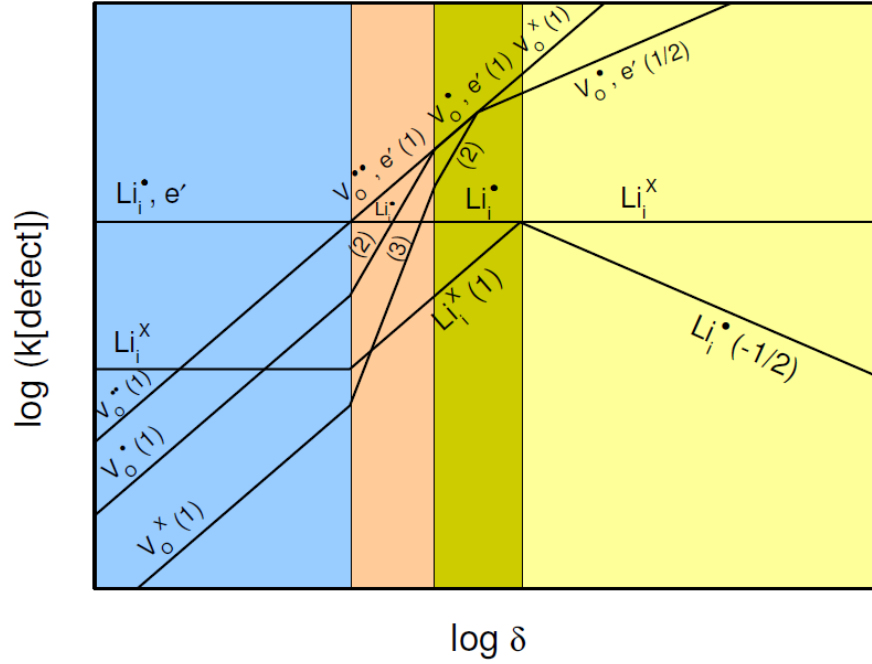


Figure 4.21: Defect concentration as a function of oxygen stoichiometry δ (with constant Li-content) for the initial situation of weak (intermediate) Li^+/e^- association. Please note that for simplicity, the contribution $\log 2$ arising from the double charge of $V_o^{\bullet\bullet}$ is suppressed.

4.4.2 Study on Lithium Diffusivity

Let me discuss the $D_{Li}^\delta(\delta)$ relation which directly gives us information on the effect of oxygen nonstoichiometry on Li-storage diffusion kinetics. Notwithstanding the fact that knowledge of the individual conductivities is very helpful in terms of electrode performance, the most relevant parameter for diffusion-controlled storage system is the chemical diffusion coefficient of lithium (D_{Li}^δ). As shortly discussed in the previous section, D_{Li}^δ is given by the ambipolar conductivity of lithium (σ_{Li}^δ) and an ambipolar concentration term that is determined by the carrier concentrations ($[e']$ and $[Li_i^\bullet]$) according to the following relation

$$D_{Li}^\delta \propto \sigma_{Li}^\delta \left(\frac{\chi_{e'}}{[e']} + \frac{\chi_{Li_i^\bullet}}{[Li_i^\bullet]} \right) \quad (4.4-10)$$

The trapping factors $\chi_{e'}$ and $\chi_{Li_i^\bullet}$ introduced in literature[49,54] make the relation general for ideal solutions. For non-ideal solution additional, corrections are

necessary[49,54] and I have to take into account internal reactions between the mobile species ($\chi_{e'}$ and $\chi_{Li_i^*}$). These are called differential electronic and ionic trapping factors[20,49,54] which can be also calculated on the basis of defect chemistry. As long as the electroneutrality equation can be written as $[e'] = \delta + [Li_i^*]$ (where $\delta = 2[V_o^{**}]$ or $\delta = [V_o^*]$), the result is $\chi_{e'} = \chi_{Li_i^*} = K_4^{-1}(2[e'] - \delta)^{-1}$, which simplifies to $(2K_4x)^{-1}$ for negligible δ and to $(K_4\delta)^{-1}$ for negligible $[Li_i^*]$. The situation is most simple for the extreme cases of negligible Li^+/e^- association (*i.e.* $\chi = 1$) and the case for very strong association ($x = [Li_i^X]$). For the latter case it can be shown that the ambipolar concentration term is simply given by x [20].

4.4.2.1 Negligible Initial Trapping Situation

For discussing the case of negligible Li^+/e^- association ($[Li_i^X] \ll [Li_i^*]$), I assume $[V_o^*] \gg [V_o^{**}]$, $[V_o^X]$ to simplify the situation. This is clearly shown in Figure 4.19. A relation between D_{Li}^δ and σ_{Li}^δ for the weak trapping initial situation is expressed as

$$D_{Li}^\delta \propto \sigma_{Li}^\delta \left(\frac{1}{[e']} + \frac{1}{[Li_i^*]} \right) \quad (4.4-11)$$

Further assuming identical concentration of electronic and ionic carriers in blue regime, Eq (4.4-11) can be modified as $D_{Li,I}^\delta \propto 2\sigma_{Li}^\delta(1/[Li_i^*]) \propto 2\sigma_{Li}^\delta(1/x)$. Here then in the blue regime (regime I in Figure 4.22a) I get $D_{Li}^\delta \propto u_{Li_i^*}$ for $u_{e'} \gg u_{Li_i^*}$ and $D_{Li}^\delta \propto u_{e'}$ for $u_{Li_i^*} \gg u_{e'}$, as the ambipolar conductivity is determined by the least conductive species (u : mobility). In the green regime where electron concentration dominates that of lithium ions, it follows a relation $D_{Li,II}^\delta \propto \sigma_{Li}^\delta(1/[Li_i^*]) \propto \sigma_{Li}^\delta(1/x)$. If the mobility of the electrons ($u_{e'}$) is greater than that of the lithium ions ($u_{Li_i^*}$) (see regime II in Figure 4.22a down), again no dependence of $D_{Li,II}^\delta$ on δ is anticipated according to $D_{Li,II}^\delta \propto u_{Li_i^*} = (1/2)D_{Li,I}^\delta$ (thus with half the proportionality constant),

yet a proportional increase of D_{Li}^δ with δ is obtained if $u_{Li_i} \gg u_e$ (see regime II in Figure 4.22a top) according to the following relation $D_{Li}^\delta \propto \delta u_e (1/x)$.

4.4.2.2 Strong Initial Trapping Situation

Now let me consider the case of strong trapping. Assuming an exergonic trapping reaction of Li_i^\bullet with a large enthalpy of association, one could extract the situation from Figure 4.20a, but it is more straightforward here to directly refer to Figure 4.20b where $[Li_i^X]$, $[V_o^{**}]$ and $[V_o^X]$ are neglected. Here again one can find a constancy for the blue regime (see regime I in Figure 4.22b) where $\delta < x$ ($D_{Li}^\delta \propto ux^{-1/2}$ where $u = u_{Li_i}$ for $u_e \gg u_{Li_i}$ and $u = u_e$ for $u_{Li_i} \gg u_e$). More interesting is the situation in the green regime (regime II, $\delta > x$). Here $D_{Li}^\delta \propto \sigma_{Li}^\delta / x$ decreases with δ , if $u_e \gg u_{Li_i}$ as $\sigma_{Li}^\delta = \sigma_{Li_i} \propto (x\delta)^{-1}$ (see regime II in Figure 4.22b down). For $u_{Li_i} \gg u_e$, however σ_{Li}^δ goes through a maximum (regime II in Figure 4.22b top), as initially the higher electron concentration does not overcompensate the lower mobility but for higher δ does so according to

$$D_{Li, IIa}^\delta \propto \delta x ([e'] \geq [Li_i^\bullet] \text{ and } u_e \gg u_{Li_i}) \text{ and } D_{Li, IIb}^\delta \propto (\delta x)^{-1} ([e'] \gg [Li_i^\bullet] \text{ and } u_e \ll u_{Li_i}).$$

This case is particularly interesting since the same behavior is seen in the storage experiments that were described in the previous section (see Chapter 4.3). This maximum in D_{Li}^δ can be explained only with a higher mobility for the lithium ions than for the electrons. Indeed, there are arguments for such an unusual mobility situation[43].

If mobility ratios are reverse (u_e exceeds u_{Li_i}), the interpretation must be the following to express the experimentally observed maximum. The local D_{Li}^δ decreases according to the defect chemical analysis but it is the increased rate of transport of the electrons to the active particle which is determined by σ_e which is responsible for the initial increase (see Figure 4.15).

4.4.2.3 Weak (Intermediate) Initial Trapping Situation

Finally I convert the case of weak (intermediate) association which refers to Figure 4.21 into $D_{Li}^\delta(\delta)$ (see Figure 4.22c). For this case, the calculation is more complex as it requires evaluation of χ as indicated above. Assuming $[e'] \approx [Li_i^{\bullet}] \gg [Li_i^X]$ in the blue regime, the trapping factors can be formulated as

$$\chi_{e'} = \frac{\partial[e']}{\partial([Li_i^X] + [Li_i^{\bullet}])} \quad \text{and} \quad \chi_{Li_i^{\bullet}} = \frac{\partial[Li_i^{\bullet}]}{\partial([Li_i^X] + [Li_i^{\bullet}])}$$

Since these two should be equal ($\chi_{e'} = \chi_{Li_i^{\bullet}} = \chi$), the calculation results in

$$D_{Li}^\delta \propto \chi \sigma_{Li}^\delta \left(\frac{1}{[e']} + \frac{1}{[Li_i^{\bullet}]} \right) \quad (4.4-12)$$

where $\chi = \frac{1}{1 + 2K_4[e']}$. This suggests for the blue regime (regime I in Figure 4.22c) a

constant $D_{Li,I}^\delta$ with an increase of δ regardless of mobility ratio, since the result is

$D_{Li,I}^\delta \propto u$ where $u = u_{Li_i^{\bullet}}$ for $u_{e'} \gg u_{Li_i^{\bullet}}$ and $u = u_{e'}$ for $u_{Li_i^{\bullet}} \gg u_{e'}$. On the other hand, the

trapping factor χ can be formulated as $\chi = \frac{1}{1 + K_4\delta}$ since electron concentration

for a situation with greater δ (regime II in Figure 4.22c) is the sum of that introduced by oxygen nonstoichiometry and Li_i^{\bullet} ($[e'] = \delta + [Li_i^{\bullet}]$). It modifies the Eq

(4.4-12) to $D_{Li,II}^\delta \propto \sigma_{Li}^\delta \frac{1}{1 + K_4\delta} \left(\frac{1}{x} \right)$. If the electron mobility is greater than the ionic

one ($u_{e'} \gg u_{Li_i^{\bullet}}$), as shown in regime II in Figure 4.22c down, obviously $D_{Li,II}^\delta$ is

inversely proportional to the oxygen stoichiometry at given condition according to

$$D_{Li,II}^\delta \propto \frac{1}{\delta} \quad ([e'] > [Li_i^{\bullet}] \text{ and } u_{e'} \gg u_{Li_i^{\bullet}}).$$

If $u_{Li_i^{\bullet}} \gg u_{e'}$, the dependence is slightly more complicated. In the subcase $[e'] \geq [Li_i^{\bullet}]$,

$D_{Li,II}^\delta$ follows as

$$D_{Li,II}^\delta \propto \sigma_{e'} \frac{1}{1 + K_4\delta} \left(\frac{1}{x} \right)$$

However, for the subcase $[e'] > [Li_i^\bullet]$ $D_{Li, II}^\delta$ follows

$$D_{Li, II}^\delta \propto \sigma_{Li_i^\bullet} \frac{1}{1 + K_4 \delta} \left(\frac{1}{x} \right)$$

In this case the dependence of D_{Li}^δ on δ is strictly negative (see regime II_b in Figure 4.22c top), while in the previous case $\sigma_{e'}$ introduced a counter-acting δ -dependence (see regime II_a in Figure 4.22c top). For great oxygen nonstoichiometries, D_{Li}^δ saturates as now the lack of Li⁺ charge carriers becomes limiting (see Table 4.5). All the relations of D_{Li}^δ for various initial conditions of the Li⁺/e⁻ association are summarized in Table 4.5.

Table 4.5: Calculated D_{Li}^δ for various initial conditions of the Li^+/e^- association $Li_i^\bullet + e' \rightleftharpoons Li_i^X$.

Regime	Case 1. Negligible association	Case 2. Strong association	Case 3. Weak (intermediate) association
I	(Condition) $[Li_i^\bullet] \approx [e'] \gg [Li_i^X]$ $[V_o^\bullet] \gg [V_o^{\bullet\bullet}], [V_o^X]$	(Condition) $[Li_i^X] \gg [Li_i^\bullet] \approx [e']$	(Condition) $[Li_i^\bullet] \approx [e'] > [Li_i^X]$
	(Lithium diffusivity) $D_{Li,I}^\delta \propto 2\sigma_{Li}^\delta \left(\frac{1}{x}\right)$	(Lithium diffusivity) $D_{Li,I}^\delta \propto \sigma_{Li}^\delta \left(\frac{1}{x}\right)$	(Lithium diffusivity) $D_{Li,I}^\delta \propto \sigma_{Li}^\delta$
	i) if $u_{e'} \gg u_{Li_i^\bullet}$	i) if $u_{e'} \gg u_{Li_i^\bullet}$	i) if $u_{e'} \gg u_{Li_i^\bullet}$
	$D_{Li,I}^\delta \propto u_{Li_i^\bullet} \propto \text{const}$	$D_{Li,I}^\delta \propto u_{Li_i^\bullet} \left(\frac{1}{\sqrt{x}}\right) \propto \text{const}$	$D_{Li,I}^\delta \propto u_{Li_i^\bullet} \propto \text{const}$
	ii) if $u_{e'} \ll u_{Li_i^\bullet}$	ii) if $u_{e'} \ll u_{Li_i^\bullet}$	ii) if $u_{e'} \ll u_{Li_i^\bullet}$
	$D_{Li,I}^\delta \propto u_{e'} \propto \text{const}$	$D_{Li,I}^\delta \propto u_{e'} \left(\frac{1}{\sqrt{x}}\right) \propto \text{const}$	$D_{Li,I}^\delta \propto u_{e'} \propto \text{const}$
II	(Condition) $[e'] > [Li_i^\bullet] \gg [Li_i^X]$	(Condition) $[Li_i^X] \gg [e'] > [Li_i^\bullet]$	(Condition) $[e'] (= \delta + [Li_i^\bullet]) > [Li_i^\bullet] > [Li_i^X]$
	(Lithium diffusivity) $D_{Li,II}^\delta \propto \sigma_{Li}^\delta \left(\frac{1}{x}\right)$	(Lithium diffusivity) $D_{Li,II}^\delta \propto \sigma_{Li}^\delta \left(\frac{1}{x}\right)$	(Lithium diffusivity) $D_{Li,II}^\delta \propto \sigma_{Li}^\delta \frac{1}{1+K_4\delta} \left(\frac{1}{x}\right)$
	i) if $u_{e'} \gg u_{Li_i^\bullet}$	i) if $u_{e'} \gg u_{Li_i^\bullet}$	i) if $u_{e'} \gg u_{Li_i^\bullet}$
	$D_{Li,II}^\delta \propto u_{Li_i^\bullet} \propto \text{const}$ ($= D_{Li,I}^\delta / 2$)	$D_{Li,II}^\delta \propto \left(\frac{1}{\delta}\right) \left(\frac{1}{x}\right) \propto \frac{1}{\delta}$	$D_{Li,II}^\delta \propto \sigma_{Li_i^\bullet} \left(\frac{1}{1+K_4\delta}\right) \left(\frac{1}{x}\right) \propto \frac{1}{\delta}$
	(II _a / II _b) ii) if $u_{e'} \ll u_{Li_i^\bullet}$	ii) if $[e'] \geq [Li_i^\bullet]$ and $u_{e'} \ll u_{Li_i^\bullet}$	ii) if $[e'] \geq [Li_i^\bullet]$ and $u_{e'} \ll u_{Li_i^\bullet}$
	$D_{Li,II}^\delta \propto \delta u_{e'} \left(\frac{1}{x}\right) \propto \delta$	$D_{Li,IIa}^\delta \propto \delta x \propto \delta$	$D_{Li,IIa}^\delta \propto \sigma_{e'} \frac{1}{1+K_4\delta} \left(\frac{1}{x}\right) \propto \text{const}$
	iii) if $[e'] \gg [Li_i^\bullet]$ and $u_{e'} \ll u_{Li_i^\bullet}$	iii) if $[e'] > [Li_i^\bullet]$ and $u_{e'} \ll u_{Li_i^\bullet}$	
	$D_{Li,IIb}^\delta \propto \left(\frac{1}{\delta}\right) \left(\frac{1}{x}\right) \propto \frac{1}{\delta}$	$D_{Li,IIb}^\delta \propto \sigma_{Li_i^\bullet} \frac{1}{1+K_4\delta} \left(\frac{1}{x}\right) \propto \frac{1}{\delta}$	
III	-	-	(Condition) $[e'] \gg [Li_i^X] > [Li_i^\bullet]$
			(Lithium diffusivity) $D_{Li,III}^\delta \propto \sigma_{Li_i^\bullet} \frac{\delta}{K_4\delta} \propto \text{const}$

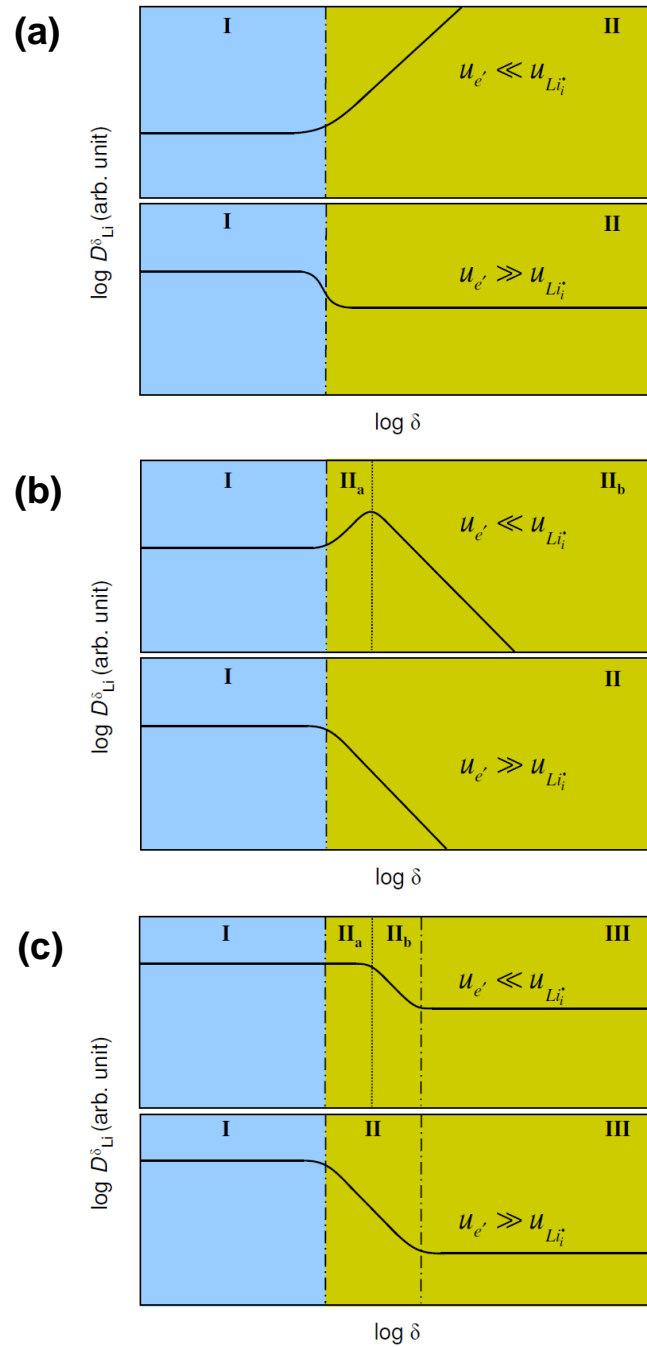


Figure 4.22: Dependence of chemical diffusion coefficient of Li in $\text{Li}_x\text{TiO}_{2-\delta}$ on oxygen nonstoichiometry δ for various initial conditions of the Li^+/e^- association $\text{Li}_i^{\bullet} + \text{e}' \rightleftharpoons \text{Li}_i^X$: (a) negligible-, (b) strong- and (c) weak (intermediate)-association. Unlike the concentration diagrams the realistic smoothening at the transitions is indicated.

4.5 Conclusion

In this chapter, a systematic study of charge carriers concentrations effects on the overall Li storage performance was carried out using multiple experimental techniques as well as a theoretical defect chemical analysis. In Chapter 4.3, novel efficient titania anodes were prepared by using oxygen-deficient anatase nanoparticles and effects of frozen-in native defects on Li storage were studied. The frozen oxygen deficiency was achieved *via* a hydrogen-thermal treatment. The H₂-thermally treated TiO_{2-δ} nanoparticles showed greatly improved electrochemical lithium storage properties because of the increased electronic transport, compared with untreated (pristine) and thermally annealed (under inert condition) titania nanoparticles. Interestingly, too high a degree of reduction proves detrimental because of depression of free Li⁺ concentration owing to association with excess electrons. In conjunction with the experimental results, in Chapter 4.4 the detailed defect chemical analysis of lithium storage in oxygen-deficient nonstoichiometric lithium titanate was discussed. A simplified version of the defect chemistry of titania was considered but included lithium defects that occur on charging titania in a Li-based cell. This allows one to understand the performance of a titania anode as a function of oxygen nonstoichiometry in detail. The decisive defect chemical analyses for deriving defect concentrations and chemical diffusion coefficients for lithium are indicated.

I want to emphasize an important finding in the current study that ionic-electronic defect association ($Li_i^\bullet + e' \rightleftharpoons Li_i^x$ and $V_o^{\bullet\bullet} + 2e' \rightleftharpoons V_o^\bullet + e' \rightleftharpoons V_o^x$) can significantly affect transport properties of lithium in titania depending on the initial trapping condition. The experimentally observed maximum in effective lithium diffusivity and storage capacity can have the explanations according to the ranking of the different mobilities. 1) A maximum in the local chemical diffusion coefficient (predicted for strong trapping and $u_{Li_i} \gg u_{e'}$). 2) A decrease of local diffusion coefficient (under weak or strong conditions) counteracting increased electronic transport to the particle to be filled. At any rate, these considerations show the large impact of the defect chemistry on the overall lithium storage performance.

Combining the storage experiments (Chapter 4.3) and the theoretical defect chemical analysis (Chapter 4.4), as a result I demonstrate here that achieving well-balanced ionic and electronic conductivity is essential for high performance Li-batteries, and therefore a careful consideration of electronic/ionic charge carriers concentrations should be conducted in order to strategically design efficient anode/cathode materials for lithium batteries.

References

- [1] C. Li, L. Gu, J.-W. Tong, J. Maier, *ACS Nano* **2011**, *5*, 2930.
- [2] D. Wang, D. Choi, J. Li, Z. Yang, Z. Nie, R. Kou, D. Hu, C. Wang, L.V. Saraf, J. Zhang, I.A. Aksay, J. Liu, *ACS Nano* **2009**, *3*, 907.
- [3] Y.-H. Huang, J. B. Goodenough, *Chem. Mater.* **2008**, *20*, 7237.
- [4] L.J. Fu, H. Liu, H.P. Zhang, C. Li, T. Zhang, Y.P. Wu, H.Q. Wu, *J. Power Sources* **2006**, *159*, 219.
- [5] R. Dominko, M. Gaberscek, M. Bele, D. Mihailovic, J. Jamnik, *J. Eur. Ceram. Soc.* **2007**, *27*, 909.
- [6] I. Moriguchi, R. Hidaka, H. Yamada, T. Kudo, H. Murakami, N. Nakashima, *Adv. Mater.* **2005**, *18*, 69.
- [7] F.-Y. Su, C. You, Y.-B. He, W. Lv, W. Cui, F. Jin, B. Li, Q.-H. Yang, F. Kang, *J. Mater. Chem.* **2010**, *20*, 9644.
- [8] Y.-G. Guo, Y.-S. Hu, W. Sigle, J. Maier, *Adv. Mater.* **2007**, *19*, 2087.
- [9] B.-L. He, B. Dong, H.-L. Li, *Electrochem. Commun.* **2007**, *9*, 425.
- [10] S.Y. Chung, J. T. Bloking, Y. M. Chiang, *Nature Mater.* **2002**, *1*, 123.
- [11] P.S. Herle, B. Ellis, N. Coombs, L.F. Nazar, *Nature Mater.* **2004**, *3*, 147.
- [12] H. Tukamoto, A.R. West, *J. Electrochem. Soc.* **1997**, *144*, 3164.
- [13] F. Coustier, J. Hill, B.B. Owens, S. Passerini, W.H. Smyrl, *J. Electrochem. Soc.* **1999**, *146*, 1355.
- [14] H. Li, Z. Wang, L. Chen, X. Huang, *Adv. Mater.* **2009**, *21*, 4593.
- [15] M.S. Islam, D.J. Driscoll, C.A.J. Fisher, P.R. Slater, *Chem. Mater.* **2005**, *17*, 5085.
- [16] C.A.J. Fisher, V.M.H. Prieto, M.S. Islam, *Chem. Mater.* **2008**, *20*, 5907.
- [17] B. Ellis, P.S. Herle, Y.-H. Rho, L.F. Nazar, R. Dunlap, L. K. Perry, D.H. Ryan, *Faraday Discuss.* **2007**, *134*, 119.
- [18] H.C. Shin, S.B. Park, H. Jang, K.Y. Chung, W.I. Cho, C.S. Kim, B.W. Cho, *Electrochim. Acta* **2008**, *53*, 7946.
- [19] R. Amin, C. Lin, J. Maier, *Phys. Chem. Chem. Phys.* **2008**, *10*, 3524.
- [20] J. Maier, R. Amin, *J. Electrochem. Soc.* **2008**, *155*, A339.

- [21] R. Amin, C. Lin, J. Peng, K. Weichert, T. Acartürk, U. Starke, J. Maier, *Adv. Funct. Mater.* **2009**, *19*, 1697.
- [22] A. Weibel, R. Bouchet, P. Knauth, *Solid State Ionics* **2006**, *177*, 229.
- [23] R. Waser, *J. Am. Ceram. Soc.* **1991**, *74*, 1934.
- [24] I. Denk, W. Münch, J. Maier, *J. Am. Ceram. Soc.* **1995**, *78*, 3265.
- [25] J. Maier, *Phys. Chem. Chem. Phys.* **2003**, *5*, 2164.
- [26] D. Liu, Y. Zhang, P. Xiao, B.B. Garcia, Q. Zhang, X. Zhou, Y.-H. Jeong, G. Cao, *Electrochim. Acta* **2009**, *54*, 6816.
- [27] P. Kofstad, Nonstoichiometry, Electrical Conductivity and Diffusion in Binary Metal Oxides. **1972**.
- [28] A. Magneli, B. Blomberg-Hansson, L. Kihlberg, G. Sundkvist, *Acta. Chem. Scand.* **1955**, *9*, 1382.
- [29] G. Li, L. Li, J. Boerio-Goates, B.F. Woodfield, *J. Am. Chem. Soc.* **2005**, *127*, 8659.
- [30] L. Kavan, K. Kratochvilová, M. Grätzel, *J. Electroanal. Chem.* **1995**, *394*, 93.
- [31] Y.H. Xu, G.P. Yin, Y.L. Ma, P.J. Zuo, X.Q. Cheng, *J. Power Sources* **2010**, *195*, 2069.
- [32] D. Aurbach, M.D. Levi, E. Levi, H. Teller, B. Markovsky, G. Salitra, *J. Electrochem. Soc.* **1998**, *145*, 3024.
- [33] M.D. Levi, G. Salitra, B. Markovsky, H. Teller, D. Aurbach, U. Heider, L. Heider, *J. Electrochem. Soc.* **1999**, *146*, 1279.
- [34] M. Takahashi, S. Tobishima, K. Takei, Y. Sakurai, *Solid State Ionics* **2002**, *148*, 283.
- [35] A.J. Bard, L.R. Faulkner, *Electrochemical Methods: Fundamentals and Applications* 2nd ed. **2001**, P231.
- [36] D.Y.W. Yu, C. Fietzek, W. Weydanz, K. Donoue, T. Inoue, H. Kurokawa, S. Fujitani, *J. Electrochem. Soc.* **2007**, *154*, A253.
- [37] M.D. Levi, K. Gamolsky, D. Aurbach, U. Heider, R. Oesten, *J. Electroanal. Chem.* **1999**, *477*, 32.
- [38] L. Kavan, M. Grätzel, S.E. Gilbert, C. Klemenz, H.J. Scheel, *J. Am. Chem. Soc.* **1996**, *118*, 6716.

- [39] M. Bousa, B. Laskova, M. Zukalova, J. Prochazka, A. Chou, L. Kavan, *J. Electrochem. Soc.* **2010**, *157*, A1108.
- [40] D. Aurbach, M.D. Levi, E. Levi, *Solid State Ionics* **2008**, *179*, 742.
- [41] Y. Zhu, C. Wang, *J. Phys. Chem. C* **2010**, *114*, 2830.
- [42] K. Tang, X. Yu, J. Sun, H. Li, X. Huang, *Electrochim. Acta* **2011**, *56*, 4896.
- [43] M.L. Sushko, K.M. Rosso, J. Liu, *J. Phys. Chem. C* **2010**, *114*, 20277.
- [44] S.N. Kerisit, K.M. Rosso, Z. Yang, J. Liu, *J. Phys. Chem. C* **2010**, *114*, 19096.
- [45] N.A. Deskins, M. Dupuis, *Phys. Rev. B* **2007**, *75*, 195212.
- [46] M. Wagemaker, R. van de Krol, A.P.M. Kentgens, A.A. van Well, F.M. Mulder, *J. Am. Chem. Soc.* **2001**, *123*, 11454.
- [47] M. Wagemaker, W.H.J. Borghols, E.R.H. van Eck, A.P.M. Kentgens, G.J. Kearley, F.M. Mulder, *Chem. Eur. J.* **2007**, *13*, 2023.
- [48] C.L. Olson, J. Nelson, M.S. Islam, *J. Phys. Chem. B* **2006**, *110*, 9995.
- [49] J. Maier, *J. Am. Ceram. Soc.* **1993**, *76*, 1212.
- [50] S. Lunell, A. Stashans, L. Ojamae, H. Lindstrom, A. Hagfeldt, *J. Am. Chem. Soc.* **1997**, *119*, 7374.
- [51] A. Stashans, S. Lunell, R. Bergström, A. Hagfeldt, S.E. Lindquist, *Phys. Rev. B* **1996**, *53*, 159.
- [52] F.A. Kröger, *Chemistry of Imperfect Crystals*, North Holland Publ. Comp., Amsterdam, **1964**.
- [53] J. Maier, *Physical Chemistry of Ionic Materials: Ions and Electrons in Solids*, John Wiley & Sons, Chichester, **2004**.
- [54] J. Maier, G. Schwitzgebel, *Phys. Status Solidi B* **1982**, *113*, 535.

5

Effects of Defect Chemistry on Lithium Storage II.

Case Study of Extrinsic Defects

This chapter deals with another example of investigating effects of defect chemistry (ionic/electronic charge carriers) in nanostructured TiO₂ on Li storage and transport, but using extrinsic defects entering the lattice in solid solution. Mesoporous niobium-doped TiO₂ ($mp\text{-Ti}_{1-y}\text{Nb}_y\text{O}_{2+\delta}$) nanostructures were successfully synthesized by sol-gel preparation method. Their electrochemical performances with respect to lithium storage clearly indicated that both strategies are effective to improve Li storage properties of titania electrodes. Moreover, similarly with the case study using frozen-in native defects (Chapter 4), it was also found in this study that the electron-ion association *i.e.* $\text{Li}_i^\bullet + e' \rightleftharpoons \text{Li}_i^x$ and $\text{Nb}_i^\bullet + e' \rightleftharpoons \text{Nb}_i^x$ plays a very important role in determining overall Li storage performance of titania electrode.

5.1 Introduction

Impurities added intentionally to a solid solution (homogeneous doping) to create or suppress other defects are called dopants. Dopants can be characterized as either donors or acceptors; owing to electroneutrality donors (D_M^*) donate electrons to the lattice, whereas acceptors (A_M') annihilate electrons of the lattice (forming holes). When a semiconductor is doped with these impurities, the semiconductor becomes extrinsic and energy levels of the impurities are introduced to the host. For example, an electron is donated to the conduction band (n -type) of silicon atom if the silicon atom is doped with arsenic (donor), whereas a hole is created in the valence band (p -type) when it is doped with a boron atom (acceptor).

The concept of homogeneous lattice doping with extrinsic dopants has largely been used also in the field of Li-batteries. Quite often, the introduction of dopants into metal oxide materials has been aimed to improve poor electrical conductivities[1,2] or sometimes to facilitate phase transition kinetics (for those electrode materials, where the phase transition occurs upon the charge/discharge process)[3], resulting ultimately in an improvement of overall electrochemical performance of electroactive materials. For TiO_2 electrodes, for example donor doping with Nb^{5+} cations has been recently studied to improve its lithium storage ability by means of the increased electronic conductivity of the material[4]. However, a systematic study on effects of ionic/electronic charge carriers concentrations on lithium storage and transport is almost absent in the literature. A simple rule (“rule of homogeneous doping”[5]) states that and now also ionic defect concentrations are varied according to their charge.

In Chapter 5.2, niobium doped TiO_2 nanostructures with mesoporosity ($mp\text{-Ti}_{1-y}\text{Nb}_y\text{O}_{2+\delta}$) were prepared by sol-gel synthetic method and their electrochemical performance in terms of lithium storage is discussed in detail. Among various types of dopants, niobium was chosen as a donor dopant, because of its similar ionic radii with that of tetravalent titanium ion, thereby allowing for chemical compatibility with the host material TiO_2 . It is already known that niobium exists in pentavalent state at least in pristine, non-lithiated TiO_2 and

substitutes for Ti^{4+} . As a consequence the concentration of all negative electronic and ionic point defects is increased individually. Therefore, varying the concentration of Nb^{5+} induces different concentration of electrons, and thus it allows one to conduct a systematic study on effects of charge carrier concentrations on electrochemical lithium storage properties in the given material. Then in Chapter 5.3 the point defect chemistry of lithium storage with $\text{Li}_x\text{Ti}_{1-y}\text{Nb}_y\text{O}_{2+\delta}$ is addressed using mass action laws and balance equations in order to understand the performance of a titania anode as a function of lithium content or activity as well as dopant (niobium) concentration, furthermore emphasize its great importance to practical lithium battery applications.

5.2 Experimental Results

5.2.1 Materials Preparation

For the typical synthesis of mesoporous TiO_2 and $\text{Ti}_{1-y}\text{Nb}_y\text{O}_{2+\delta}$ nanoparticles, titanium (IV) isopropoxide ($\text{C}_{12}\text{H}_{28}\text{O}_4\text{Ti}$, 97%, Aldrich), niobium (V) ethoxide ($\text{C}_{10}\text{H}_{25}\text{O}_5\text{Nb}$, 99.95%, Aldrich), 2-propanol (Merck), and acetic acid (100%, Roth) were used as received without further purification. The *mp*- $\text{Ti}_{1-y}\text{Nb}_y\text{O}_{2+\delta}$ nanoparticles were prepared by a sol-gel synthetic route. 0.5 M of titanium isopropoxide solution in 2-propanol was prepared and stirred for 30 min followed by slowly adding appropriate volume of niobium (V) ethoxide for each doping level (5 ~ 20 mol%). After a vigorous stirring for further 30 min, a homogeneous mixture of the precursor solution was obtained. The obtained mixed precursor solutions were added dropwise into an aqueous solution containing acetic acid and 2-propanol (50:50 in vol.%) followed by further vigorous stirring for 2 h. Distilled water was introduced dropwise into the solution for a gelification. After 30 min of aging at room temperature, the elastic gel was dried at 373 K overnight. Calcination was performed at 673 K for 5 hours in air with a heating/cooling rate of $10 \text{ K}\cdot\text{min}^{-1}$.

5.2.2 Results and Discussion

5.2.2.1 Structural Characterization

Figure 5.1a shows powder XRD pattern of synthesized $mp\text{-Ti}_{1-y}\text{Nb}_y\text{O}_{2+\delta}$ nanostructures depending on the doping level (0 ~ 20 mol% Nb). Up to Nb concentration of 15 mol%, samples exhibit crystal structure of pure anatase phase, showing the space group of $I4_1/amd$ (JCPDS 21-1272). As shown in Figure 5.1b and Table 5.1, lattice parameters (a- and c-axis) vary almost linearly with a Nb concentration up to 15 mol% according to Vegard's law[6]. At 20 mol% Nb concentration, the increase in the lattice parameter saturates and extra diffraction peaks were detected from XRD pattern indicating a formation of second phases. Based on the diffraction peaks analysis, the formed extra phases are most likely a combination of multiple phases, *e.g.* titanium niobium oxide (TiNb_2O_7) and niobium pentoxides (Nb_2O_5)[7,8]. This result nicely matches with reported phase diagram for $\text{Li}_{1+x}\text{Nb}_{1-x}\text{Ti}_x\text{O}_3$ by Yamamoto *et al.* which is shown in Scheme 5.1. The above observations demonstrate that the solid solubility limit of Nb into anatase TiO_2 lattice lies in between 15 and 20 mol%. The determined solid solubility limit is in a good agreement with the previous report (15 ± 4 mol%) on Nb-doped TiO_2 (anatase) synthesized by hydrothermal process[9,10].

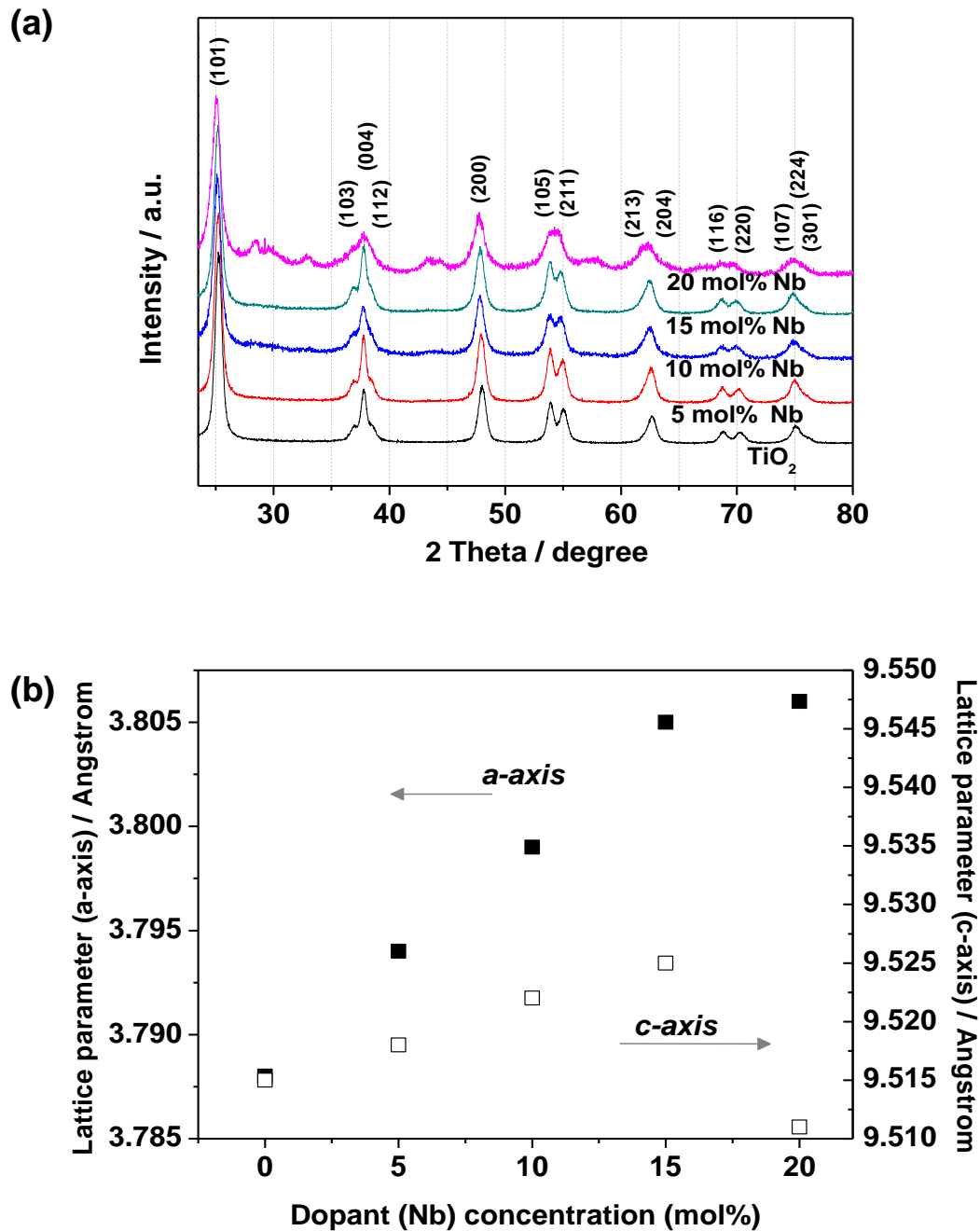
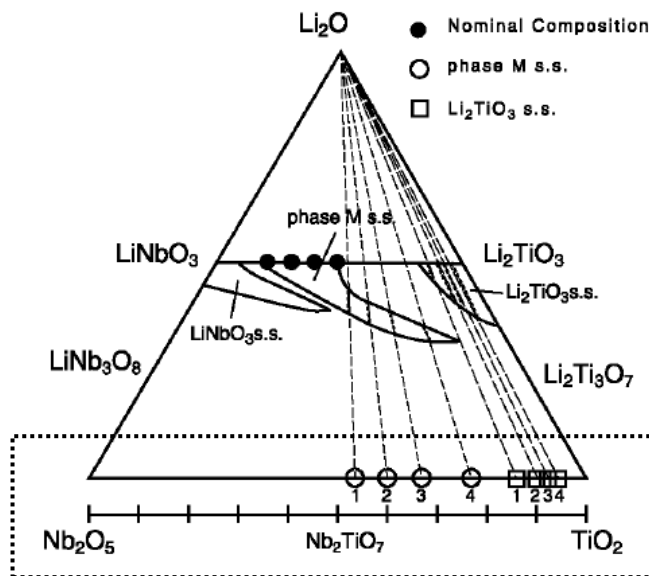


Figure 5.1: (a) XRD patterns of pure- and Nb-doped mesoporous TiO_2 with different dopant concentration (5 – 20 mol%). (b) Variation of lattice parameters (a- and c-axis) of Nb-doped anatase mesoporous TiO_2 synthesized by sol-gel method as a function of dopant concentration.



Scheme 5.1: Phase development in the formula $\text{Li}_{1+x}\text{Nb}_{1-x}\text{Ti}_x\text{O}_3$ with the nominal composition x [11]. Please note that only the information shown in the x-axis (dotted box, binary phase diagram of $\text{TiO}_2\text{-Nb}_2\text{O}_5$) was taken for this study.

As seen in Figure 5.2a, the average crystallite size of $mp\text{-Ti}_{1-y}\text{Nb}_y\text{O}_{2+\delta}$ nanostructures (determined from XRD measurement using WPPD method) was found to be *ca.* 15 ~ 20 nm, while those calculated using S_{BET} showed slightly smaller values of 10 ~ 13 nm. For both cases, a slight decrease in the crystallite size was observed most probably due to an induced strain by Nb-doping in the lattice[12]. Nonetheless, such small change in crystallite size with Nb-doping within solid solubility limit suggests that an effect of Nb-doping on the microstructure of TiO_2 can be assumed to be insignificant. Figure 5.2b shows nitrogen adsorption/desorption isotherms of synthesized mesoporous TiO_2 . It depicts the nature of the uniform mesopores (less than 10 nm in diameter) with narrow pore size distribution (Figure 5.2b inset), showing typical Type IV behavior with clear capillary condensation. This mesoporosity was maintained even after homogeneous Nb-doping, exhibiting similar isotherms at all dopant concentrations within the solid solubility limits.

Table 5.1: Crystallographic parameters for $mp\text{-Ti}_{1-y}\text{Nb}_y\text{O}_{2+\delta}$ with various dopant concentration ($y = 0.05 - 0.15$).

	$mp\text{-TiO}_2$	$mp\text{-Ti}_{0.95}\text{Nb}_{0.05}\text{O}_{2+\delta}$	$mp\text{-Ti}_{0.90}\text{Nb}_{0.10}\text{O}_{2+\delta}$	$mp\text{-Ti}_{0.85}\text{Nb}_{0.15}\text{O}_{2+\delta}$
Space group	$I4_1/amd$	$I4_1/amd$	$I4_1/amd$	$I4_1/amd$
Lattice parameters [Å]	a 3.788 c 9.515	a 3.794 c 9.518	a 3.799 c 9.522	a 3.805 c 9.525
Unit cell volume [Å ³]	136.53	137.01	137.43	137.90

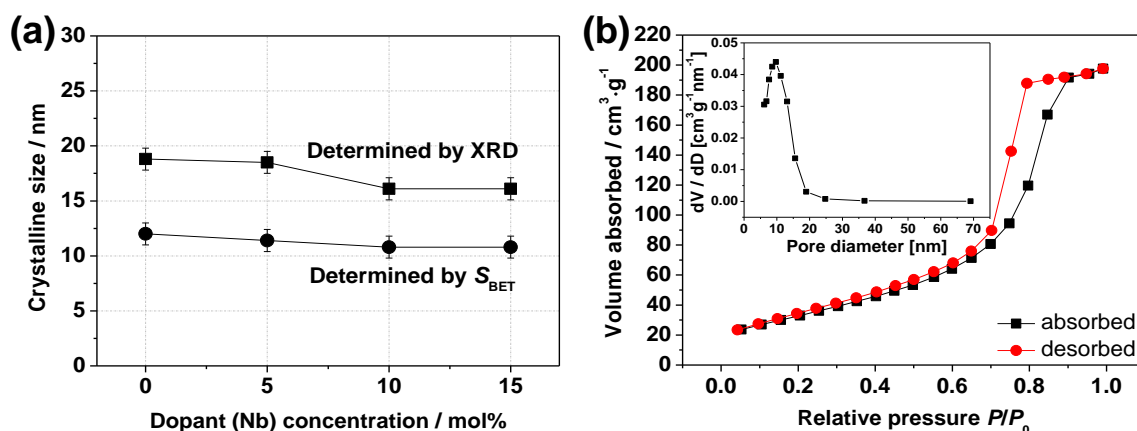
**Figure 5.2:** (a) Crystallite sizes of $mp\text{-Ti}_{1-y}\text{Nb}_y\text{O}_{2+\delta}$ nanostructures determined by XRD result (■) and BET surface area (●) as a function of dopant concentration. (b) Nitrogen adsorption and desorption isotherms and pore size distribution (inset) of synthesized mesoporous TiO_2 nanostructures.

Figure 5.3 shows HRTEM images of synthesized mesoporous undoped (Figure 5.3a), 10 mol% (Figure 5.3b), and 20 mol% (Figure 5.3c) Nb-doped titania nanostructures. Figure 5.3a indicates a successful preparation of fine TiO_2 crystallites with narrow size distribution (15 ~ 20 nm). The selected area electron diffraction (SAED) pattern (Figure 3a inset) showing diffraction spots all located on multiple concentric circles, which are attributed to different lattice planes of the anatase (*e.g.* (101), (004), (200), and (211)) confirms the formation of finite amount of single TiO_2 crystallite with random orientation. The 10 mol% Nb-doped sample (Figure 5.3b) still shows pure anatase TiO_2 phase without second phases.

In Figure 5.3d, TEM images of $mp\text{-Ti}_{0.90}\text{Nb}_{0.10}\text{O}_{2+\delta}$ nanostructures with corresponding elemental maps for Ti, O, and Nb content are shown. It is clearly

shown that dopant (Nb) element is homogeneously distributed in TiO_2 host matrix. However, in Figure 5.3c, slightly decreased crystallite size with additional diffuse spots in SAED pattern for the 20 mol% Nb-doped titania sample implies a formation of second phases existing together with anatase TiO_2 as also confirmed from the XRD result (Figure 5.1a).

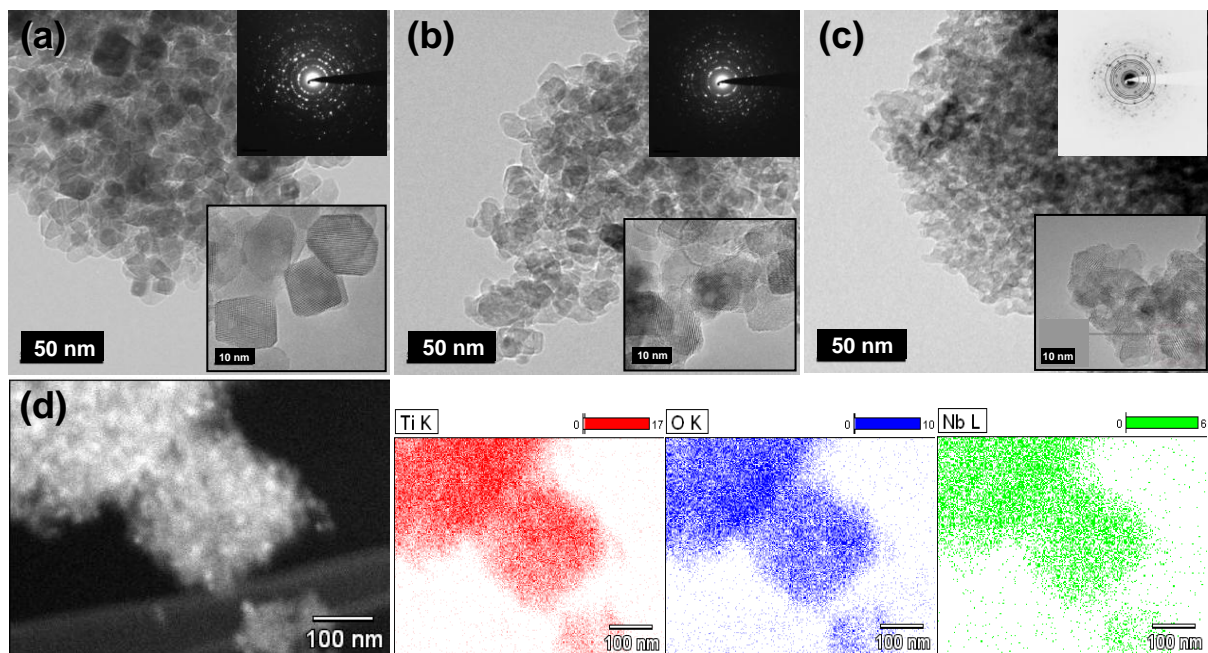
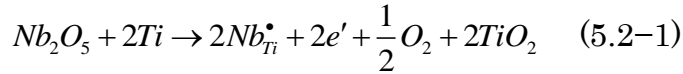


Figure 5.3: HRTEM images of (a) undoped, (b) 10 mol% Nb-doped, (c) 20 mol% Nb-doped mesoporous TiO_2 (insets; magnified views and SAED patterns of corresponding samples). (d) Elemental maps of Ti, O, and Nb content in $mp\text{-Ti}_{1-y}\text{Nb}_y\text{O}_{2+\delta}$ sample.

5.2.2.2 Defect Chemistry and Conductivity Study

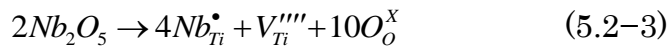
As previously mentioned, donor doping of TiO₂ is achieved by an incorporation of a cation of valence greater than +4 into the regular Ti lattice site. When TiO₂ is doped by Nb⁵⁺, niobium atom that sits on a titanium site can be considered as a point defect Nb_{Ti}^{\bullet} . For reasons of electroneutrality, charge compensation occur either predominantly by electronic or by ionic charge carriers, depending on a preparation condition, for instance oxygen partial pressure and temperature[13]. The combination of electroneutrality and mass action laws predicts the detailed impact on the individual concentrations. The incorporation of Nb⁵⁺ into TiO₂ lattice can be expressed in following Kroger-Vink notation as



In the regime of low oxygen partial pressures, the majority defects are given by the electronic charge compensation of Nb⁵⁺, and hence the electronic conductivity is mainly dependent on dopant concentration rather than P_{O_2} :

$$n = [Nb_{Ti}^{\bullet}] \quad (5.2-2)$$

On the other hand, at relatively high oxygen partial pressures (the boundary between low and high P_{O_2} regime was found to be at $\sim 10^{-14}$ bar *via* our conductivity measurements), dopants are ionically compensated, and Eq (5.2-1) is better written as



with

$$4[V_{Ti}'''] = [Nb_{Ti}^{\bullet}] \quad (5.2-4)$$

As a consequence of the oxygen incorporation equilibrium, the electronic conductivity of Nb-doped TiO₂ in this regime turns out to be dependent on both P_{O_2} and Nb⁵⁺ concentration, following the relation below

$$n = \left(\frac{K_i^4 [Nb_{Ti}^{\bullet}]}{4K_1} \right)^{1/4} P_{O_2}^{-1/4} \quad (5.2-5)$$

where $K_i = np$ and $K_1 = [V_{Ti}''''']p^4P_{O_2}^{-1}$. This has been experimentally confirmed by our P_{O_2} dependent conductivity measurements (The defect diagram for whole oxygen partial pressure regime proposed by Sheppard[14] is shown in Figure 5.4 inset). Figure 5.4 shows the oxygen partial pressures dependence of the bulk conductivity of 10% Nb-doped mesoporous TiO_2 ($mp\text{-}Ti_{0.90}Nb_{0.10}O_{2+\delta}$) samples at 823 K. While no oxygen partial pressure dependence was observed at low P_{O_2} regime (electronic charge compensation), the slope of $-1/4$ is clearly shown at relatively high P_{O_2} regime which suggests that charge compensation occurs mainly by titanium vacancies (V_{Ti}'''''). As mentioned, the crossover between low and high P_{O_2} regime was determined as $\sim 10^{-14}$ bar.

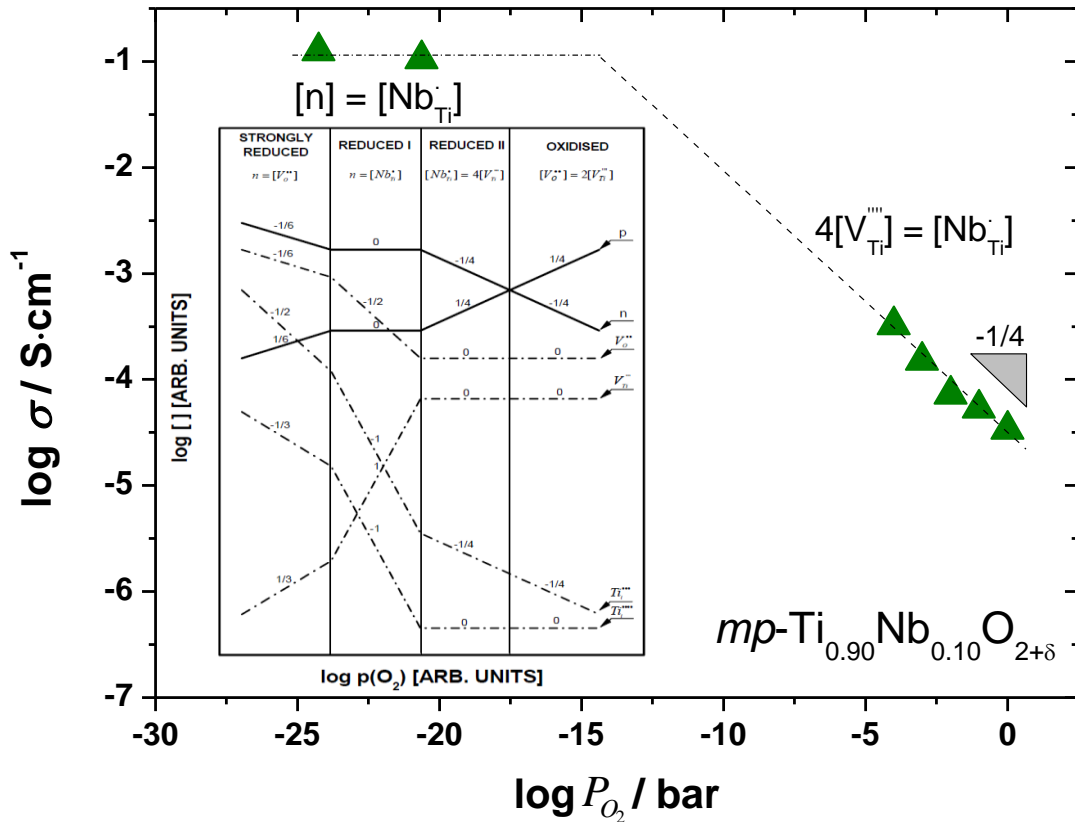


Figure 5.4: Measured oxygen partial pressure dependence of bulk conductivity for $mp\text{-}Ti_{0.90}Nb_{0.10}O_{2+\delta}$ measured at 823 K (inset: proposed defect diagram by Sheppard for Nb-doped TiO_2 for whole P_{O_2} regime[14]).

On the one hand, from the electrochemical point of view, it should be noted that upon discharge, Nb^{5+} is reduced to Nb^{4+} at a potential around 1.6 V vs. Li/Li^+ . At this point, Ti^{4+} is already reduced to Ti^{3+} and in general, the reference state of Ti is always negative compared to the charge state of niobium, down to potentials of around 0.5 V, where the charge transfer of $\text{Nb}^{4+}/\text{Nb}^{3+}$ takes place[15].

At any P_{O_2} regime, it is obvious that niobium acts as a donor. Assuming that mobility of electron does not change by doping, the electronic conductivity of titania material must increase on Nb-doping according to $\sigma_e \propto [e'] \cdot \mu_e$, as TiO_2 is *n*-type conducting.

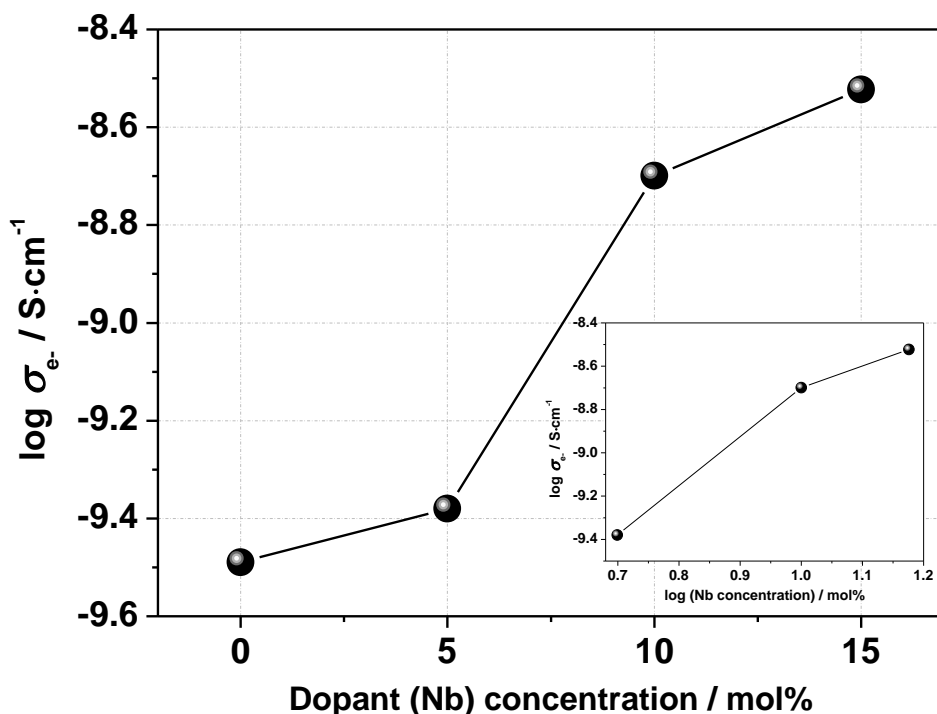


Figure 5.5: Conductivity of $mp\text{-Ti}_{1-y}\text{Nb}_y\text{O}_{2+\delta}$ nanostructures measured at 523 K as a function of dopant concentration (0 ~ 15 mol%) (inset: log-log plot).

In Figure 5.5, electronic conductivities measured at 523 K are plotted as a function of Nb concentration (0 – 15 mol%). The conductivity of 20% Nb-doped titania sample was not measured because it was not a single phase material. One can recognize from Figure 5.5 that the conductivity increased by almost one order of magnitude by Nb-doping within the solid solubility limit (15 mol%), showing the

value of $3.2 \cdot 10^{-10}$, $4.2 \cdot 10^{-10}$, $2.0 \cdot 10^{-9}$, and $3.0 \cdot 10^{-9} \text{ S}\cdot\text{cm}^{-1}$ in the presence of 0, 5, 10, and 15 mol% Nb, respectively. It should be noted that the measured conductivities can not be considered as absolute values as a relative density of measured pellets was only approximately 45 % owing to the absence of a sintering process to keep the nano-sized, anatase phase. Nevertheless, a relative comparison of conductivity values for each pellet was possible as the density of all pellets used for the measurements was almost identical.

5.2.2.3 Electrochemical Analysis: Kinetic Analysis

Electrochemical impedance spectroscopy (EIS) can verify reaction models to distinguish various bulk and interfacial properties of the system at different time scales[16-18]. The Nyquist plot of the electrochemical impedance measurements for undoped, Nb-doped mesoporous TiO_2 electrode are shown in Figure 5.6a. All impedance spectra of undoped and Nb-doped mesoporous TiO_2 comprise one depressed semicircle at high frequency range (charge transfer resistance) and extended straight line at low frequency region (Warburg response). The deviation of Warburg tails from the ideal 45 degree is explained in detail in the literature by Jamnik and Maier[19]. The semicircles at relatively high frequency range most likely arise from the resistance by charge transfer of Li^+ at the electrolyte/electrodes interface. The impedance spectra were fitted with the equivalent circuit in order to determine the charge transfer resistance. The change of the R_{ct} values as a function of dopant concentration is plotted in Figure 5.6b and summarized in Table 5.2. It can be seen that the diameters of the semicircles have a tendency to decrease with an increase of dopant concentration, which indicates Nb-doping reduces the charge transfer resistance in TiO_2 electrodes. The smaller charge transfer resistance of Nb-doped titania electrodes indicates a lower electrochemical polarization of the cells most likely resulting from the increased electronic charge carrier concentration by homogeneous *n*-type doping. The variation of the charge transfer resistance seems to saturate at high Nb-content (almost identical R_{ct} values at 15% and 20%). This is most likely because the

formation of secondary phases at high dopant concentration (over solid solubility limit, $mp\text{-Ti}_{0.85}\text{Nb}_{0.15}\text{O}_{2+\delta}$) induces additional resistance in the system.

Table 5.2. Charge transfer resistance of $mp\text{-Ti}_{1-y}\text{Nb}_y\text{O}_{2+\delta}$ electrodes determined by EIS depending on niobium concentration.

	$mp\text{-TiO}_2$	$mp\text{-Ti}_{0.95}\text{Nb}_{0.05}\text{O}_{2+\delta}$	$mp\text{-Ti}_{0.90}\text{Nb}_{0.10}\text{O}_{2+\delta}$	$mp\text{-Ti}_{0.85}\text{Nb}_{0.15}\text{O}_{2+\delta}$	$mp\text{-Ti}_{0.80}\text{Nb}_{0.20}\text{O}_{2+\delta}$
R_{ct} [Ω]	139.2	101.2	85.6	56.6	52.5

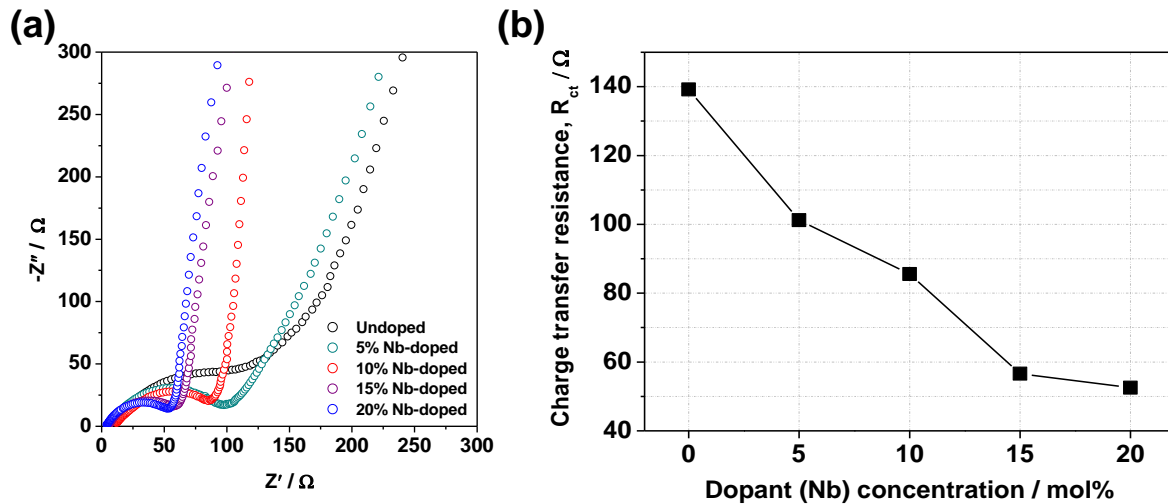


Figure 5.6: (a) Nyquist plots of undoped, Nb-doped mesoporous TiO_2 electrodes for different dopant concentration. (b) Variation of charge transfer resistance (R_{ct}) with the increase of Nb concentration.

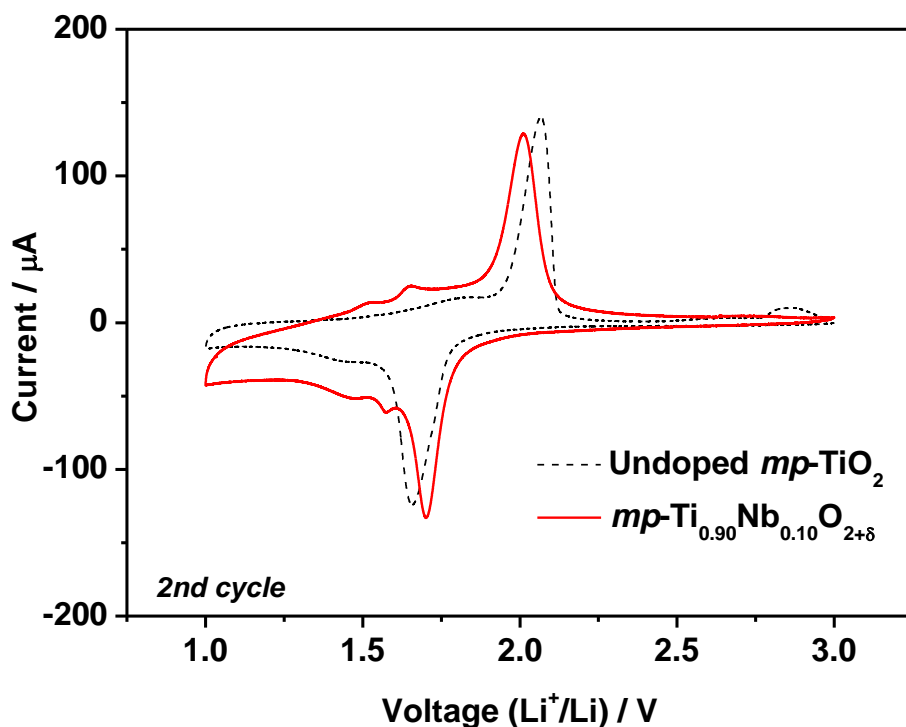
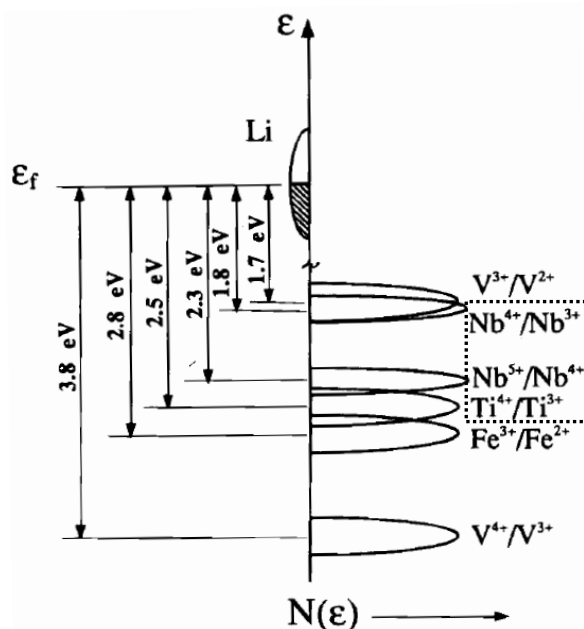


Figure 5.7: Cyclic voltammograms of undoped (dashed line) and 10 mol% Nb-doped mesoporous TiO_2 (solid line) electrodes at the scan rates of $0.1 \text{ mV} \cdot \text{s}^{-1}$ in the potential window between 3.0 and 1.0 V vs. Li^+/Li .

To investigate the electrochemical redox reactions of Li in $mp\text{-Ti}_{1-y}\text{Nb}_y\text{O}_{2+\delta}$ electrodes, cyclic voltammetry (CV) measurement was performed and is shown in Figure 5.7. The measurements were carried out in the potential window of 1.0 – 3.0 V at the scan rate of $0.1 \text{ mV} \cdot \text{s}^{-1}$. For undoped $mp\text{-TiO}_2$ (dashed line, Figure 5.7), apparent pair of reduction/oxidation (redox) peaks were observed at 1.7 V (reduction: Li-intercalation) and 2.0 V (oxidation: Li-extraction) vs. Li^+/Li , which corresponds to the valence variation of $\text{Ti}^{4+}/\text{Ti}^{3+}$. Additionally, redox shoulder peaks at $\sim 1.45 \text{ V}$ (reduction) and $\sim 1.85 \text{ V}$ (oxidation) were driven downward, that could be attributed to multi-phase transitions to Li_xTiO_2 ($x > 0.55$). The Nb-doped titania samples show redox couples in the same potential ranges but with significantly reduced current peak separation (Δi_p) due to the decreased electrode polarization resulting from the increased electronic conductivity. The Δi_p values are summarized in Table 5.3.

In addition to these two redox couples, the cyclic voltammogram curves of 10% Nb-doped TiO_2 electrode depicts another distinct pair of reduction and oxidation peaks at ~ 1.56 V (reduction) and ~ 1.64 V (oxidation), respectively.

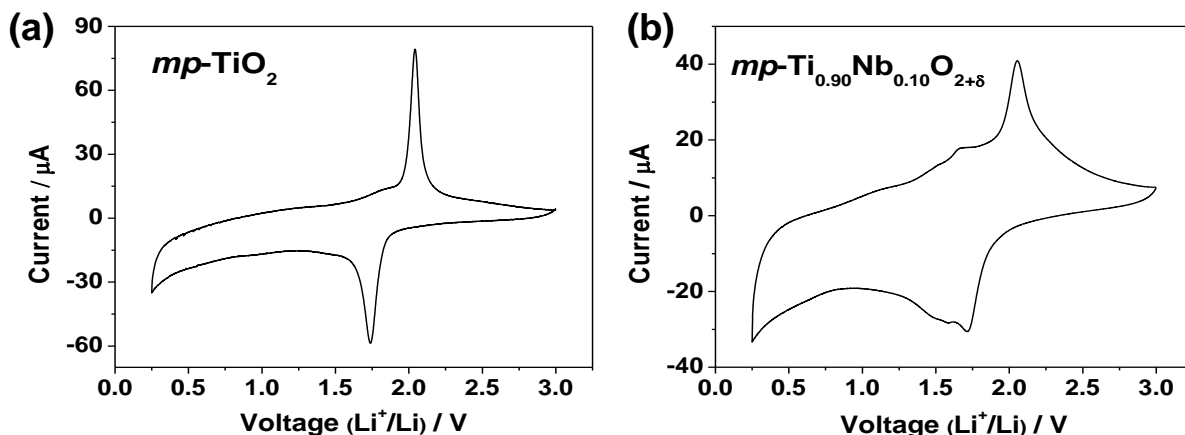


Scheme 5.2: Relative energies of redox couples in materials having NASICON framework[15]. (Please refer the information in the dotted box.)

As Padhi *et al.* reported, this redox couple at slightly lower voltage window than the ones for $\text{Ti}^{4+}/\text{Ti}^{3+}$ redox reaction most likely corresponds to reduction/oxidation of Nb ($\text{Nb}^{5+}/\text{Nb}^{4+}$)[15]. Relative energies of each redox couple are shown in Scheme 5.2. In order to investigate all possible valence variations of niobium *i.e.* $\text{Nb}^{5+}/\text{Nb}^{4+}/\text{Nb}^{3+}$, another CV measurement was carried out in a wider potential window (0.25 V - 3.0 V) at the same scan rate of $0.1 \text{ mV} \cdot \text{s}^{-1}$. While no further redox reactions were observed at voltages below 1.0 V for the pure mesoporous TiO_2 electrode, for the niobium-doped titania electrode the small bump upon oxidation was observed at ~ 1.1 V (see Figure 5.8) which is approx. 0.4 V below the voltage for the redox couple $\text{Nb}^{5+}/\text{Nb}^{4+}$ (however this is not observable in the reduction process). This small bump could correspond to the partial reduction reaction of $\text{Nb}^{4+}/\text{Nb}^{3+}$. Nonetheless, this transition reaction can be excluded from the main consideration because the operating potential window for battery cycling in the present study is limited as 1.0 – 3.0 V.

Table 5.3: The current peak separation Δi_p of $mp\text{-Ti}_{1-y}\text{Nb}_y\text{O}_{2+\delta}$ (in mV) for different dopant (Nb) concentrations at scan rate of 0.1 and 1 mVs^{-1} .

Scan rate	$mp\text{-TiO}_2$	$mp\text{-Ti}_{0.95}\text{Nb}_{0.05}\text{O}_{2+\delta}$	$mp\text{-Ti}_{0.90}\text{Nb}_{0.10}\text{O}_{2+\delta}$	$mp\text{-Ti}_{0.85}\text{Nb}_{0.15}\text{O}_{2+\delta}$
0.1 mVs^{-1}	393	320	312	286
1 mVs^{-1}	570	550	526	-

**Figure 5.8:** Comparison of cyclic voltammograms between (a) undoped and (b) 10 % Nb-doped mesoporous TiO_2 electrode in wider voltage range of 3.00 – 0.25 V at scan rate of 0.1 mVs^{-1} .

As mentioned in the previous section, the measured peak current i_p can be described by the Randles-Sevcik equation for the diffusion-controlled reversible system, and thus the effective chemical diffusion coefficient ($eff. D_{Li}^\delta$) can be determined using CV profiles. Figure 5.9 shows a variation of calculated $eff. D_{Li}^\delta$ values in the $mp\text{-Ti}_{1-y}\text{Nb}_y\text{O}_{2+\delta}$ electrodes as a function of dopant concentration. The $eff. D_{Li}^\delta$ value for $mp\text{-Ti}_{0.90}\text{Nb}_{0.10}\text{O}_{2+\delta}$ electrode during Li-insertion is $6.9 \cdot 10^{-18} \text{ cm}^2 \cdot \text{s}^{-1}$ which is higher than the value for undoped titania electrode. This implies that in addition to the decrease in R_{ct} , the increased electronic charge carrier concentration facilitates the local ambipolar $\text{Li} = \text{Li}^+ + e^-$ transport kinetics in titania electrodes. However, in spite of the higher electronic conductivity, $eff. D_{Li}^\delta$ in $mp\text{-Ti}_{0.85}\text{Nb}_{0.15}\text{O}_{2+\delta}$ electrode was found to be even smaller than that in undoped TiO_2 electrode, and thus a maximum of $eff. D_{Li}^\delta$ is observed at 10 mol% niobium concentration. Calculated $eff. D_{Li}^\delta$ values are summarized in Table 5.4.

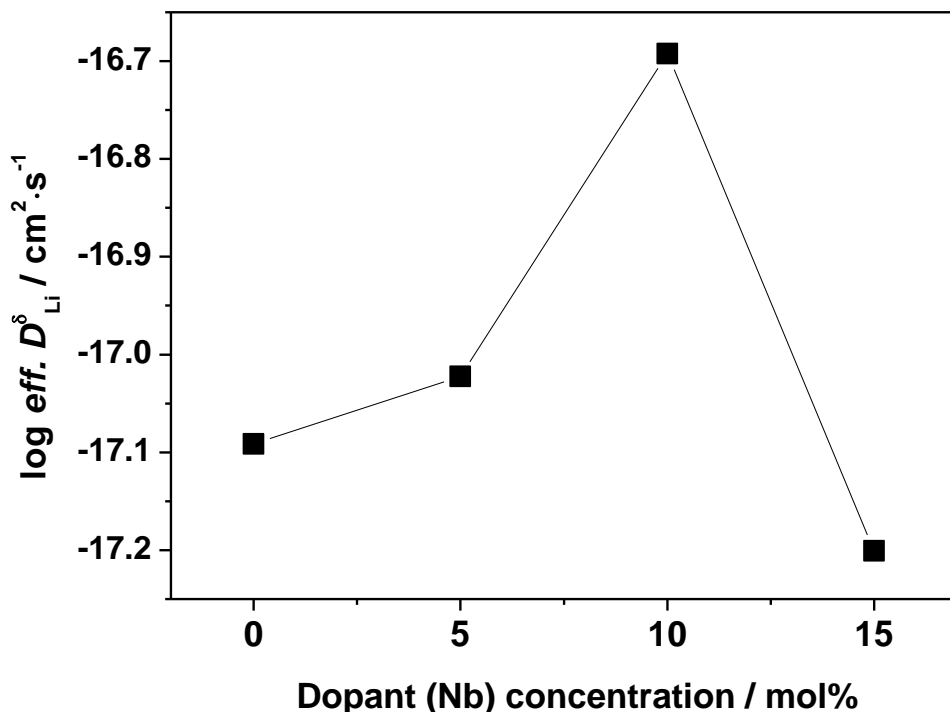


Figure 5.9: Effective chemical diffusion coefficient of Li (D_{Li}^{δ}) determined by SSCV as a function of niobium concentration.

5.2.2.4 Electrochemical Analysis: Li Storage Performance

Figure 5.10 displays galvanostatic discharge curves (at 0.2C) for $mp\text{-TiO}_2$ and $mp\text{-Ti}_{0.90}\text{Nb}_{0.10}\text{O}_{2+\delta}$. For comparison, a discharge curve for commercially available TiO_2 nano-particles ($comm\text{-TiO}_2$) having a similar crystallite size (≈ 20 nm) with that of $mp\text{-TiO}_2$ is also shown together. It clearly shows that both mesoporosity and increased electronic conductivity are beneficial to enhance Li-storage capacity of the TiO_2 electrode. The delivered Li-insertion capacities at 0.2C were 87.5, 149.6, and 200.5 $\text{mAh} \cdot \text{g}^{-1}$ for $comm\text{-TiO}_2$, $mp\text{-TiO}_2$, and $mp\text{-Ti}_{0.90}\text{Nb}_{0.10}\text{O}_{2+\delta}$, respectively. For an in-depth study on the Li-insertion mechanism into each material, the galvanostatic discharge curves are again divided into three representative regions[20]. The voltage first drops quickly from open circuit voltage to ~ 1.75 V (region A: Li intercalation into TiO_2 lattice) followed by voltage plateau corresponding to two-phase insertion of Li (region B). After leaving the voltage

plateau, another voltage slope is shown up to cut-off voltage of 1.0 V (region C). By comparing the voltage profile of *comm*-TiO₂, *mp*-TiO₂, it was found first of all that the use of mesoporous structure gives rise to two characteristics in the voltage profile; i) a large increase of capacity delivered by region B, and ii) a more distinct additional pseudo-plateau at 1.6 ~ 1.4 V.

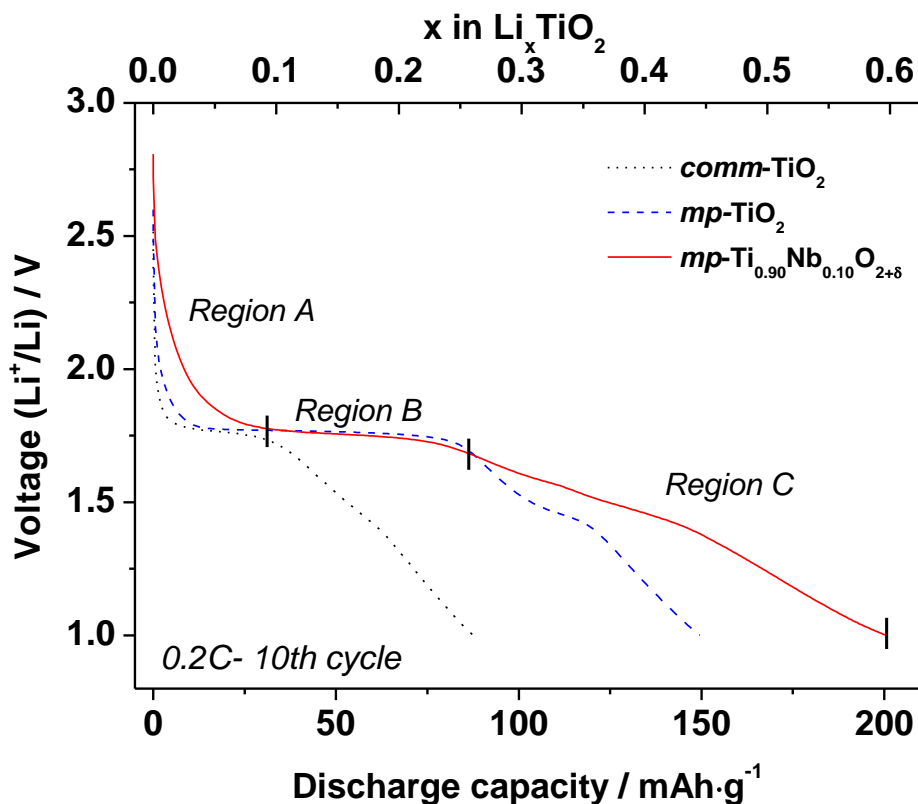


Figure 5.10: Comparison of voltage profiles *vs.* discharge (reversible) capacities for commercial (nonporous), mesoporous undoped, and mesoporous 10 mol% Nb-doped titania electrode discharged at 0.2C (20th cycle).

As discussed in Chapter 3, a primary advantage of using a porous structure is that a large interfacial region (large electrolyte/electrode contact area by the help of high porosity) significantly shorten the diffusion length of both Li⁺ and e⁻, thereby providing better electrochemical utilization because of an improved Li⁺ ion access. This enhanced transport characteristics, which allows for a larger electrochemically available volume in titania, primarily causes a significant improvement of the two-phase Li-storage reaction (region B). Compared to nanoporous TiO₂ materials described in Chapter 3, only the half of specific surface

area ($\sim 140 \text{ m}^2\text{g}^{-1}$) of the $mp\text{-TiO}_2$ here is however not sufficient to notably emphasize the interfacial storage phenomena (region C).

It has been reported that the second characteristics, the pseudo-plateau is indicative of a topotactic further intercalation of Li, which is particularly observed for small-sized particles[21,22]. Using neutron diffraction techniques, Wagemaker *et al.*[23] found that this pseudo-plateau most likely is attributed to a formation of high order tetragonal Li-titanate *e.g.* Li_1TiO_2 (space group $I4_1/amd$) which may coexist with orthorhombic lithium titanate ($\text{Li}_{0.5}\text{TiO}_2$, space group $Imma$), indicating that another two-phase reaction taking place after the main Li insertion. Hence, the clear distinction of pseudo-plateau for $mp\text{-TiO}_2$ seems to be attributed to a multi phase transition into high order Li-titanate by the aid of large Li^+ accessibility and short ambipolar $\text{Li} = \text{Li}^+ + \text{e}^-$ transport length. As shown in Figure 5.11, the storage capacity delivered at 0.2C by region B for $mp\text{-TiO}_2$ electrode (after several initial cycles) was significantly larger than that for $comm\text{-TiO}_2$. For even further cycles, $mp\text{-TiO}_2$ electrode exhibited only slight decay in the region B, while $comm\text{-TiO}_2$ showed severe decay in region B. This is because, in addition to the larger accessible Li^+ ions, a structural integrity of $mp\text{-TiO}_2$ allows for a better accommodation of structural changes upon Li insertion/extraction, thereby causing the better cycle performance. On the one hand, as it is also observable with $np\text{-TiO}_2$ samples (see Chapter 3), the large initial capacity loss of $mp\text{-TiO}_2$ electrode might be due to electrolyte decomposition reactions by the trace humidity which can be easily adsorbed in a porous structure.

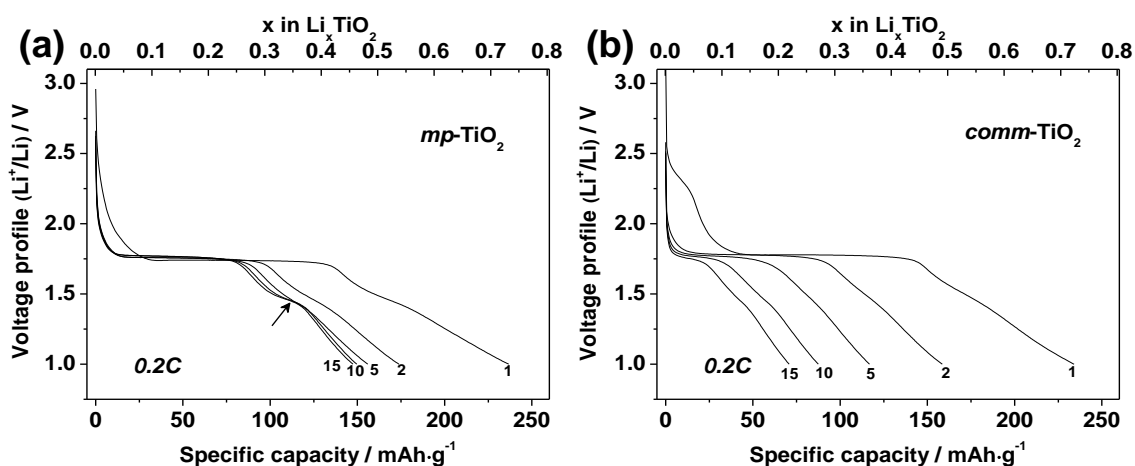


Figure 5.11: Discharge curves at 0.2C of (a) mp -TiO₂ and (b) $comm$ -TiO₂ at various cycles.

Let me then discuss about effects of niobium doping on voltage profiles upon Li-insertion. As illustrated in Figure 5.10, when compared with the undoped titania electrode, niobium doping gives rise to the predominant increases in region A and C. The negligible x (in Li_xTiO_2) by region A for undoped TiO₂ increases up to $x=0.1$ by 10 mol% Nb-doping. The increase in region A can be explained by a decreased miscibility gap resulting from the slightly smaller sized grains of Nb-doped samples. It was reported by several groups[23,24] that the phase transitions between TiO₂ and Li_xTiO_2 involves a change in enthalpy that is highly related to the particle size. If the particle size decreases, so called the miscibility gap decreases by the increasing contribution of the elastic energy penalty at the two phase boundary, which results in an extension of the single phase regions (region A or C). The increase in region C could also partly be influenced by size confinement effect, however it seems that this is more pronouncedly attributed to the additional redox reaction at lower potential range accompanying valence variation of Nb⁵⁺/Nb⁴⁺ as CV analysis indicated. The voltage profile of this redox reaction (at 1.6 ~ 1.5 V) could partially overlap with the one by the further phase transitions (representing a pseudo-plateau at 1.6 ~ 1.4 V), thereby extending sloped voltage profile after leaving a main voltage plateau at 1.75 V.

Figure 5.12 shows voltage profiles *vs.* reversible capacities depending on current densities. It is clearly exhibited that for various C rates an additional increase of

discharge capacities was achieved by 10 mol% Nb-doping, predominantly by an extension of region C without a significant change in the length of region B. Upon lithiation at 0.2C, the capacity corresponded to voltage region C represents 63.3 % of the total capacity for $mp\text{-Ti}_{0.90}\text{Nb}_{0.10}\text{O}_{2+\delta}$ electrode, while only 44.4 % for undoped $mp\text{-TiO}_2$. In addition, Nb-doped titania electrodes could sustain higher capacities even at high C rates due to an increase of electronic charge carrier concentration that plays a beneficial role in the storage of a multi particle arrangement (enhanced rate of intra- and inter-particle electron transport, shown in Figure 4.15).

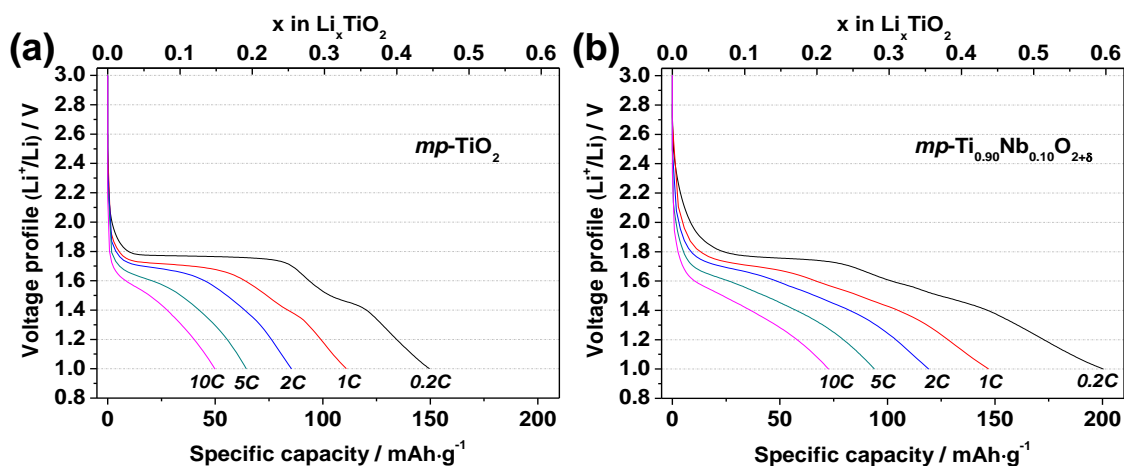


Figure 5.12: Voltage profiles vs. reversible capacities for (a) $mp\text{-TiO}_2$ and (b) $mp\text{-Ti}_{0.90}\text{Nb}_{0.10}\text{O}_{2+\delta}$ electrodes at various discharge rates (0.2C – 10C).

The electronic charge carrier concentration could be systematically varied by increased dopant concentration (0 – 15 mol%). Figure 5.13 shows galvanostatic discharge curves and a rate performance of $mp\text{-Ti}_{1-y}\text{Nb}_y\text{O}_{2+\delta}$ electrodes for different dopant concentration. As shown in Figure 5.13a, at 0.2C an improvement of electrochemical Li-storage property by Nb-doping was observed only up to 10 mol% of niobium, whereas an even smaller reversible capacity was obtained for the $mp\text{-Ti}_{0.85}\text{Nb}_{0.15}\text{O}_{2+\delta}$ electrode. Moreover, Figure 5.13b and Table 5.4 demonstrate the worse rate capability of $mp\text{-Ti}_{0.85}\text{Nb}_{0.15}\text{O}_{2+\delta}$ electrode compared to 10% Nb-doped sample. By analyzing the voltage profiles upon discharge, it was found that all the capacities delivered by regions A/B/C for $mp\text{-Ti}_{0.85}\text{Nb}_{0.15}\text{O}_{2+\delta}$ were significantly reduced. Up to 10 mol% Nb, the performed niobium doping not only enhances the ability of utilizing the theoretical bulk Li-storage capacity ($\text{Ti}^{4+}/\text{Ti}^{3+}$) due to

increased electronic carriers concentration, but also delivers an extra storage capacity by the additional redox reaction ($\text{Nb}^{5+}/\text{Nb}^{4+}$). However, similarly with the situation of oxygen-deficient titania in the previous section, too high a concentration of electrons at 15% Nb concentration is rather detrimental to overall Li-storage most likely due to the increased defect association $\text{Li}_i^* + e' \rightleftharpoons \text{Li}_i^X$ (see Chapter 4) that depletes free Li^+ carrier concentration [25–27]. As shown in Figure 5.13a, this strong trapping might cause the early onset of region C in the voltage profile of $mp\text{-Ti}_{0.85}\text{Nb}_{0.15}\text{O}_{2+\delta}$ electrode as well as decreased $eff. D_{Li}^\delta$ value compared to that for $mp\text{-Ti}_{0.90}\text{Nb}_{0.10}\text{O}_{2+\delta}$ (Figure 5.9). As a consequence, this most likely gave rise to worse overall Li-storage properties of heavily-doped (herewith 15 mol% Nb) titania electrodes. A detailed theoretical defect chemical analysis on lithium storage in $\text{Ti}_{1-y}\text{Nb}_y\text{O}_{2+\delta}$ is discussed in the next section (Chapter 5.3).

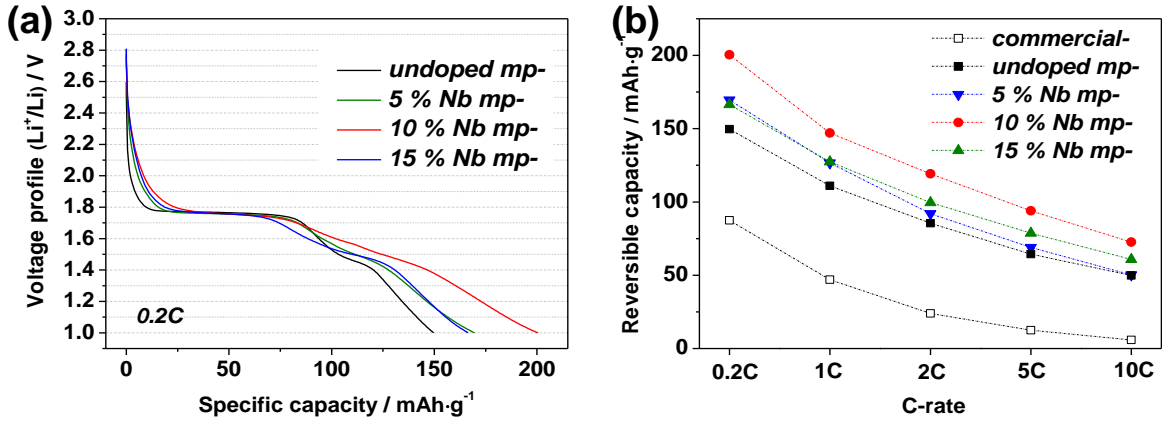


Figure 5.13: (a) Voltage profiles vs. reversible capacities for $mp\text{-Ti}_{1-y}\text{Nb}_y\text{O}_{2+\delta}$ electrodes (depending on dopant concentration during discharge) at 0.2C and (b) rate capability of the $mp\text{-Ti}_{1-y}\text{Nb}_y\text{O}_{2+\delta}$ electrodes depending on y (0.05 – 0.15).

Table 5.4: Charge transfer resistance, effective chemical diffusion coefficient of Li ($eff. D_{Li}^\delta$) and reversible discharge capacities (at 0.2C, 10C) for $mp\text{-Ti}_{1-y}\text{Nb}_y\text{O}_{2+\delta}$ electrodes.

	$mp\text{-TiO}_2$	$mp\text{-Ti}_{0.95}\text{Nb}_{0.05}\text{O}_{2+\delta}$	$mp\text{-Ti}_{0.90}\text{Nb}_{0.10}\text{O}_{2+\delta}$	$mp\text{-Ti}_{0.85}\text{Nb}_{0.15}\text{O}_{2+\delta}$
R_{ct} [Ω]	139	101	86	57
$eff. D_{Li}^\delta$ [$\text{cm}^2 \cdot \text{s}^{-1}$]	$8.1 \cdot 10^{-18}$	$9.5 \cdot 10^{-18}$	$2.0 \cdot 10^{-17}$	$6.3 \cdot 10^{-18}$
Reversible capacity (0.2C) [$\text{mAh} \cdot \text{g}^{-1}$]	145	164	196	158
Reversible capacity (10C) [$\text{mAh} \cdot \text{g}^{-1}$]	49	50	73	61

5.3 Theoretical Analysis– Brouwer Diagrams

5.3.1 Study on Defect Concentration

In this section, for an in-depth investigation of the experimentally observed phenomena in terms of Li transport and storage, the point defect chemistry of lithium storage in the $\text{Ti}_{1-y}\text{Nb}_y\text{O}_{2+\delta}$ electrode material is discussed. The main difference to the defect chemical analysis with frozen-in native defects (see Chapter 4.4.1) is that $\text{Nb}_{\text{Ti}}^\bullet$ instead of oxygen vacancies ($V_{\text{O}}^{k\bullet}$) is considered as a predominant type of introduced defect. It is assumed that the contributions of native defects (*i.e.* oxygen vacancies and titanium defects) are small compared to niobium doping and Li content. At room temperature again ion-electron associations between Li^+ and e^- as well as between Nb^{5+} and e^- have to be reckoned with according to $\text{Li}_i^\bullet + e' \rightleftharpoons \text{Li}_i^X$ and $\text{Nb}_{\text{Ti}}^\bullet + e' \rightleftharpoons \text{Nb}_{\text{Ti}}^X$. Then the exponents M'_j , N'_j , and γ' introduced in Eq (4.4-2) can be determined from the following mass action laws and balance equations.

$$x = [\text{Li}_i^\bullet] + [\text{Li}_i^X] \quad (\text{Li stoichiometry}) \quad (5.3-1)$$

$$C = [\text{Nb}_{\text{Ti}}^\bullet] + [\text{Nb}_{\text{Ti}}^X] \quad (\text{total dopant concentration}) \quad (5.3-2)$$

$$[e'] = [\text{Nb}_{\text{Ti}}^\bullet] + [\text{Li}_i^\bullet] \quad (\text{electroneutrality}) \quad (5.3-3)$$

$$[\text{Nb}_{\text{Ti}}^\bullet][e'] = K_1[\text{Nb}_{\text{Ti}}^X] \quad (\text{trapping of } e' \text{ by } \text{Nb}_{\text{Ti}}^\bullet) \quad (5.3-4)$$

$$[\text{Li}_i^\bullet][e'] = K_2[\text{Li}_i^X] \quad (\text{trapping of } e' \text{ by } \text{Li}_i^\bullet) \quad (5.3-5)$$

Figures 5.14–5.16 show Brouwer diagrams $\log [\text{defect}]$ vs. \log (lithium content x) or \log (lithium activity a_{Li}) (Figure 5.14 and 5.15) and \log (total dopant concentration C) (Figure 5.16) derived from the above mass balance equations. As I assume only one type of charged extrinsic defects (*i.e.* $\text{Nb}_{\text{Ti}}^\bullet$) to dominate, Brouwer diagrams seem to be rather simple compared to those shown in Figures 4.19–4.21 in which multiple charge state of oxygen vacancies ($V_{\text{O}}^{k\bullet}$, $k = 0, 1, 2$) are considered.

Figures 5.14–5.15 show the variation of defect concentration with x and a_{Li} as variables (at constant Nb concentration in this case) in lithiated Nb-doped TiO_2 ($\text{Li}_x\text{Ti}_{1-y}\text{Nb}_y\text{O}_{2+\delta}$). At a first glance, one can easily observe the same two phenomena

as in the previous study. First, Brouwer diagrams depend significantly on the choice of initial Li^+/e^- association condition. Even though the present case seems to have less impact on the qualitative picture of defect diagram compared to the case with oxygen-deficient titania electrode (due to single charge variation of the extrinsic dopant), it is obvious that the choice of the ratio of $[\text{Li}_i^\bullet]/[\text{Li}_i^X]$ at initial condition (left hand side of values in the abscissa) still yields different variation of overall defect concentration upon Li insertion. The second important information is that on increased lithium content x , the concentration of both charge carriers Li_i^\bullet and e' increase but eventually cannot be as steep as for Li_i^X at high lithium content (x). On the one hand, the change of variable from x into a_{Li} influences the defect diagram only for the case of weak (intermediate) initial ionic/electronic association condition (Figure 5.15), otherwise there is no significant impact for the case of the strong association condition according to $x = [\text{Li}_i^X] \propto a_{\text{Li}}$.

Now let me discuss features with the defect diagrams depending on the extrinsic dopant concentration (at fixed lithium content x) that is illustrated in Figure 5.16. If there is initially no ion-electron association reaction, the concentration of Li_i^\bullet is essentially constant in the overall range of the total dopant concentration (C), while at high doping level, Nb_{Ti}^\bullet proportionally increases with the increase of total dopant (Nb) concentration followed by a slight decrease of slope at very high dopant concentration due to the increased concentration of Nb_{Ti}^X . Therefore, three representative regimes (yellow/green/blue regime) are given. On the other hand, as far as weak (intermediate) initial association $\text{Li}_i^\bullet + \text{e}' \rightleftharpoons \text{Li}_i^X$ (Figure 5.16b) is concerned, one additional regime (illustrated as violet regime) should be considered in defect diagrams. One recognizes that on increased total Nb concentration, whereas electron concentration increases, the free lithium carrier concentration Li_i^\bullet decreases due to increased ion-electron association *i.e.* trapping reaction. Depending on the degree of initial association condition (the ratio of $\text{Li}_i^\bullet / \text{Li}_i^X$ at left hand side of abscissa), quite different variations of defect concentration with the increase of dopant concentration (y-axis) are shown. This indicates a great

importance of association among charged defects for Li-storage ability of electrode materials.

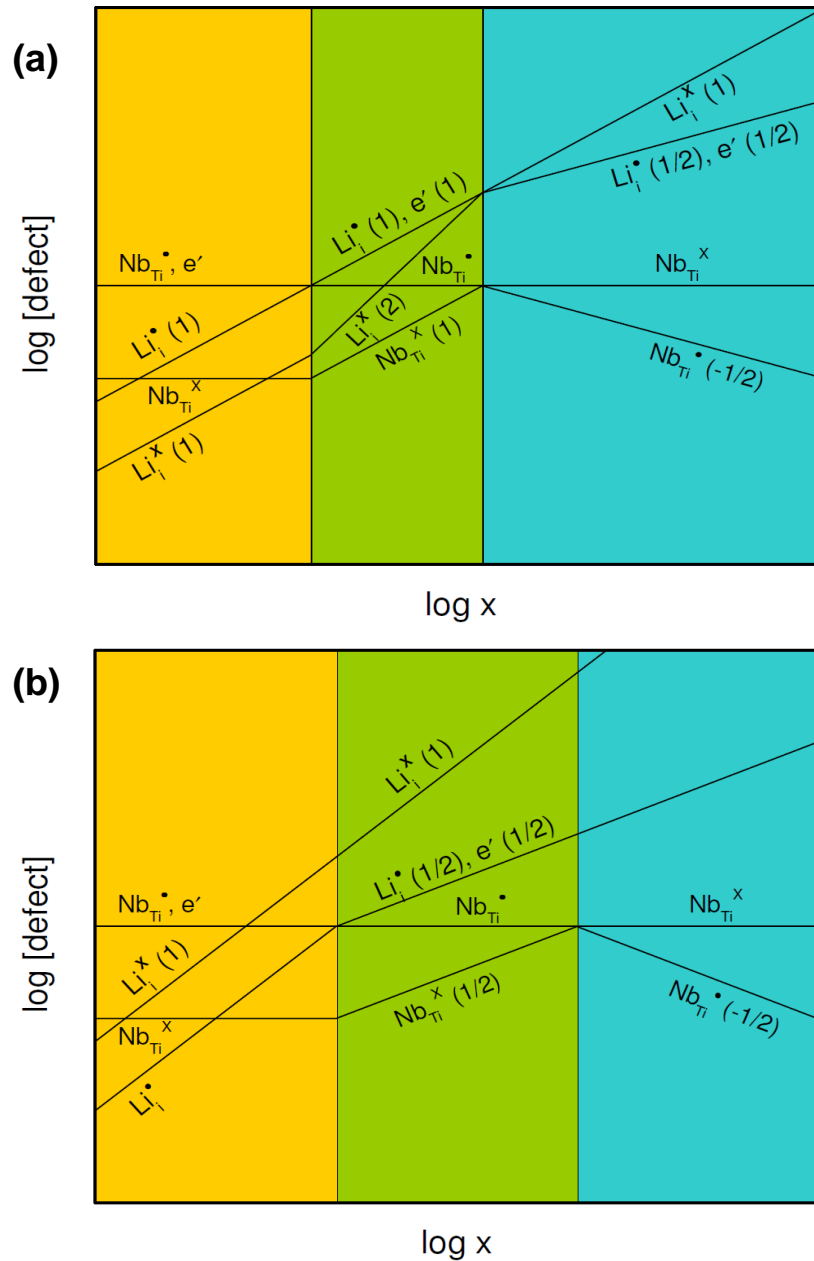


Figure 5.14: Dependence of defect concentration upon lithium insertion (depending on x) in $\text{Li}_x\text{Ti}_{1-y}\text{Nb}_y\text{O}_{2+\delta}$ (with a constant dopant concentration y) for the initial situation of (a) weak (intermediate) and (b) strong Li^+/e^- association $\text{Li}_i^\bullet + \text{e}' \rightleftharpoons \text{Li}_i^x$.

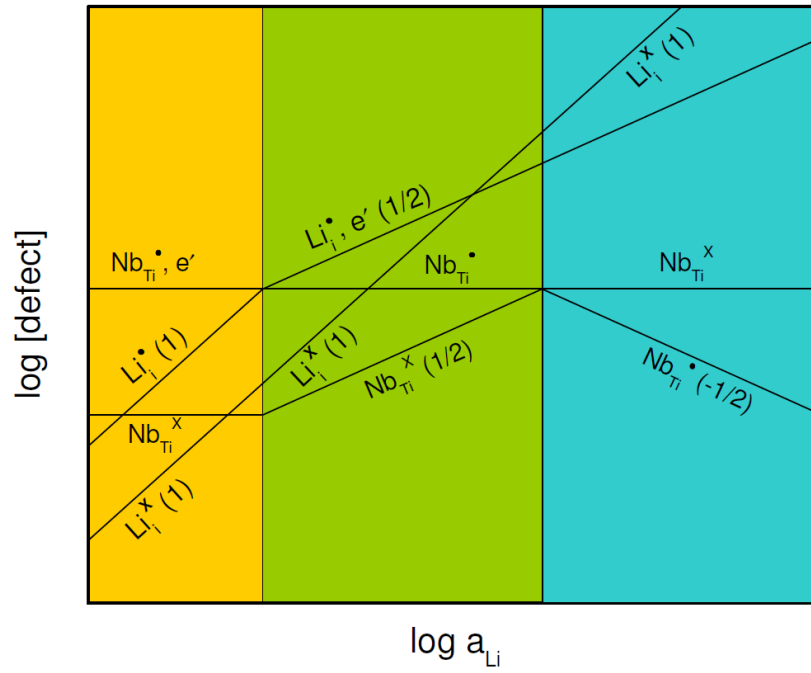


Figure 5.15: Variation in defect concentration in $\text{Li}_x\text{Ti}_{1-y}\text{Nb}_y\text{O}_{2+\delta}$ (with a constant dopant concentration y) as a function of lithium activity a_{Li} for an initial situation of weak (intermediate) Li^+/e^- association.

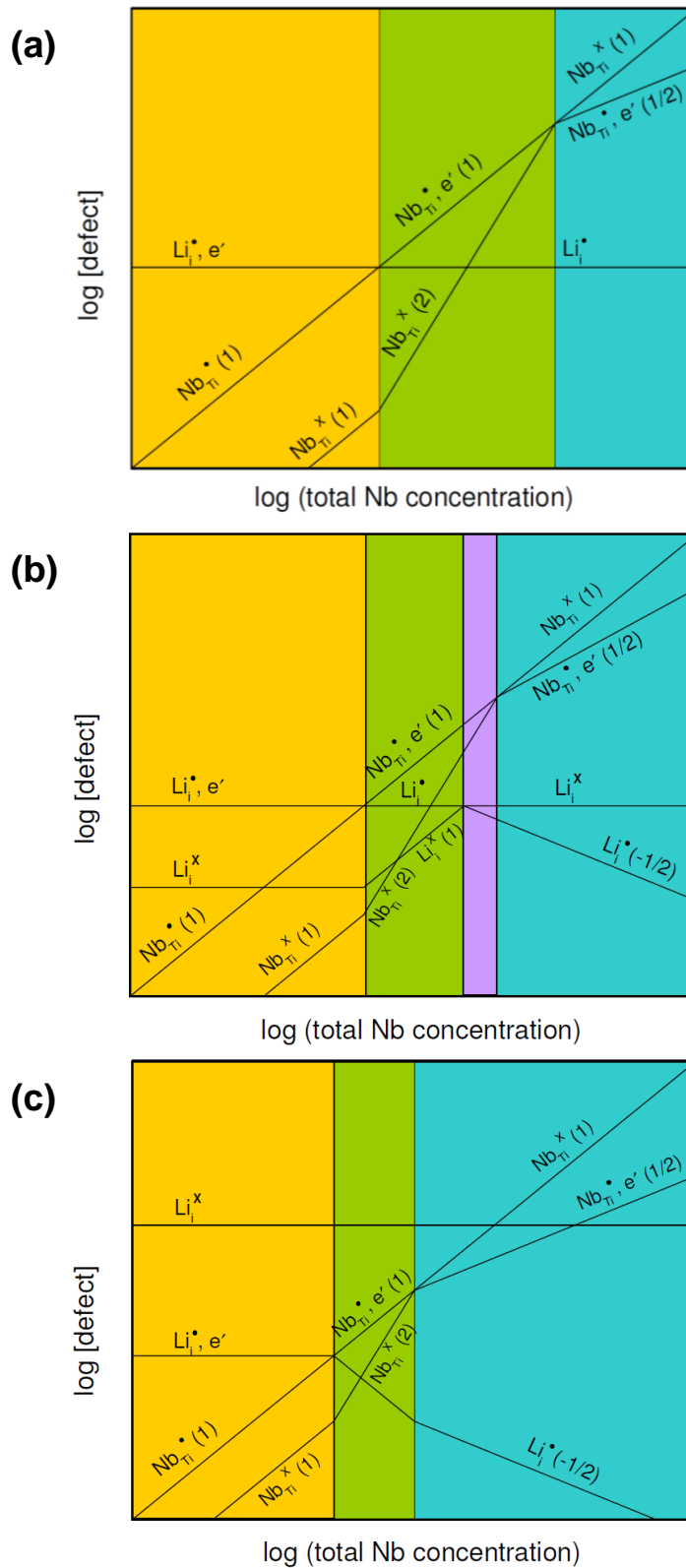


Figure 5.16: Defect concentration as a function of total dopant (Nb) concentration for different initial conditions of the Li^+/e^- association $Li_i^\bullet + e^- \rightleftharpoons Li_i^{\times}$: (a) negligible, (b) weak (intermediate) and (c) strong association.

5.3.2 Study on Lithium Diffusivity

To discuss effects of charge carriers concentration (mainly electronic carriers introduced by Nb-doping) on the chemical lithium diffusivity (D_{Li}^δ), let me start with the general equation given by the ambipolar conductivity (σ_{Li}^δ) term with trapping factors $\chi_{e'}$ and $\chi_{Li_i^\bullet}$ according to the Eq (4.4-10). For the present study, the electroneutrality equation can be written as $[e'] = [Nb_{Ti}^\bullet] + [Li_i^\bullet]$. Figure 5.17 shows a variation of D_{Li}^δ with the increase of total dopant concentration under different initial ion-electron association $Li_i^\bullet + e' \rightleftharpoons Li_i^X$ conditions. One can easily recognize at a first glance that the calculation results in almost identical D_{Li}^δ situation with the case study of lithium storage for oxygen-deficient $TiO_{2-\delta}$ electrode (see Chapter 4.4.2).

The cases with negligible and strong initial association conditions are rather simple. If there is initially no trapping between Li^+ and e^- ($x \approx [Li_i^\bullet]$), one can get relations of the types $D_{Li}^\delta \propto 2\sigma_{Li_i^\bullet} x^{-1}$ (if $u_{e'} \gg u_{Li_i^\bullet}$) and $D_{Li}^\delta \propto 2\sigma_{e'} x^{-1}$ (if $u_{e'} \ll u_{Li_i^\bullet}$) for the yellow regime in Figure 5.16a because σ_{Li}^δ is governed by the least conductive species. Therefore, D_{Li}^δ is constant with the increase of the total dopant concentration in this regime, regardless of mobility situations as summarized in Figure 5.17a. The same situation is expected even for the case with the initially strong association condition ($[Li_i^X] \gg [Li_i^\bullet] \approx [e']$, regime I in Figure 5.17c). At higher doping level where electron concentration exceeds Li^+ concentration (regime II), the mobility ratios govern the tendency of D_{Li}^δ variation as a function of dopant concentration. For negligible initial association, if $u_{e'} \ll u_{Li_i^\bullet}$, the calculation yields the relation $D_{Li}^\delta \propto \sigma_{e'} x^{-1}$, and thus a proportional increase of lithium diffusivity is anticipated in regime II (Figure 5.17a top) because of the increase of electron concentration with the increase of total Nb concentration (see Figure 5.16a). On the other hand, if the mobility of electron exceeds that of Li^+ , a constant relation of D_{Li}^δ as a function of

dopant concentration is anticipated according to $D_{Li}^{\delta} \propto \sigma_{Li} x^{-1}$ (Figure 5.17a, regime II down).

The defect concentration situation for the green regime in Figure 5.16b ($[e'] > [Li_i^{\bullet}] > [Li_i^X]$) is converted into D_{Li}^{δ} and shown in Figure 5.17b (regime II). Although the onset point is somehow different according to mobility ratios, the same monotonic decrease of D_{Li}^{δ} with the increase of Nb concentration is shown. At very high Nb doping level ($[e'] \gg [Li_i^X] > [Li_i^{\bullet}]$, see the blue regime in Figure 5.16b), the analysis suggests again a constant D_{Li}^{δ} as a function of Nb concentration regardless of mobility term. This is illustrated in Figure 5.17b (regime III).

If a high doping level situation with the initially strong association ($x = [Li_i^X]$) is converted to Li diffusivity, I get a relation $D_{Li}^{\delta} \propto \sigma_{Li} x^{-1}$. Again mobility determines D_{Li}^{δ} in which, if the mobility of Li^+ exceeds $u_{e'}$, D_{Li}^{δ} shows a maximum at certain Nb concentration followed by monotonic decrease at higher Nb doping level (Figure 5.17c regime II top). Indeed, this tendency of showing a maximum is observed in our experimental results of Li diffusivity as well as storage capacity (see Chapter 5.2). For such an unusual mobility situation one can again refer to the literature[28]. If the mobility of electron exceeds that of Li^+ , a monotonic decrease of diffusivity is anticipated with the increase of doping level (Figure 5.17c regime II down). In this case, the experimentally observed maximum in Li storage and transport as a function of dopant concentration can be explained by a counterplay of D_{Li}^{δ} decrease and increased rate of interparticle electron transport which is described by Figure 4.15. Hence both cases may be relevant for the experimentally observed tendency. On the other hand, the maximum in storage experiment of Nb-doped titania might be also attributed to a change of mobility by structural variation at high concentration of Nb.

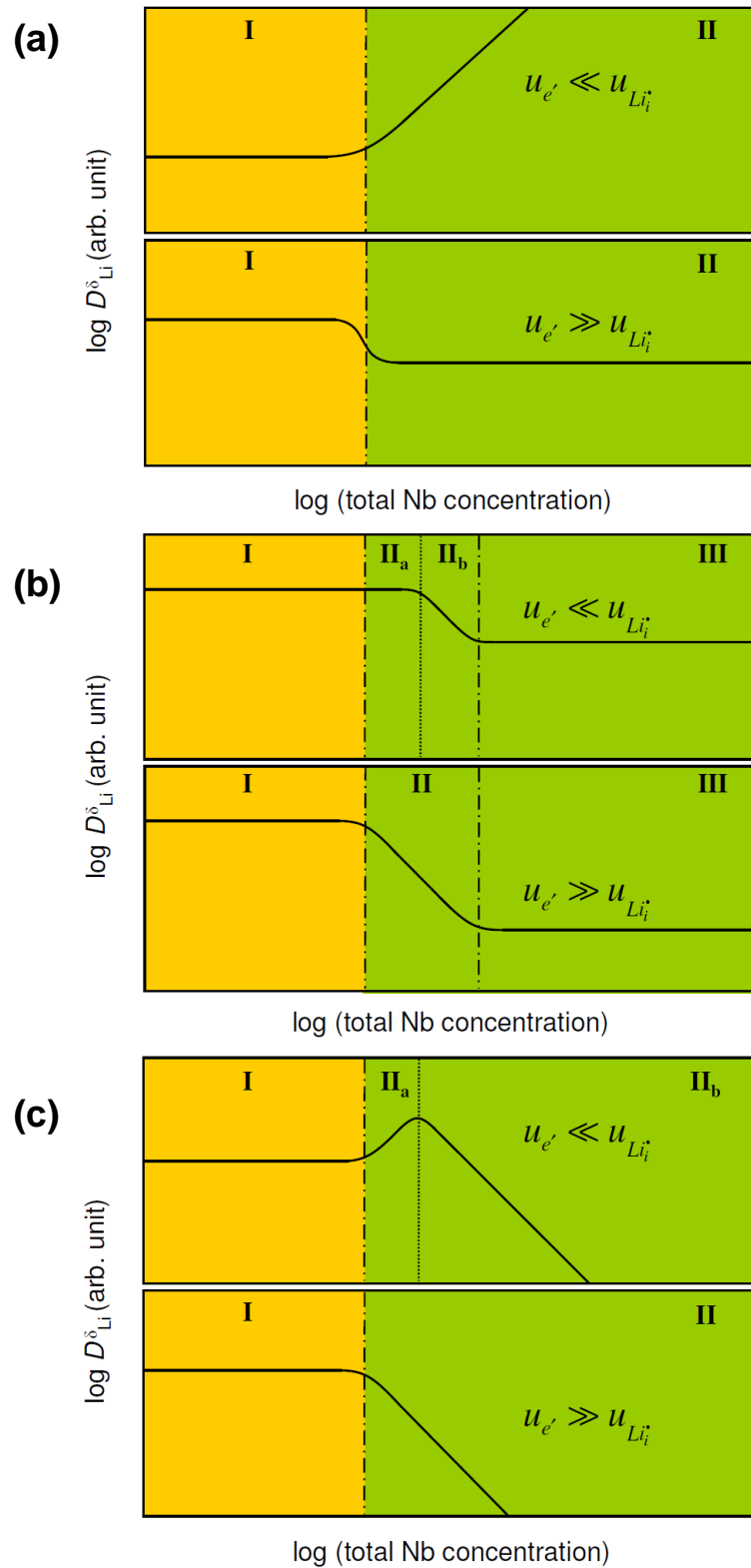


Figure 5.17: Variation of chemical diffusion coefficient of Li in $\text{Li}_x\text{Ti}_{1-y}\text{Nb}_y\text{O}_{2+\delta}$ depending on the dopant (Nb) concentration for different initial conditions of the Li^+/e^- association $\text{Li}_i^* + \text{e}' \rightleftharpoons \text{Li}_i^X$: (a) negligible, (b) weak (intermediate) and (c) strong. Unlike the concentration diagrams, the realistic smoothening at the transition is indicated.

5.4 Conclusion

In this Chapter, another approach to investigate effects of charge carriers concentrations in titania electrode was applied by using extrinsic defects (Nb-doping) and its impact on Li storage and transport was discussed. In Chapter 5.2, mesoporous niobium-doped anatase TiO_2 ($mp\text{-Ti}_{1-y}\text{Nb}_y\text{O}_{2+\delta}$) nanostructures were successfully prepared by sol-gel preparation method with a variation of dopant concentration within a solid solubility limit (y from 0.05 to 0.2). The synthesized nanostructures showed a grain size of around 20 nm with a narrow distribution of nano-sized pores. Both mesoporosity and Nb-doping were found to be very effective approaches to enhance electrochemical Li storage performance of TiO_2 electrodes. From electrochemical analyses, I demonstrate that the use of mesoporous structure efficiently enhanced the transport kinetics of titania electrode owing to a significantly shortened transport length mainly for Li^+ . On the other hand, an additionally increased electronic charge carrier concentration (together with the additional redox couple $\text{Nb}^{5+}/\text{Nb}^{4+}$) by Nb-doping could deliver extra storage capacities due to an increased rate of transport of the electrons within/through the active particles (increase of chemical complexity). The optimum doping level for Nb-doped TiO_2 is around 10 mol% above which— in spite of the higher electron concentration— Nb-doping rather deteriorates overall lithium transport and storage performance owing to an increased free Li^+ ion trapping by ion-electron association $\text{Li}_i^\bullet + e' \rightleftharpoons \text{Li}_i^x$ effect. The significantly increased electron transport length caused by the increased morphological complexity in mesoporous structure (as electron is supposed to transport through agglomerated nano-sized particles between numerous pores) might explain the fairly larger optimum dopant (Nb) concentration for Li storage (10 mol%) compared to the previous case study with oxygen-deficient (non-porous) $\text{TiO}_{2-\delta}$ nanoparticles (oxygen vacancy concentration in thousand ppm level). Some details on this feature are discussed in Chapter 6.

In Chapter 5.3, using mass action laws and balance equations detailed defect chemical analyses were carried out depending on several variables such as lithium content or activity and dopant concentration and it showed consistent result with

the storage experiment and hence confirmed the claim described in the previous case study using frozen native defects that ionic-electronic defects associations *e.g.* $Li_i^\bullet + e' \rightleftharpoons Li_i^x$ play a very important role in determining Li-storage and transport characteristics in titania electrode systems. Therefore, I would like to again emphasize the importance of well-balanced Li^+/e^- transport to overall Li storage properties. As a consequence, a careful consideration of a comprehensive interaction among charge carriers in oxide electrode materials is necessary when applied to Li-batteries.

References

- [1] S.Y. Chung, J.T. Bloking, Y.M. Chiang, *Nature Mater.* **2002**, *1*, 123.
- [2] P.S. Herle, B. Ellis, N. Coombs, L.F. Nazar, *Nature Mater.* **2004**, *3*, 147.
- [3] J. Ma, C. Wang, S. Wroblewski, *J. Power Sources* **2007**, *164*, 849.
- [4] Y. Wang, B.M. Smarsly, I. Djerd, *Chem. Mater.* **2010**, *22*, 6624.
- [5] J. Maier, *Physical Chemistry of Ionic Materials: Ions and Electrons in Solids*, John Wiley & Sons, Chichester, **2004**.
- [6] A.R. Denton, N.W. Ashcroft, *Phys. Rev. A* **1991**, *43*, 3161.
- [7] A.L. Bowman, T.C. Wallace, J.L. Yarnell, R.G. Wenzel, *Acta Cryst.* **1966**, *21*, 843.
- [8] N.G. Eror, *J. Solid State Chem.* **1981**, *38*, 281.
- [9] M. Hirano, K. Matsushima, *J. Nanosci. Nanotechnol.* **2006**, *6*, 762.
- [10] R.K. Sharma, M.C. Bhatnagar, *Sens. Actuators B* **1999**, *56*, 215.
- [11] Y. Yamamoto, H. Hayashi, T. Sekino, T. Nakayama, H. Kondo, M. Wada, T. Adachi, K. Niihara, *Mat. Res. Innovat.* **2003**, *7*, 74.
- [12] L.E. Depero, L. Sangaletti, B. Allieri, E. Bontempi, A. Marino, M. Zocchi, *J. Crys. Growth* **1999**, *198*, 516.
- [13] L.R. Sheppard, T. Bak, J. Nowotny, *J. Phys. Chem. B* **2006**, *110*, 22447.
- [14] L.R. Sheppard, Ph.D. thesis: Defect Chemistry and Charge Transport in Niobium-doped Titanium Dioxide, **2007**, University of New South Wales.
- [15] A.K. Padhi, K.S. Nanjundaswamy, C. Masquelier, J.B. Goodenough, *J. Electrochem. Soc.* **1997**, *144*, 2581.
- [16] D. Aurbach, M.D. Levi, E. Levi, H. Teller, B. Markovsky, G. Salitra, *J. Electrochem. Soc.* **1998**, *145*, 3024.
- [17] M.D. Levi, G. Salitra, B. Markovsky, H. Teller, D. Aurbach, U. Heider, L. Heider, *J. Electrochem. Soc.* **1999**, *146*, 1279.
- [18] M. Takahashi, S. Tobishima, K. Takei, Y. Sakurai, *Solid State Ionics* **2002**, *148*, 283.
- [19] J. Jamnik, J. Maier, *J. Electrochem. Soc.* **1999**, *146*, 4183.
- [20] J.-Y. Shin, D. Samuelis, J. Maier, *Adv. Funct. Mater.* **2011**, *21*, 3464.

- [21] U. Lafont, D. Carta, G. Mountjoy, A.V. Chadwick, E.M. Kelder, *J. Phys. Chem. C* **2010**, *114*, 1372.
- [22] G. Sudant, E. Baudrin, D. Larcher, J.-M. Tarascon, *J. Mater. Chem.* **2005**, *15*, 1263.
- [23] M. Wagemaker, W.J.H. Borghols, F.M. Mulder, *J. Am. Chem. Soc.* **2007**, *129*, 4323.
- [24] G. Kobayashi, S. Nishimura, M. Park, R. Kanno, M. Yashima, T. Ida, A. Yamada, *Adv. Funct. Mater.* **2009**, *19*, 395.
- [25] C.L. Olson, J. Nelson, M.S. Islam, *J. Phys. Chem. B* **2006**, *110*, 9995.
- [26] J.-Y. Shin, J.H. Joo, D. Samuelis, J. Maier, *Chem. Mater.* **2012**, *24*, 543.
- [27] J.-Y. Shin, D. Samuelis, J. Maier, *Solid State Ionics*, in press, DOI:10.1016/j.ssi.2011.12.003.
- [28] M.L. Sushko, K.M. Rosso, J. Liu, *J. Phys. Chem. C* **2010**, *114*, 20277.

6

Conclusions and Outlook

The present thesis deals with developing high performance titania electrodes for Li-batteries, but also with advancing a fundamental understanding of how ionic and electronic charge carriers influence overall lithium storage and transport properties. Titanium dioxide (anatase) has been used as a model since this material has been considered as promising for anode applications in Li-batteries. As the rate-determining step for electrode reaction is usually solid state diffusion of lithium, reaction kinetics plays a significant role. Hence the strategies to design high performance electrode materials used in the present thesis were based on a simple equation of the diffusion relaxation time $\tau_{\text{eq}} \propto L^2 / \tilde{D}$, where L is diffusion length and \tilde{D} is chemical diffusion coefficient of lithium. To manipulate each parameter (*i.e.* to shorten L and/or to increase \tilde{D}), the concepts of nano-structuring and homogeneous doping were applied. These two different strategies essentially allow for relevant adjusting screws to alter overall Li transport and storage properties either by increasing morphological (L) or chemical (\tilde{D}) complexity.

In the first part of the thesis (Chapter 3), mainly size and morphology effects of titania on Li storage were studied. A use of hierarchical nanoporous titania with very high surface area gave rise to short transport length L predominantly for Li^+ ion in the given material. It turned out that this nano-structuring is essentially beneficial to achieve high Li storage capacities due to the enhanced transport

kinetics by the significantly shortened diffusion length that ultimately allows for the better electrochemical utilization. Another interesting finding from this study is that introducing hierarchical porosity gives rise to large interfacial area contacting with the electrolyte, and in such a condition the interfacial Li storage contribution is no longer negligible compared to bulk Li storage contribution. I further investigated the nature of the interfacial Li storage mechanism. It was found that at high rates, compared to the sluggish bulk transition, Li^+ is predominantly stored in the interfacial regions because bulk transport is not able to keep up with the applied galvanostatic current. Therefore, a continuous cycling of the materials enables Li^+ ions being remained at the interfaces, resulting in very little bulk degradation* and giving high and sustainable Li storage even under high current densities.

In the latter half of the thesis (Chapters 4 and 5), the variation of charge carrier concentrations on Li storage and transport were systematically studied. Two different approaches were applied to introduce excess electronic charge carriers (for charge compensation); i) formation of frozen-in native defects (oxygen vacancies, $V_o^{k\bullet}$) and ii) homogeneous doping with extrinsic defects (substitution of Nb^{5+} on Ti^{4+} site, Nb_{Ti}^*). These two methods did not alter the microstructure of the material, but only gave rise to varying concentrations of charge compensating electrons. Because electrochemical Li storage properties of TiO_2 are mainly limited by poor intrinsic electronic conductivity of the material, the increase of electronic charge carrier concentration by these two strategies could contribute greatly to the overall Li storage and transport properties *e.g.* capacity and rate capability. However, Li storage abilities were not proportionally enhanced with the increase of electronic charge carriers. This is most likely due to the impact of ionic-electronic defect association reactions *e.g.* $\text{Li}_i^\bullet + e' \rightleftharpoons \text{Li}_i^X$, $V_o^{\bullet\bullet} + 2e' \rightleftharpoons V_o^\bullet + e' \rightleftharpoons V_o^X$ and $\text{Nb}_{\text{Ti}}^\bullet + e' \rightleftharpoons \text{Nb}_{\text{Ti}}^X$ on Li transport and storage. Among these defect associations, $\text{Li}_i^\bullet + e' \rightleftharpoons \text{Li}_i^X$ is particularly important to Li storage, because it leads to inverse

* From theoretical studies[1], it was shown that lithium diffusivity decreases by approx. 6 orders crossing the tetragonal/orthorhombic boundary (see chapter 1.3).

effects as far as $[e']$ and $[Li_i^*]$ (*i.e.* $[e'] \propto [Li_i^*]^{-1}$) are concerned. Multiple electrochemical techniques have proven that storage capacity as well as the effective Li diffusion coefficient have optimum values (showing maximum) at certain frozen-in native or extrinsic defect concentrations ($V_o^{k*} \approx 2350$ ppm and $Nb_{Ti}^* \approx 10$ mol%). This indicates that using frozen-in native defects (V_o^{k*}) is more efficient way to enhance Li storage ability as this method needs much smaller dopant concentration compared to the homogeneous doping by extrinsic defects (Nb_{Ti}^*). The detailed theoretical defect chemical analyses have led to a consistent and coherent description of the importance of ionic-electronic defect associations in Li-battery applications. The variation of not only defect concentration but also lithium diffusivity (since lithium diffusivity is given by the ambipolar Li conductivity and an ambipolar concentration term that is determined by the carrier concentrations) as a function of several variables such as lithium content or activity and frozen-in native or extrinsic dopant concentration was determined using mass action laws and balance equations. It turned out that the choice of initial association strength $Li_i^* + e' \rightleftharpoons Li_i^X$ condition (negligible or weak or strong), *i.e.* the initial $[Li_i^*]/[Li_i^X]$ ratios yields quite different situations for not only defect concentration but also lithium diffusivity. For both cases with frozen-in native and extrinsic defects, calculated lithium diffusivity as a function of dopant concentrations exhibited a maximum which is consistent with storage experiment, provided the lithium ion mobility is larger than that of electron. The alternative, namely mobility of electron which is larger than that Li^+ , the experimentally observed phenomena (maxima in effective chemical Li diffusion coefficient and storage capacity) can be explained by a counterplay of the decrease of lithium diffusivity and increased rate of interparticle electron transport. In the case of Nb-doping also effects on the mobilities have to be considered. A decision between these options is not yet possible. At any rate, the ionic-electronic association is highly important for overall Li-storage properties.

As summarized above, two different case studies with frozen-in native (Chapter 4) and extrinsic (Chapter 5) defects showed the same qualitative feature of Li storage,

namely that maximum values of chemical lithium diffusivity and storage capacity as a function of dopant concentration exist. However, the determined optimum dopant concentration for each case is very different; thousand ppm level for oxygen vacancies *vs.* 10 mol% for niobium. This large concentration difference is most likely due to the significantly different electron transport length in two systems which might be induced by morphological diversity. Figure 6.1 illustrates a simplified schematic view of electron transport length in non-porous (Figure 6.1a, situation for Chapter 4) and meso-porous (Figure 6.1b, situation for Chapter 5) TiO₂ electrode. In the case of the non-porous system, almost every single titania particles is supposed to be attached to carbon species (added during electrode preparation as conductive additive) and hence the electron transport length towards an efficient electron distribution network formed by the percolating carbon is rather short. On the other hand, in meso-porous TiO₂, the carbon additives seem to be attached to agglomerated, bigger particles rather than to single titania particles. In such a case, electron should first travel a long way within the electroactive particles before it meets carbon species, while the Li⁺ stemming from the electrolyte may still penetrate. Therefore, on a global scale, the electron transport length in meso-porous electrode system is significantly larger than that in the non-porous structure due to the increased morphological complexity that requires a much larger optimum dopant concentration (*i.e.* electron concentration). In short, the study has shown the significance of “balanced ionic/electronic charge carrier transport” for overall Li-storage properties. Therefore a comprehensive consideration of charge carriers on the level of point defect chemistry is ultimately needed in strategically designing high performance electrode materials for Li-batteries in which multiple charge carriers exist together.

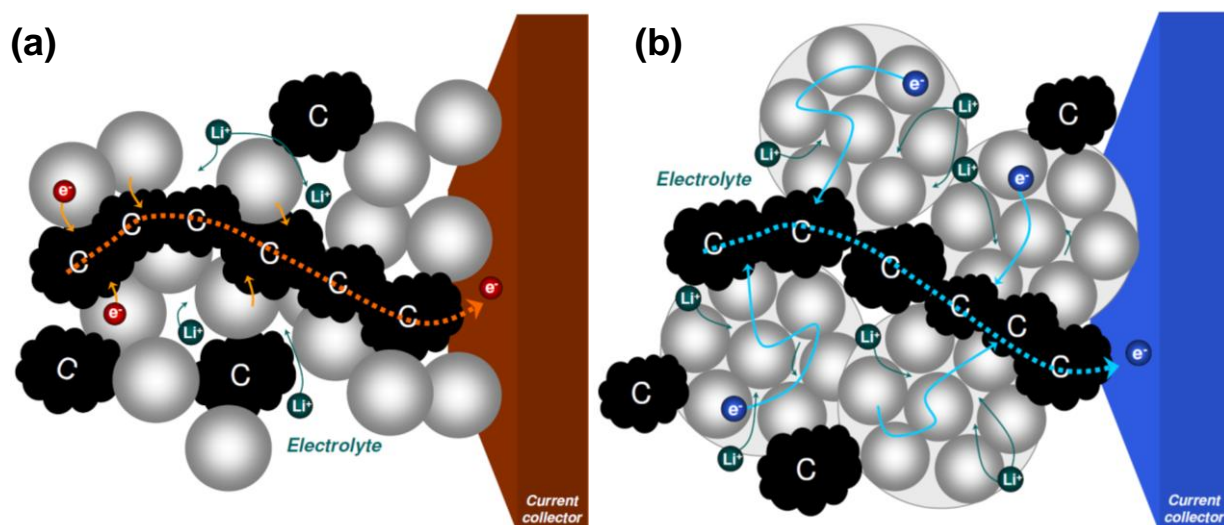


Figure 6.1: Schematic illustration of electron transport length in different morphology of TiO_2 electrode: (a) in the non-porous (used for Chapter 4) and (b) in the meso-porous (used for Chapter 5) electrode system, respectively.

References

- [1] A. Van der Ven, Elucidating the kinetics of complex Li insertion reactions in Li batteries, abstract #EMA-S4-010-2012, Meeting: Electronic Materials and Applications, Orlando, January 2012.

Abbreviations and Symbols

List of Abbreviations

HEV	hybrid electric vehicles
EV	electric vehicles
NEDO	new energy and industrial technology development organization
XRD	X-ray diffraction
JCPDS ICDD	joint committee on powder diffraction standards- international center for diffraction data
WPPD	whole powder pattern decomposition
SAED	selected area electron diffraction
BET	Brunauer – Emmett – Teller
(FE)SEM	(field-emission) scanning electron microscope
HRTEM	high resolution transmission electron microscopy
TGA	thermogravimetric analysis
BJH	Barrett – Joyner – Halenda
DC	direct current
CIP	cold isostatic pressing
PVDF	poly (vinyl difluoride)
NMP	N-methyl-2-pyrrolidone
EC	ethylene carbonate
DMC	dimethyl carbonate

EIS	electrochemical impedance spectroscopy
SSCV	slow-scan cyclic voltammetry
$np\text{-TiO}_2$	nanoporous titanium dioxide
TGP	titanium glycolate precursor
FWHM	full width at half maximum
NMR	nuclear magnetic resonance
SEI	solid electrolyte interface
$comm\text{-TiO}_2$	commercial titanium dioxide
$mp\text{-Ti}_{1-y}\text{Nb}_y\text{O}_2$	mesoporous niobium-doped titanium dioxide
$\text{Li}_x\text{Ti}_{1-y}\text{Nb}_y\text{O}_2$	lithiated niobium-doped titanium dioxide

List of Symbols

L	diffusion length
D	diffusion coefficient
$\tilde{\mu}$	electrochemical potential
μ	chemical potential
σ^δ	ambipolar conductivity
σ_{Li^+}	lithium ion conductivity
σ_e	electron conductivity
c_{Li}	lithium concentration
C^δ	chemical capacitance
D^δ	chemical diffusion coefficient
P_0	relative pressure
W_m	weight of adsorbate
C'	BET constant related to energy of adsorption in the first adsorbed layers
W	weight of gas adsorbed

d	particle size
ρ	density
P_{O_2}	oxygen partial pressure
a_{Li}	lithium activity
T	absolute temperature
C^*	chemical diffusion coefficient constant related to bulk concentration of species
n	concentration of electron
p	concentration of hole
e'	electronic defect
V_o^{**}	double positive oxygen vacancy
V_o^\bullet	single positive oxygen vacancy
V_o^x	neutral oxygen vacancy
OH_o^\bullet	proton defect
δ	oxygen nonstoichiometry
\tilde{D}_o	oxygen chemical diffusivity
E_a	activation energy
S_w	Warburg factor
Z'	impedance: real part
Z''	impedance: imaginary part
ω	angular frequency
R	molar gas constant
n^*	number of electrons transferred
F	Faraday constant
i_p	peak current
v	scan rate
Li_i^\bullet	lithium interstitial
Li_i^x	neutral lithium defect
E_{bind}	associate formation enthalpy

u	mobility
j	charge carrier
V_i	interstitial vacancy
K	mass action constant
x	lithium content
χ	trapping factor
D_M^\bullet	donor
A'_M	acceptor
Nb_{Ti}^\bullet	pentavalent niobium defect sitting on tetravalent titanium site
Nb_i^x	neutral niobium defect
V_{Ti}''''	titanium vacancy
C	total niobium concentration
R_{ct}	charge transfer resistance
Δi_p	current peak separation
$eff. D_{Li}^\delta$	effective chemical diffusion coefficient of lithium
M'_j, N'_j, γ'	exponents

Curriculum Vitae

Name: Ji-Yong Shin
Date of Birth: 31.01.1981
Place of Birth: Seoul / Republic of Korea (South Korea)

Education

Oct 2008 – Mar 2012 Ph.D. in Chemistry at Max Planck Institute for Solid State Research and University of Stuttgart, Stuttgart, Germany
(Thesis Advisor: Prof. Dr. Joachim Maier)

Mar 2006 – Feb 2008 M.Sc. in Materials Science and Engineering at Gwangju Institute of Science and Technology, Gwangju, Republic of Korea (South Korea)
(Thesis Advisor: Prof. Dr. Kurt E. Geckeler)

Mar 1999 – Feb 2006 B.Sc. in Chemical Engineering at Inha University, Incheon, Republic of Korea (South Korea)

Work Experience

Jan 2008 – Aug 2008 Research Scientist in Hybrid Materials Research Center at Korea Institute of Science and Technology, Seoul, Republic of Korea (South Korea)

Jan 2002 – Mar 2004 Military Service, South Korean Army

Publications

Journal Articles

1. J.-Y. Shin, D. Samuelis, and J. Maier, "Defect chemistry of lithium storage in TiO_2 as a function of oxygen stoichiometry", *Solid State Ionics*, article in press, DOI: 10.1016/j.ssi.2011.12.003.
2. J.-Y. Shin, J.H. Joo, D. Samuelis, and J. Maier, "Oxygen nonstoichiometric TiO_{2-x} nanoparticles *via* hydrogen reduction for high rate capability lithium batteries", *Chemistry of Materials*, **2012**, *24*, 543.
3. J.-Y. Shin, D. Samuelis, and J. Maier, "Sustained high lithium-storage performance of hierarchical, nanoporous anatase TiO_2 at high rates: emphasis on interfacial storage phenomena", *Advanced Functional Materials* **2011**, *21*, 3464.
4. R. Singh, T. Premkumar, J.-Y. Shin, and K.E. Geckeler, "Carbon nanotube and gold-based materials: a symbiosis", *Chemistry—A European Journal* **2010**, *16*, 1728 (Review article).
5. G. Jo, W.-K. Hong, J.I. Sohn, M. Jo, J.-Y. Shin, M.E. Welland, H. Hwang, K.E. Geckeler, and T. Lee, "Hybrid complementary logic circuits of one-dimensional nanomaterials with adjustment of operation voltage", *Advanced Materials* **2009**, *21*, 2156 (Front cover picture article).
6. J.-Y. Shin, C. Kim, and K.E. Geckeler, "Single-walled carbon nanotube-polystyrene nanocomposites: dispersing nanotubes in organic media", *Polymer International* **2009**, *58*, 579.
7. J.-Y. Shin, T. Premkumar, and K.E. Geckeler, "Dispersion of single-walled carbon nanotubes by using surfactant: are the type and concentration important?", *Chemistry—A European Journal* **2008**, *14*, 6044.

Patents

1. J.-Y. Shin, J.H. Joo, D. Samuelis, and J. Maier, "Surface reduced transition metal oxides with increased electronic conductivity as anode materials for lithium batteries" (European patent applied 2010, and PCT applied 2011)
2. J.-Y. Shin, C. Kim, and K.E. Geckeler, "Preparation of polystyrene-coated carbon nanotubes dispersable in organic media" (Korean patent applied 2007)